U.PORTO
FEUP FACULDADE DE ENGENHARIA
UNIVERSIDADE DO PORTO

Linerless COPVs for space applications

André Filipe Moreira dos Santos

Supervisors:
António Torres Marques, Emeritus Professor
Pedro Teixeira, Ph.D.
Henrique Santos, M.Sc.

Submitted in Fulfilment of the requirements for the degree of Master of Science in Mechanical Engineering to the Faculty of Engineering of the University of Porto

Porto, September 2022

Abstract

Sending payload to space is an expensive process. However, space launch costs are decreasing because powerful and lighter rockets have entered the market. The creation of reusable launch vehicles is also associated with this cost reduction. It is also important to significantly reduce the structural weight of vehicles, which depends on the creation of new materials, technologies, and manufacturing processes. To satisfy these requirements, a strong and lightweight fuel tank design is important given the tank's proportional weight contribution to the overall vehicle weight.

Compared with space-used metal tanks, linerless COPVs can achieve a weight reduction of 40 %. This technology has long been the ambition of composite pressure vessel manufacturers. Firstly, due to the absence of metal or polymeric liners, it is possible to get a much lighter tank. Secondly, the structural performance is governed by the behavior of the reinforcement fiber producing a structure with good fatigue performance by default. Thirdly, since the liner is an expensive part of a common COPV overall cost, a linerless composite pressure vessel will typically be less expensive. Fourthly, because of an easier setup for mandrel production, it is possible to reduce substantially the lead time of these products and to make customized tanks. This technology, however, presents significant design and production challenges, such as gas or liquid permeation and the necessity to have a removable mandrel in the absence of a liner.

The work developed for this thesis establishes the first steps to developing a linerless composite overwrapped pressure vessel. Possible solutions were analyzed for the production process and the most promising one was chosen to construct the prototype.

Improving the permeation barrier characteristics of a linerless COPV, although not fundamental in an early development stage, is also a critical aspect of these products. With that in mind, possible solutions are presented to incorporate barrier materials during the production process. According to the literature, it was found that toughening the resin matrix with graphene-based nanoparticles was the most promising solution.

From the presented production methodologies, a soluble ceramic material was used to produce the mandrel that was overwrapped with reinforcement fibers. The design methodology for mandrel geometry, polar boss fitting, and winding setup is presented and discussed, along with the manufacturing approach, which is validated through the production of a prototype.

Keywords: Linerless Composite Overwrapped Pressure Vessels, Water-Soluble Mandrels, Permeation Barrier

Resumo

O envio de carga para o espaço é um processo dispendioso. Contudo, os custos dos lançamentos espaciais estão a diminuir porque entraram no mercado lançadores mais potentes e leves. Esta redução de custos está também associada ao desenvolvimento dos veículos de lançamento reutilizáveis. É importante reduzir significativamente o peso da estrutura destes lançadores com a criação de novos materiais, tecnologias e processos de fabrico. De forma a satisfazer esses requisitos, é importante ter um reservatório de combustível leve e resistente, dado à contribuição de peso que normalmente estas estruturas têm no peso total destes veículos.

Comparando com reservatórios metálicos usados em aplicações espaciais, a tecnologia de reservatórios tipo V consegue alcançar uma redução de peso até 40 %. Esta tecnologia tem sido, desde há muito tempo, uma ambição dos fabricantes de reservatórios de pressão em materiais compósitos. Em primeiro lugar, porque sem um *liner* metálico ou polimérico, é possível a obtenção de um tanque muito mais leve. Em segundo lugar, porque o desempenho estrutural é dominado pelo comportamento da fibra produzindo-se assim uma estrutura que é com defeito, resistente à fadiga. Em terceiro lugar, sendo que o *liner* é uma parte cara no custo de um reservatório comum, um reservatório tipo V será tipicamente mais barato. Em quarto lugar, devido ao *setup* de fabrico do mandril ser simples, é possível diminuir drasticamente o tempo de processamento destes produtos e produzir reservatórios personalizados. Contudo, esta tecnologia apresenta desafios no *design* e produção, tal como a permeabilidade em gases ou líquidos, e a necessidade de produzir um mandril removível, na ausência de um *liner*, para enrolamento das fibras impregnadas.

O trabalho desenvolvido nesta tese estabeleceu as primeiras etapas de desenvolvimento de um reservatório *linerless*. Foram analisadas possíveis soluções de fabrico e a mais promissora foi escolhida para a produção do primeiro protótipo.

O melhoramento das características de impermeabilização de um reservatório de pressão *linerless,* embora não seja fundamental numa fase inicial de desenvolvimento, é também um aspeto crítico nestes produtos. Por essa razão, são apresentadas várias soluções para a incorporação de materiais com propriedades impermeabilizantes durante o processo de fabrico. De acordo com a literatura revista, constatou-se quee a aditivação da resina do compósito com nano partículas de grafeno era a solução mais promissora.

Das soluções de fabrico apresentadas, foi usado um material cerâmico solúvel água para produzir o mandril que seria enrolado por fibras impregnadas. A metodologia de *design* da geometria do mandril, do *polar boss* e os setups de produção são apresentados e discutidos, também como o procedimento de fabrico, que foi validado através da construção de um protótipo.

Palavras-Chave: Reservatórios de Pressão em Compósitos Sem *Liner*, Mandris Solúveis em Água, Barreira de Permeabilização

Acknowledgments

I would like to express, firstly, my gratitude to Professor António Torres Marques for his help throughout the course of this thesis. For all his dedicated time and support, and for transmitting to me his vast knowledge.

I would like to thank FHP - Frezite High Performance for the opportunity to work on this challenging project. To Henrique Santos for his ambition and motivation and for trusting me during this work. I would like to thank José Cerqueira for his assistance during the development of this project. To Pedro Teixeira and all the FHP workers for letting me feel so comfortable inside the company. To Carolina, Raquel, and Ricardo who accompanied me during this project.

To Exequiel Rodriguez, from the Universidade Nacional de Mar del Plata, for passing me his experience in these linerless tanks technologies.

Finally, I want to thank my brother Miguel for spending hours providing me with technical advice and knowledge. To my father, who was always willing to assist me. To them both, for letting me use the resources available in our family company, DISATEC Metalomecânica, to develop most of the experimental work.

Contents

List of Symbols and Abbreviations

Abbreviations:

CFRP	Carbon Fiber Reinforcement Polymer
CNC	Computer Numeric Control
CNG	Compressed Natural Gas
COPV	Composite Overwrapped Pressure Vessel
CTE	Coefficient of Thermal Expansion
EVOH	Ethylene-Vinyl Alcohol Copolymer
FEA	Finite Element Analysis
HDPE	High-Density Polyethylene
LDPE	Low-Density Polyethylene
MEOP	Maximum Expected Operation Pressure
NASA	National Aeronautics and Space Administration
PA	Polyamide
PET	Polyethylene Terephthalate
POM	Polyoxymethylene
RTM	Resin Transfer Molding
SMP	Shape Memory Polymer
UAV	Unmanned Aerial Vehicle
VARTM	Vacuum Assisted Resin Transfer Moulding

Symbols:

α	Winding angle, °
σ_{hel}	Helical fibers allowable stress, MPa
σ_{hoop}	Hoop fibers allowable stress, MPa
σ_{TS}	Tensile strength, MPa
E	Elastic modulus, MPa
M	Maximum external cylinder bending moment, Nm
m_r^0	Maximum normalized radial bending moment
N	Pressure vessel efficiency, m
$N_\emptyset$	Resultant load in the axial direction, N
N_θ	Resultant load in the radial direction, N
N_{f_i}	Load carried by the fibers winded at an angle α_i, N
N_f	Load carried by the fibers, N
n_i	Number of plies at winding angle i
p	Burst pressure, MPa
P	Internal pressure, MPa
p_f	Reactive contact pressure, MPa
P_{ULT}	Ultimate pressure vessel's pressure, MPa
PN	Pattern number
ν	Poisson's ratio

r	Distance from the mandrel axis to its surface, mm
R	Pressure vessel internal radius, mm
R_C	Cylinder internal radius adjusted with hoop strain, mm
R_F	Port opening radius, mm
R_{NX}	Radius to the center of load, mm
R_O	Exterior radius of the polar boss fitting, mm
SI	Skip index
SR	Pressure vessel stress distribution factor
T	Axial load applied in the pressure vessel, N
t_{hel}	Helical fibers thickness, mm
t_{hel_p}	Helical fibers thickness in a single ply, mm
t_{hoop}	Hoop fibers thickness, mm
t_{hoop_p}	Hoop fibers thickness in a single ply, mm
T_F	Polar boss thickness, mm
T_g	Glass transition temperature, °C
V	Internal volume, m^3
W	Pressure vessel mass, kg
y	Dome profile function
z	Coordinate in the pressure vessel's axial direction, mm

List of Figures

List of Tables

Chapter 1

Introduction

Composite Overwrapped Pressure Vessels (COPVs) are defined as structures that comprise layers of wound fibers, specially designed to withstand pressurized fluids. COPVs are frequently used in the engines of both commercial and military aircraft as well as spacecraft. They are frequently used to convey liquid fuel or compressed natural gas for buses, as well as for aviation and other forms of transportation [1].

Sending payloads into space is an expensive process. Launching a single kilogram into lower earth orbit can cost companies over 1500 € using the Falcon Heavy launcher. To send a kilogram of payload to the geosynchronous orbit the price is around 30000 € [2]. With the same amount of cargo on the moon, the price tag rockets to over a million euros [3]. If the destination is the surface of Mars the price jumps to 2,7 million euros per kilogram [4].

This price has dramatically decreased over the past fifty years because smaller, more powerful, cheaper, and lighter rockets have entered the market [5]. Figure 1 presents a picture of the different low earth orbit launching prices per kilogram over the last years.

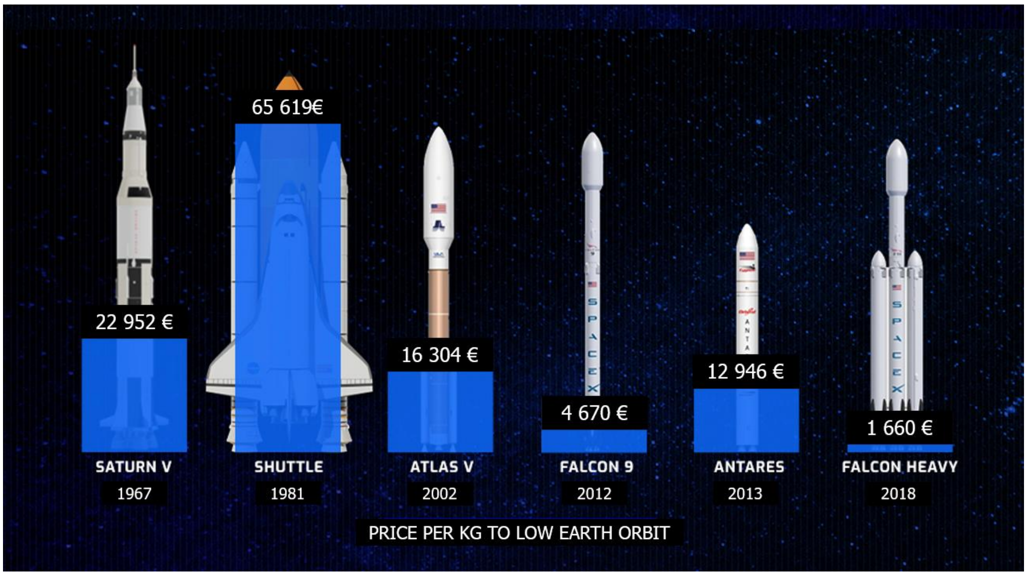

Figure 1- Low earth orbit payload price per kg through the last years, adapted from [6].

The creation of reusable launch vehicles is essential for reducing costs, and more frequent launches are associated with reduced overall transport costs per launch. It is also necessary to significantly reduce the structural weight of vehicles, which will depend on the creation of new materials, technologies, and manufacturing processes. To satisfy these requirements, a strong and lightweight fuel tank design will be essential given the tank's proportional weight contribution to the overall vehicle weight [7].

1.1 Motivation

As aforementioned, using a lighter fuel storage system reduces the overall weight of the aerospace craft or vehicle, resulting in a lower launch cost or improved payload capacity, and a greater fuel range in the case of vehicles. Linerless (also known as type V) composite pressure vessels have long been the goal of manufacturing high-pressure storage tanks. Pressure vessels of types III and IV have a liner made of metals or polymers between the liquid or gas that is stored inside and the composite outside. In the case of fuel storage tanks for spacecraft, eliminating the liner component greatly reduces the weight of the tank [8].

The linerless construction has a lot of advantages. Firstly, a lighter tank is produced by removing the liner and replacing it with a material that generally has better specific strength and stiffness. Secondly, by eliminating the requirement for strain compatibility between the liner and the composite overwrap, a design that is governed by the behavior of the reinforcing fiber may be realized, producing a structure with an improved fatigue performance by default. Thirdly, since the liner normally accounts for the majority of the vessel's overall cost, the tank will typically be less expensive. Fourthly, because of an easy setup for mandrel production, it is possible to reduce substantially the lead time of these products and to make customized tanks. A linerless tank, however, poses several design and manufacturing difficulties, such as gas or liquid permeation and the requirement to establish a method of winding the pressure vessel in the absence of the liner [9].

To contribute to a lighter and more efficient payload transporting, it is then necessary to comprehend linerless COPV technology and the primary challenges to achieving a promising and secure product.

1.2 Main Goal

The main goal of this thesis was to achieve a roadmap for the production methodology of a linerless composite overwrapped pressure vessel. Since this technology is fairly recent and not so common when compared with the other types of COPVs, the FHP - Frezite High Performance company have proposed this work with the ultimate goal of having a first linerless COPV prototype.

Other critical topics were investigated because of their importance in linerless tank technologies. Matrix microcracking occurs when a COPV shell is pressurized. This technology does not employ a liner material, so the pressurized gas or liquid may leak through these micro-fissures. As a result, materials capable of acting as permeation barriers are required.

1.3 Thesis Outline

To obtain a first linerless COPV prototype, it was first necessary to understand the general COPVs types and their production process. Thus, Chapter 2 focuses on general topics about COPVs, their classification types, and usages, their production techniques, and materials. Some structural and design methodologies that have importance when developing a COPV are reviewed too.

Thereafter, Chapter 3 focuses on the linerless pressure vessel's theme. It is firstly contextualized the current development and applications of these COPVs. Then, a review of possible ways to fabricate these pressure vessels is done. It is concluded with a list of permeation barrier materials and possible ways of incorporating them into the fabrication process.

Chapter 4 is a presentation of the prototype development steps. It starts with the construction of the mandrel geometry, followed by the presentation of the materials used and a simple structural calculation. Then, it is presented the polar boss design approach, and a methodology to incorporate a permeation barrier in the linerless COPV is reported. Finally, the trade-off between the possible removable mandrel's solutions is done.

The developed machine setups for producing the mandrel and attaching it to the filament winding machine are described in Chapter 5. Next, tests made with the washable mandrel material are presented and, then, the mandrel fabrication methodology is described. An approach used to make adhesion tests between the composite and the polar boss material is demonstrated. Finally, the linerless COPV prototype production steps are described.

Chapter 6 is the results presentation of the tests described in the previous chapter. A reflection on these results and the characteristics of the produced linerless COPV prototype is done.

Lastly, major conclusions derived from the work developed in this thesis are summarized in Chapter 7. It is also contemplated suggestions for future work to continue with this linerless tank product development.

Chapter 2

COPVs - General Topics

Before delving into the development of a linerless COPV, an introduction to the topic of pressure vessels and their vast typologies must be performed. Although the materials, manufacturing processes, and design methods used are common to other products and types of COPVs, the design of vessels of type 5 presents additional challenges. In particular, the winding process occurs with a special tool because of the absence of a liner.

The present chapter addresses first a contextualization of the different types of pressure vessels, their production methods and base materials, and some structural and design requirements.

2.1 Contextualization and Classification

One of the biggest and fastest-growing markets for advanced composites, particularly filament-wound composites, is high-pressure gas storage vessels. The main end markets are for the storage of liquid propane gas, compressed and renewable natural gas, and hydrogen. They are also used in self-contained breathing apparatuses and provide oxygen and gas storage on aerospace vehicles [10].

Even through their various types and applications, COPVs are typically built with the same geometry: a cylindrical part, two domes, and one or more openings with polar boss fittings to make the interface with the outside network. Figure 2 shows a scheme of the COPV main parts.

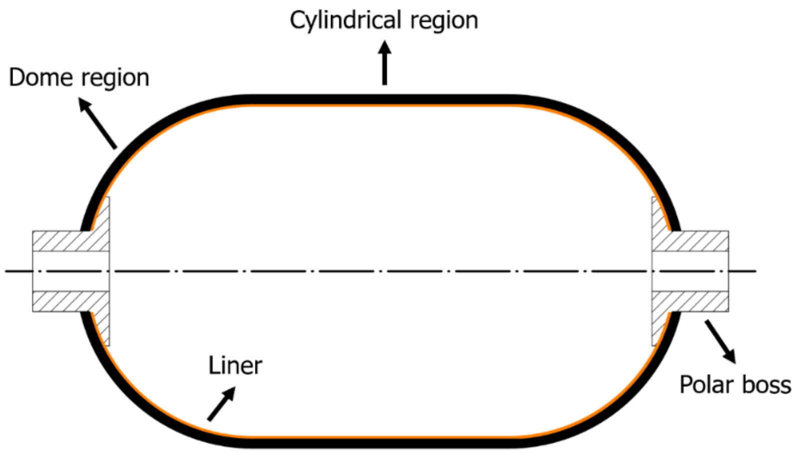

Figure 2 - COPV main parts composition.

The development of new technologies and production methods made possible the creation of lighter products with increased capacity storage over years.

A type I pressure vessel is an all-metal construction, generally in steel or aluminum alloys. A type II is a tank mostly in steel or aluminum alloys overwrapped with composite in the cylindrical region, typically glass fiber composite, the metal, and the composite materials share about the same structural loading. A type III pressure vessel is a full composite overwrapped in a metal liner, generally in aluminum alloys. A type IV tank is an all-composite construction with a polymeric liner usually made of polyamide (PA) or high-density polyethylene (HDPE). The composite materials carry all the structural loads, and it is normally used as carbon fiber or hybrid carbon/glass fiber composites. A type V pressure vessel is an all-composite pressure vessel generally made of carbon fiber [10, 11]. Figure 3 shows a scheme of the ISO and ASME classification for pressure vessels, as explained above.

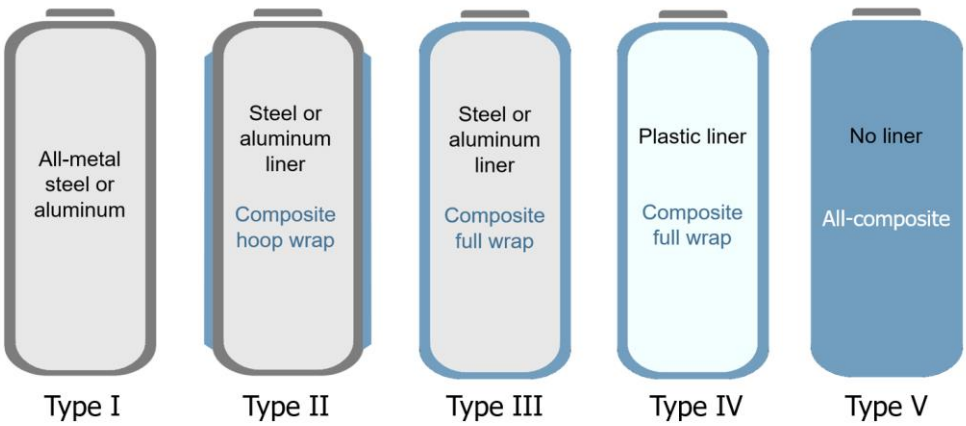

Figure 3 - ISO and ASME classification for pressure vessel types, adapted from [10].

Type I tanks are entirely made of steel, or occasionally, aluminum alloys. Because they would cause the vehicle to lose most of its payload, all-steel cylinders are too heavy to be used for onboard fuel storage in commercial vehicle applications. These vessels are typically only used for applications involving small passenger cars, to transport compressed natural gas, or for ground storage in general. They have the advantage of being typically the most affordable vessel type. Additionally, the tools and metalworking expertise required to produce them are widely accessible globally. They are best suited for industrial use in high-volume static applications and less appropriate for uses that call for portability and lightweight [11].

Type II overwrapped pressure vessels are primarily made of steel or aluminum alloys, with the cylindrical portion covered in a glass-fiber composite. This design can decrease the load on the cylindrical part of the tank, bringing the stress in that area closer to being equal to the axial stress, while also decreasing the thickness of the tank wall. They can weigh 30 % to 40 % less than type I tanks although can cost 50 % more [11].

Type III pressure vessels have advantages over the other types, withstanding higher pressures and significant weight savings (up to 30 % over type II vessels). This enables a larger storage capacity for a cylinder of the same size. These portable, lightweight gas cylinders are perfect for uses like home oxygen therapy and medical oxygen cylinders in ambulances where portability and capacity are crucial. Additionally, they are well suited for other uses like portable fluid testing, drones, unmanned aerial vehicles, fuel cell applications, aerospace, military, etc [11]. The drawbacks of this technology are liner fatigue over cycles of filling and draining, and liner corrosion [12].

The lightest cylinders currently on the common market are type IV COPVs. The main advantage of these cylinders is their reduced weight, which makes them ideal for applications requiring maximum portability. Type IV vessels have less durability and damage resistance than type III vessels, which is a drawback. Additionally, because polymers have a certain permeability to gas molecules the polymer lining is not a completely impermeable barrier, making them more prone to leakage [11]. The storage of gaseous hydrogen under high pressure in type IV vessels is now regarded as a solution to the hydrogen storage problem. To be efficient, this storage must be performed at high pressure, greater than 35 MPa, and up to 70 MPa for onboard applications [13].

Type V vessels can offer the lightest weight vessels for a given set of requirements because they don't have a metallic or polymeric liner. They present weight savings of roughly 50 % over all-metal type I, 25 % over type III, and 10% over type IV vessels, allowing for a reduction in the mass of the entire storage system [14]. Table 1 presents the demand and forecast, over the years, for CNG storage in different types of pressure vessels.

Table 1 - CNG pressure vessels demand and forecast [15].

CNG vessel type	2 007	2009	2011	2013	2015	2017	2019	2021	2023
Type I	89%	88%	84%	82%	72%	67%	65%	56%	54%
Type II	9%	11%	14%	16%	25%	26%	24%	30%	31%
Type III	2%	1%	1%	1%	2%	5%	5%	7%	8%
Type IV	1%	1%	1%	<1%	1%	2%	5%	7%	7%
Type V	-	-	-	-	<1%	<1%	<1%	<1%	<1%

To understand the differences between pressure vessel types and to recognize the potential of type V or linerless COPVs over the other technologies, it is important to understand the pressure vessel efficiency parameter, described by Eq. (1).

$$N = \frac{p \cdot V}{W} \tag{1}$$

Where p is the design burst pressure in MPa, V is the tank internal volume in m^3 and W is the tank mass in kg [16]. Figure 4 presents the different efficiencies for diverse pressure vessel technologies where it is possible to see the big advantage of the linerless COPVs.

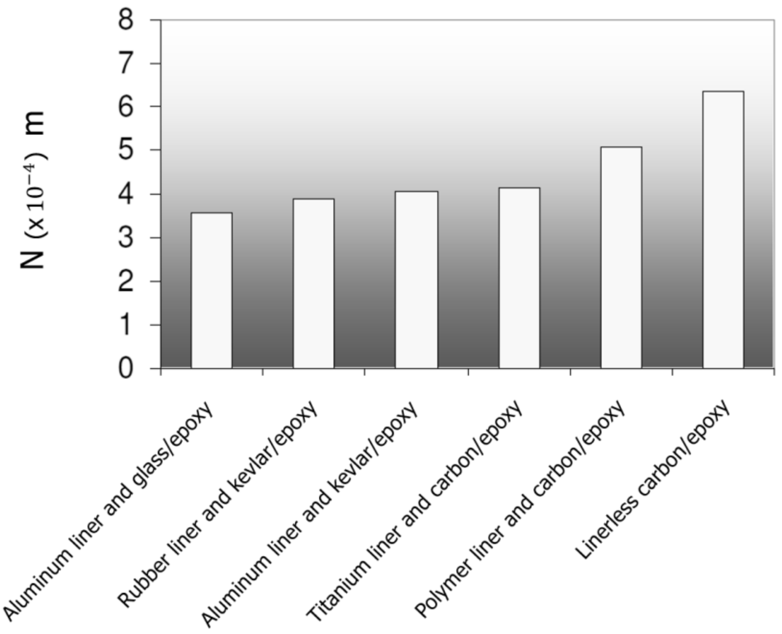

Figure 4 - Efficiencies in different types of pressure vessel configurations, adapted from [17].

2.2 Manufacturing

The overwrapping process of a linerless composite pressure vessel is the same as a typical one except for the winding mandrel that is removable or collapsible. Besides that, it could exist also a step to incorporate a permeation barrier. It is important to understand the manly used materials and the COPV production steps to achieve a potential prototype.

2.2.1 Composite Materials

Carbon fibers are known for their outstanding mechanical performance allied with low density, making them suitable for very demanding applications. The majority of the mechanical loads are carried by the reinforcement fibers in COPVs, which typically have a fiber volume of about 60 % [18, 19]. When choosing fibers, tensile modulus and strength are the most important factors. According to their tensile modulus, carbon fibers can be divided into three categories: standard, intermediate, and high modulus. Table 2 presents the typical elastic and tensile strength properties that are used in this classification.

Table 2 - Carbon fiber typical classification properties [20, 21].

	Elastic modulus GPa	**Tensile strength** MPa
Standard Modulus	230 - 250	3500 - 4900
Intermediate Modulus	250 - 340	4900 - 7000
High Modulus	> 340	< 4900

Fibers are typically chosen for COPV production based on performance requirements like burst strength, weight, or stiffness requirements. To make COPVs, both standard and intermediate modulus fibers are suitable. Higher strength fibers are needed for vessels with higher working pressures, ranging from 35 MPa to 70 MPa, demanding intermediate modulus fibers [16]. In the design of COPVs it is common to use glass fibers, not for structural purposes, but to prevent corrosion and humidity absorption. [22].

Carbon fibers are overwrapped with resin embedded, called matrix. Thermosets and thermoplastics are the two types of matrix systems most common in COPVs applications. Thermosets are produced through a chemical reaction in which resin is mixed with a hardener or catalyst and subjected to an irreversible chemical reaction, resulting in a hard, infusible matrix. Various thermosets are currently used in the composites industry, the most common are polyester, vinylester, and epoxy. Thermoplastics, like metals, soften and eventually melt when heated and then harden again when cooled. This process of crossing the softening or melting point on the temperature scale can be repeated as many times as desired without affecting the material properties in either state significantly [23].

The most used matrix in COPV production is epoxy thermosets. This resin is chosen based on manufacturing, chemical, thermal, electrical, flammability, and environmental requirements. Usually, the matrix determines also the service operating temperature of the pressure vessel [24]. The glass transition temperature (T_g), is defined as the temperature above which an amorphous or semi-amorphous polymer changes from a glass state into a semi-liquid state. As space equipment undergoes thermal cycles during its service life, T_g must be greater than the highest working temperature, or the polymer matrix will transform into a gel-like phase. Anvari argues that in thermal cycling environments, the epoxy temperature must always be less than 90 % of T_g to make sure it does not fail [25].

If the resin mixture is too viscous during the manufacturing process, there will be an abundance of resin and poor adhesion to the fibers. On the other hand, if the resin is not sufficiently viscous, the resin may drip and result in a deficit or uneven distribution of the material [16, 24]. The duration of time that a mixture will stay liquid at a specific temperature is known as pot life. This property is crucial for managing the time and temperature of vessel manufacturing [19].

2.2.2 Production Processes

Most composite pressure vessels are obtained by filament winding. The interior geometry of the vessel is usually defined by a mandrel, which revolves around itself while an automated carriage covers it with reinforcing fibers. Following the completion of the winding process, the mandrel and fibers are subjected to the curing process. [16, 19]. Figure 5 is a picture of the filament winding of a COPV.

Filament winding is classified into three types based on the resin impregnation method: dry-winding, pre-preg winding, and wet winding. Wet winding is the most commonly used method, where the fiber is automatically impregnated using resin baths during the process [16, 24].

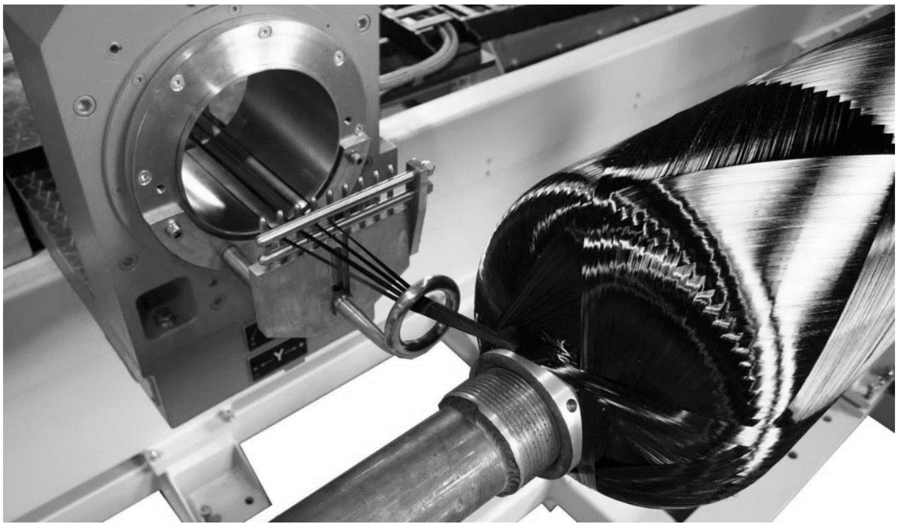

Figure 5 - COPV production by filament winding method, adapted from [26]

Pre-preg winding, alternatively, eliminates the need for resin handling during the process because the fibers are already impregnated during the production step. Because pre-pregs can be more high-controlled produced, they have the greatest control over resin content, and thus, mechanical properties. However, it is considered the most expensive method due to the higher costs of materials. The dry-winding process is still in its early stages, dry fibers are wounded and resin is added after the geometry is obtained [16, 24]. Figure 6 presents a scheme of the wet winding process.

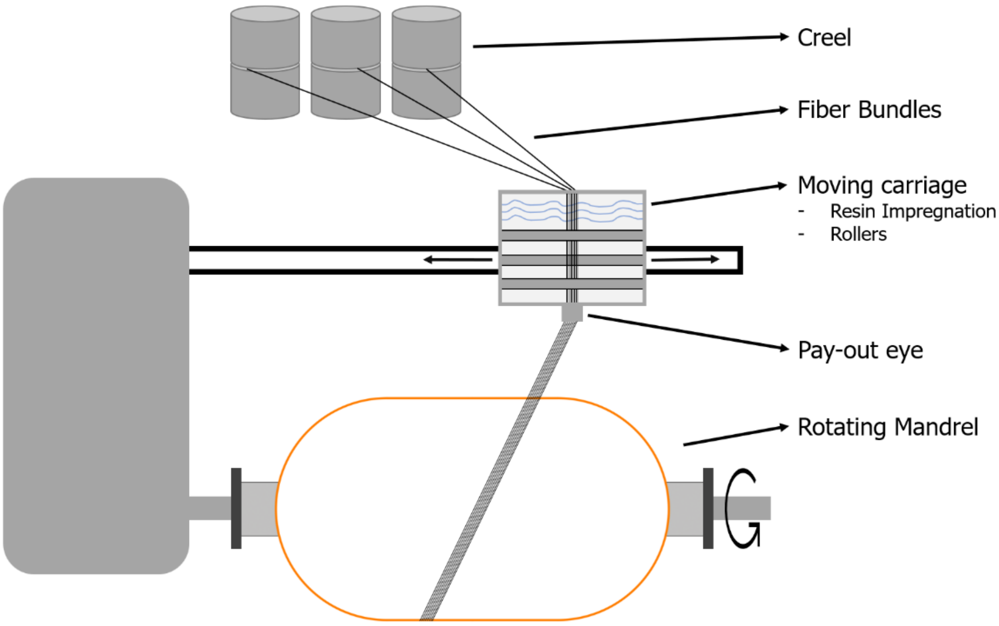

Figure 6 - Wet filament winding production process, adapted from [16, 19].

The fiber bundles are pulled from the creel and placed in a moving carriage. Then, the fibers pass through a resin bath and a sequence of rollers inside the carriage remove the excess resin to ensure a homogeneous impregnation. The impregnated fibers wrap around the mandrel as it turns, forming a composite winding over the mandrel's surface. The carriage longitudinal rate and the rotary velocity of the mandrel determine the exact direction of the composite winding [16, 19]

The axes of the machine are all in the carriage except one of them which is the rotation of the mandrel. The minimum number of axes to be possible for filament wind is two, one is the horizontal movement of the carriage and the other is the mandrel rotation. The more axes or degrees of freedom a winding machine has, the bigger the flexibility for winding different shapes and patterns [16, 19].

In the case of type II, III, and IV COPVs, the liners serve as mandrels. In the case of type V tanks, the mandrel must be removable. These mandrels are directly deposited with fibers. The bandwidth is defined as the width of the fiber bundle fed by the carriage. A larger bandwidth may reduce the number of winding cycles required to cover the mandrel. This parameter is an important factor that influences the tank weight performance and should be carefully chosen to deliver a continuous smooth covering of the mandrel. The winding angle is defined from the mandrel axis [19]. Figure 7 presents some of the parameters described above.

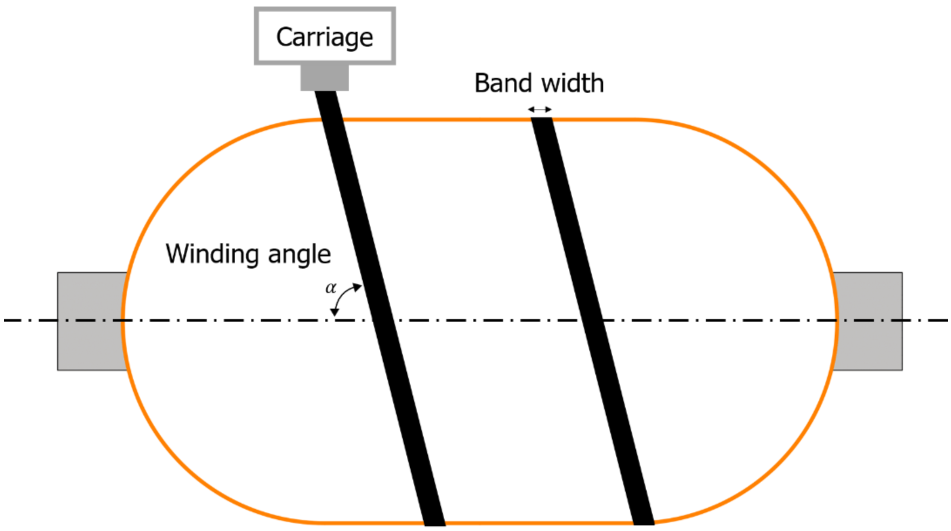

Figure 7 - Some filament winding parameters.

The shortest path between two points on a surface is defined as a geodesic curve. Geodesic winding is to apply the fibers in the described curves. It is a method commonly used because it ensures consistent winding. The lateral forces applied in the fibers are close to zero in this scenario, they are mostly loaded with normal forces against the mandrel which prevents the occurrence of fiber slippage [16, 24].

In axisymmetric geometries, like COPVs it is used Clairault’s relation that is valid for any point on a geodesic path located on an arbitrary surface of revolution.

Clarault's relation is described in Eq. (2).

$$r \cdot \sin\alpha = \text{Constant} \qquad (2)$$

Where r is the radial distance of any point on a geodesic path from the mandrel axis and α is the winding angle [16].

In more sophisticated designs, non-geodesic winding is used because it improves pathways flexibility. On the other hand, they require frictional forces to keep them from slipping off the mandrel surface since they are unstable. As a result, because the friction coefficient dictates the set of winding trajectories, it becomes a significant factor in the process [19]. It depends on the fiber/resin combination and generally, the friction limits are established empirically [16].

The type of winding is defined by the winding angle, which is measured from the mandrel axis. A ply with a determined α angle is laid when the carriage moves from one end of the vessel to the other. When the carriage reverses direction, the bundle forms a negative α angle. When producing COPVs, it is possible to define: helical, polar, and hoop winding layers [16, 19]. Figure 8 is a scheme of each winding type.

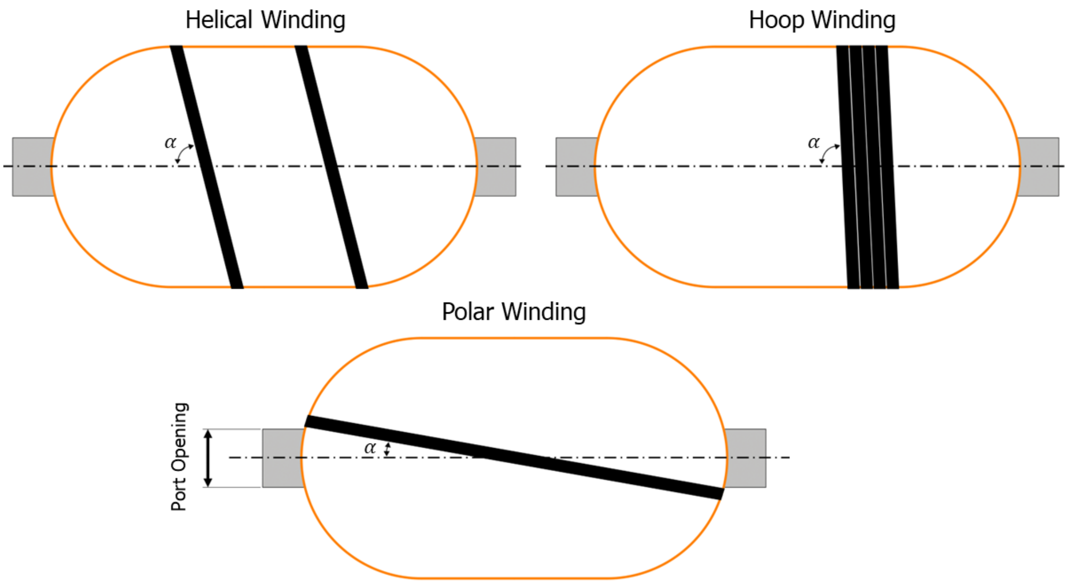

Figure 8 - Types of winding layers, adapted from [16, 19].

The polar winding layers have a small winding angle specified by port openings and part length, covering the dome parts of the vessel. Helical winding is more flexible than polar winding because it has a wider range of winding angles, although it will depend more on the friction coefficient. It is commonly used in the manufacture of composite tubes and pressure vessels. Almost every diameter and length combination can be wound by trading off the wind angle and circuits to close patterns [16, 19].

Hoop windings cover the cylindrical part of the pressure vessel, and their angles (close to 90°) are dictated by the diameter and bandwidth of the fiber bundle. It increases the structure's radial strength, whereas helical winding holds the hoop circuits, gives end stability, and helps to withstand axial loads [19].

Another important factor in the filament winding process is understanding pattern generation. PN is defined as the pattern number and represents the number of cycles that need to pass before the fiber bundle is placed next to the first one, SI is the skip index and represents the number of cycles that the pattern skips, as shown in Figure 9 [27].

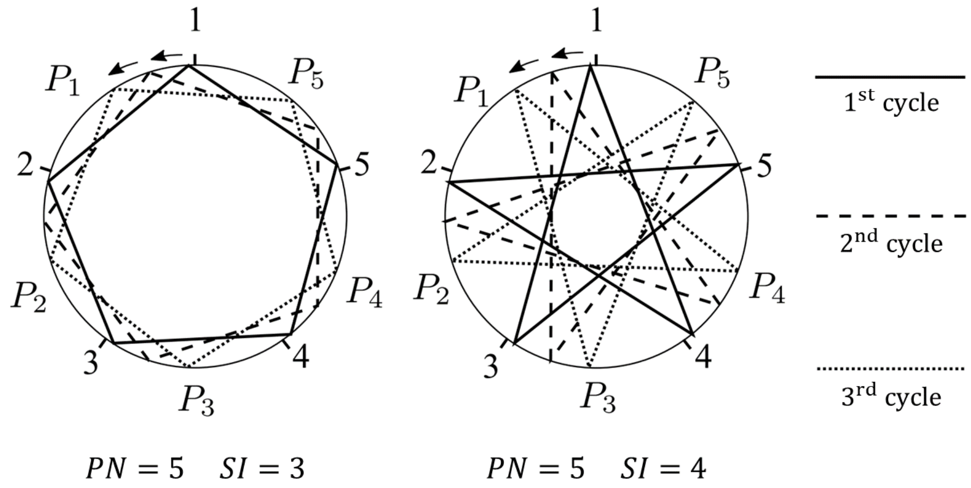

Figure 9 - Two types of pattern generation cycles, adapted from [28].

Currently, winding settings are adjusted using filament winding simulation software, which normally accepts input for raw materials, mandrel geometry, fiber bandwidth, winding angle, pattern, mandrel coverage, friction coefficient, and the majority of process parameters. Once the user enters the desired parameters, it calculates the various winding configurations approximating the part by triangles (on which the fiber path corresponds to a straight line), or the path can be calculated by solving a set of differential equations numerically [29]. As a result, designing the winding sequence is an iterative process in which the input parameters are adjusted until the winding is optimal. Some winding simulation software immediately exports FEA files with the lay-up and material configuration, allowing developers to modify the winding parameters and get the best configuration faster [18, 30].

Following the completion of the winding procedure, the COPV is sent to the curing step to consolidate the resin matrix. The pressure vessel should be rotating in a horizontal position to ensure a homogeneous distribution of resin content. The mandrel remains inside during this process [16, 19].

During the curing stage, a thermoset polymer such as epoxy can go through several phases: sol glass, liquid, gel glass, gel rubber, and char. The mechanical qualities, such as shear strength and viscosity, as well as molecular movement, distinguish the various phases [31]. The reaction with hardeners produces three-dimensional molecular chains during curing, a process known as cross-linking. Because of these cross-linkings, the molecules are rigid and cannot be remelted or molded. The more cross-linkings there are, the stiffer and thermally stable the material will be [24, 31].

Gelation is the abrupt and irreversible change of a viscous liquid into an elastic gel system. Its occurrence is determined by the functionality of the epoxy resin and the component stoichiometry, but not by experimental conditions such as curing temperature. Vitrification is the physical change of material from a liquid or rubbery state to a glassy state caused by an increase in the crosslinking density. This happens when the glass transition temperature (T_g) equals the curing temperature [31].

The heating phase of a typical cure cycle for a curing thermoset epoxy part is schematically shown in Figure 10. It has two ramps as well as two isothermal holds. The initial ramp and isothermal hold are employed to allow the resin to flow (bleed) and volatiles to escape. The imposed viscosity curve in the figure illustrates that, when heated, the semi-solid resin matrix melts and the viscosity drops dramatically. The polymerization component of the cure cycle occurs during the second ramp and hold. During this stage, the resin viscosity reduces slightly due to the addition of heat and then rises substantially when the resin's kinetics initiate the cross-linking process. During the second isothermal hold, the resin solidifies, and the cross-linking process proceeds. The resin is kept at this cure temperature for the duration of the cross-linking procedure [32].

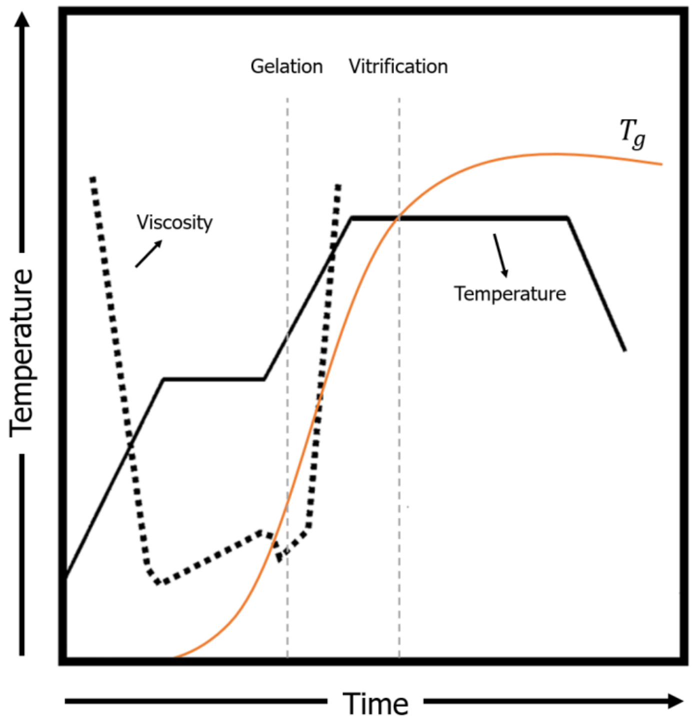

Figure 10 - Typical epoxy thermoset thermal curing cycle, adapted from [32, 33].

Another production technique to produce COPVs is the automated fiber placement system. It is made up of a placement head and a robotic arm that is computer controlled by sophisticated software packages. The lay-up head combines several manufacturing phases, including lay-up, curing/melting, and consolidation, boosting the productivity of this method. When performing a lay-up, the placement head applies heat and pressure to the narrow pre-preg tape surfaces. This pressure is applied by a consolidation roller, which squeezes the air out of the composite structure, and a heat source (hot gas torch or laser system) melts or cures the pre-pregs, being thermoplastics or thermosets [34]. Figure 11 presents a scheme of the placement head.

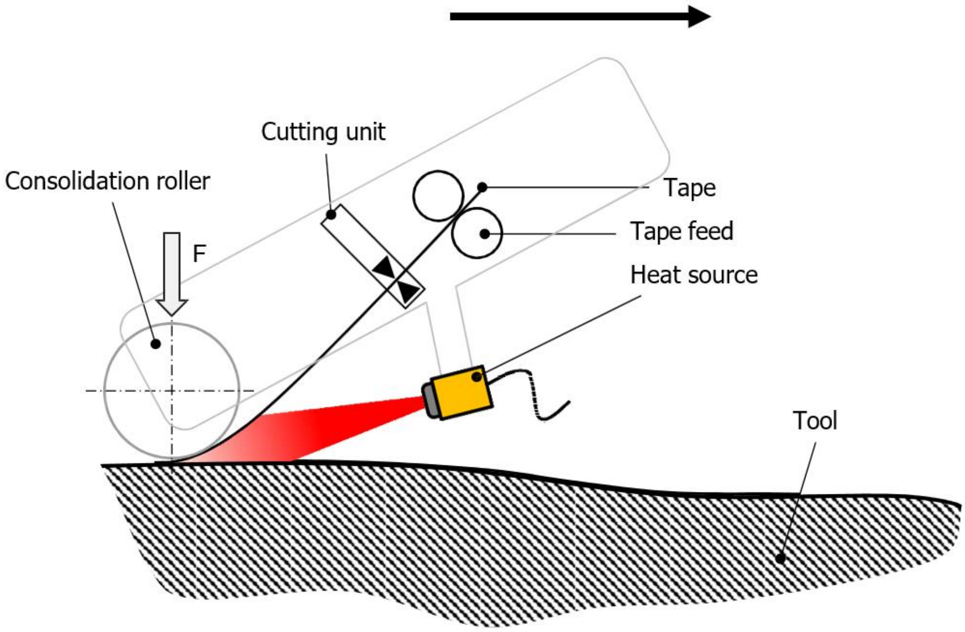

Figure 11 - Automated fiber placement lay-up head, adapted from [35].

Many major organizations employ automated fiber placement to build aerospace equipment, but this fabrication technology is not available to some small and medium-sized businesses due to the high investment required [36].

Because of its high degree of automation and efficient process with a minimal number of consumables and process steps, this is a promising technology. This technology is particularly well suited for big pressure vessels because of the unlimited part thickness and high tensile strength of the resulting laminate [37]. The National Composites Centre has manufactured a linerless tank using this technology, demonstrating the future of composite space tank technology [38]. Figure 12 shows a photo of this tank.

Figure 12 - The National Composites Centre linerless tank, near the automated fiber placement system, adapted from [38].

2.3 Design Approach

To have an insight into the thickness that the composite pressure vessels shell should have, in the hoop and helical direction, to bear the expected internal pressure, it can be used the netting analysis methodology. Another factor that is important for the pressure vessel performance is the dome part, a theoretical design approach to this part is presented after the netting analysis methodology description.

2.3.1 Netting Analysis

Netting analysis is a simple analytical technique to design and evaluate filament-wounded composite pressure vessels. It only considers the stress in the fibers ignoring the influence of the resin matrix. For that reason, it can be considered a conservative model [39]. Burst tests demonstrated that the resin matrix starts to fail at a low level of internal pressure being the fibers responsible for withstanding loading up until their fracture. The netting theory also neglects any interaction between the filaments [23]. This methodology also assumes that the fibers do not possess bending or shearing stiffness and carry only the axial tensile loads [16].

The netting theory that will be presented below is the proposed methodology by Peters and Tew [16, 40]. Considering a cylindrical section of a close-ended pressure vessel with an internal radius R, subjected to an internal pressure P with helical and hoop layers overwrapped. The winding angle is represented by α, σ_{hel} is the helical fibers allowable stress, σ_{hoop} is the hoop fibers allowable stress, t_{hel} is the helical fibers thickness and t_{hoop} is the hoop fibers thickness. E is the fiber elastic modulus and σ_{TS} is the fiber tensile strength. Figure 13 presents the free-body diagram for the cylindrical wall composite plies.

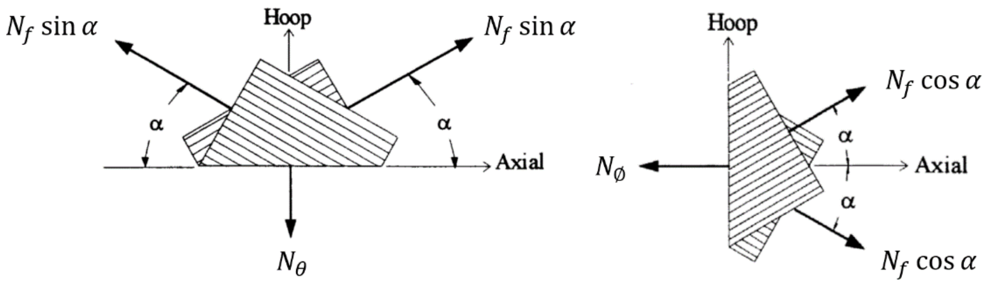

Figure 13 - Free-body diagram for the cylindrical composite plies, adapted from [41].

Considering N_f the load carried by the fibers in a single ply. Because the fibers carry all applied load the free-body diagram will only be in equilibrium if:

$$N_\theta = 2 \cdot N_f \cdot \sin^2 \propto \quad (3)$$

and

$$N_\emptyset = 2 \cdot N_f \cdot \cos^2 \propto \quad (4)$$

Each layer of a filament-wound structure consists of two plies of fiber (α and $-\alpha$). The total load carried by a set of plies is obtained by:

$$N_\theta = 2 \cdot n_1 \cdot N_{f_1} \cdot \sin^2 \propto_1 + 2 \cdot n_2 \cdot N_{f_2} \cdot \sin^2 \propto_2 + \ \dots \ + 2 \cdot n_n \cdot N_{f_n} \cdot \sin^2 \propto_n = \\ = \sum_{i=1}^{n} 2 \cdot n_i \cdot N_{f_i} \cdot \sin^2 \propto_i \quad (5)$$

$$N_\emptyset = 2 \cdot n_1 \cdot N_{f_1} \cdot \cos^2 \propto_1 + 2 \cdot n_2 \cdot N_{f_2} \cdot \cos^2 \propto_2 + \ \dots \ + 2 \cdot n_n \cdot N_{f_n} \cdot \cos^2 \propto_n = \\ = \sum_{i=1}^{p} 2 \cdot n_i \cdot N_{f_i} \cdot \cos^2 \propto_i \quad (6)$$

where $n_1,\ n_2, \dots, n_p$ are the number of plies wound at angles $\alpha_1,\ \alpha_2, \dots, \alpha_p$. When are just used two filament winding angles and from equations (5) and (6):

$$N_{f_1} = \frac{N_\theta \cdot \cos^2 \propto_2 - \ N_\emptyset \cdot \sin^2 \propto_2}{2 \cdot n_1 \cdot (\cos^2 \propto_2 \cdot \sin^2 \propto_1 - \sin^2 \propto_2 \cdot \cos^2 \propto_1)} \quad (7)$$

$$N_{f_2} = \frac{N_\theta \cdot \cos^2 \propto_2 - \ N_\emptyset \cdot \sin^2 \propto_2}{2 \cdot n_2 \cdot (\cos^2 \propto_1 \cdot \sin^2 \propto_2 - \sin^2 \propto_1 \cdot \cos^2 \propto_2)} \quad (8)$$

Considering direction 1 as the hoop angle and direction 2 as the helical angle the average stresses for the fibers wounded at these angles are:

$$\sigma_{hel} = \frac{2 \cdot N_{hel}}{t_{hel_P}} = \frac{N_\theta \cdot \cos^2 \propto_{hoop} - \ N_\emptyset \cdot \sin^2 \propto_{hoop}}{2 \cdot n_{hel} \cdot t_{hel_P} \cdot (\cos^2 \propto_{hoop} \cdot \sin^2 \propto_{hel} - \sin^2 \propto_{hoop} \cdot \cos^2 \propto_{hel})} \quad (9)$$

$$\sigma_{hoop} = \frac{2 \cdot N_{hoop}}{t_{hoop_p}} = \frac{N_\theta \cdot \cos^2 \propto_{hel} - \ N_\emptyset \cdot \sin^2 \propto_{hel}}{2 \cdot n_{hoop} \cdot t_{hoop_P} \cdot (\cos^2 \propto_{hel} \cdot \sin^2 \propto_{hoop} - \sin^2 \propto_{hel} \cdot \cos^2 \propto_{hoop})} \quad (10)$$

where t_{hel_P} and t_{hoop_P} are the helical and hoop ply thickness. The total thickness for the helical and hoop directions could be calculated as $n_{hel} \cdot t_{hel_P}$ and $n_{hoop} \cdot t_{hoop_P}$ respectively. Finally, the (9) and (10) equations can be re-wrote as:

$$t_{hel} = n_{hel} \cdot t_{hel_P} = \frac{N_\theta \cdot \cos^2 \propto_{hoop} - N_\emptyset \cdot \sin^2 \propto_{hoop}}{\sigma_{hel} \cdot (\cos^2 \propto_{hoop} \cdot \sin^2 \propto_{hel} - \sin^2 \propto_{hoop} \cdot \cos^2 \propto_{hel})} \tag{11}$$

$$t_{hoop} = n_{hoop} \cdot t_{hoop_P} = \frac{N_\theta \cdot \cos^2 \propto_{hel} - N_\emptyset \cdot \sin^2 \propto_{hel}}{\sigma_{hoop} \cdot (\cos^2 \propto_{hel} \cdot \sin^2 \propto_{hoop} - \sin^2 \propto_{hel} \cdot \cos^2 \propto_{hoop})} \tag{12}$$

It is important to note that equations (11) and (12) indicate fiber thickness and not composite thickness. To obtain composite thickness is necessary to divide the values of fiber thickness by the fiber volume fraction [16].

For a pressure vessel, the running load in the axial direction ($N_\emptyset$) can be defined as:

$$N_\emptyset = \frac{P \cdot R_C}{2} + \frac{T}{2\pi R_C} + \frac{M}{\pi {R_C}^2} \tag{13}$$

Where R_C is equal to $R \cdot \left(1 + \varepsilon_{hoop}\right)$ and is the cylinder's internal radius adjusted for hoop strain. The ε_{hoop} is calculated as $\sigma_{hoop}/E,$ T is the axial load, in propellant tanks it should be applied as motor thrust (to lift the rocket); M is the added maximum external cylinder bending moment if applied. The running load is applied in the hoop direction, N_θ, and can be defined as $P \cdot R_C$ [16].

The stress ratio is an important parameter to control pressure vessel failure modes, Madhavi et al. recommend that this value should be between 0,6 and 0,8 to prevent dome or boss blowout failure. It can be defined as:

$$SR = {}^{\sigma_{hel}}/_{\sigma_{hoop}} \tag{14}$$

2.3.2 Dome Profile Design

In an isotropic material like steel, the typical dome geometry is hemispherical or semi-elliptical. In orthotopic materials, an adequate geometry is more complicated to be generated. The analytical models presented in the literature describe that the optimal dome design for fiber-wounded pressure vessels are based on differential equations [16, 42, 43].

An optimum design guarantees a high burst pressure and a large volume with the lowest possible weight. The high-stress values that the dome part experiences make it more susceptible to failure than the cylindrical part of the pressure vessel and it is for that reason that it is so important to have some criteria in its design [44].

Some authors presented the mathematical formulation to calculate the optimum dome profile. This academic work follows the methodology proposed by Mahdy et al. [43]. Their methodology was confirmed by published models like the one proposed by

Vasiliev [42]. It is based on the mechanics of materials and geodesic analysis and it is solved using numerical techniques. The main goal is to obtain through this method a shape that can safely withstand maximum volume with minimum weight [45]

For a dome shell with a polar opening, the dome profile is divided into two segments, because there is an inflection point in the first equation that occurs when the dome radius is $\sqrt{1{,}5} \cdot R_F$ where R_F is the port opening to fit the polar boss. Vasiliev recommends that the exterior radius of the polar boss part should be greater than the radius of the inflection point [42].

The first equation is valid between R (cylindrical part radius) and R_O (exterior radius of the polar boss fitting). Being r the radius coordinate and z the dome height coordinate.

The first equation is presented below, in Eq. (15):

$$y_1(x) = \frac{dz_1}{R} = -\frac{x^3\,[1 + {x_F}^2\,(k-1)]^{\frac{k+1}{2}}}{\sqrt{[x^2 + {x_F}^2\,(k-1)]^{(k+1)} - x^6\,[1 + {x_F}^2\,(k-1)]^{(k+1)}}}\,dx \qquad (15)$$

Where $x_F = R_F/R$ and $x = r/R$.

The second equation, valid between R_O and R_F, is presented below, in Eq. (16):

$$y_2(x) = \frac{dz_2}{R} = -\frac{{x_O}^2\,[1 + {x_F}^2\,(k-1)]^{\frac{k+1}{2}}(x^2 - {x_F}^2)\,x}{A}\,dx \qquad (16)$$

$$A = \sqrt{({x_O}^2 - {x_F}^2)^2\,\left(x^2 + {x_F}^2\,(k-1)\right)^{(k+1)} - {x_O}^4[1 + {x_F}^2\,(k-1)]^{(k+1)}\,x^2\,(x^2 - {x_F}^2)^2}$$

where $x_O = R_O/R$.

These equations can be solved using, for example, the trapezoidal integration method. To increase the accuracy of this numerical integration, small steps could be used to increment the r value. It can be used MATLAB or Microsoft Excel to easily make these calculations. Figure 14 presents a scheme of the trapezoidal integration methodology.

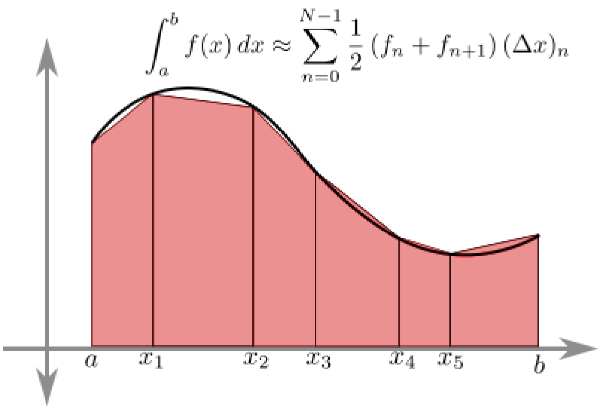

Figure 14 - Trapezoidal rule explanation, adapted from [46].

For a dome without opening the formulation to have the points that compose the profile is presented in Eq. (17):

$$y(r) = -\frac{(r/R)^{2-k}}{\sqrt{1-(r/R)^{4-2k}}}\,dx \tag{17}$$

The k parameter presented in Eq. (18) is a material parameter that relates the transversal with the longitudinal stiffness of the composite.

$$k = \frac{E_2\,(1+\upsilon_{21})}{E_1\,(1+\upsilon_{12})} \tag{18}$$

Figure 15 is a graphic where is possible to see the effect of the k parameter in the dome profile shape. When the difference between the transversal and longitudinal elastic properties decreases the dome profile starts to increase in height having a slimmer shape.

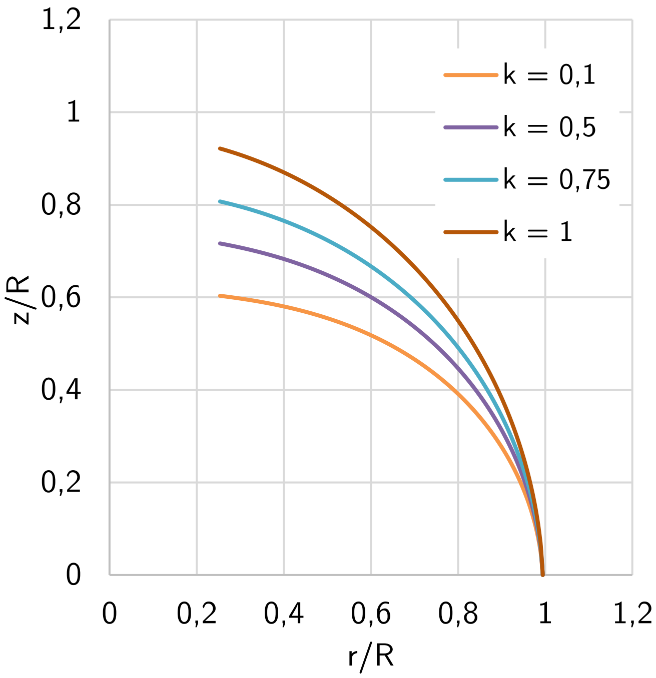

Figure 15 - Effect of k parameter in the dome profile for a R_0 equal to 0,25R.

2.3.2.1 Abaqus WCM

The Abaqus WCM is a powerful tool that helps to make Abaqus models of composite pressure vessels. It facilitates the creation of entire axisymmetric or three-dimensional finite element models of COPVs. It is a plug-in that automates the creation of tank geometries, their corresponding mesh, element-by-element material properties, and orientation assignments.

It has an option to create the dome geometry from elliptical or spherical forms, geodesic, user-defined geometries that are inputted by a list of points, or using an Abaqus part instance.

The geodesic dome geometry that this plug-in creates is a specially shaped profile that results in a nearly constant strain state along much of the fibers that are overwrapped around it. The input parameters to this geodesic shape are the cylindrical part radius and the wind angle related to the first helical layer. Figure 16 presents a print screen of the Abaqus WCM geodesic dome input parameters.

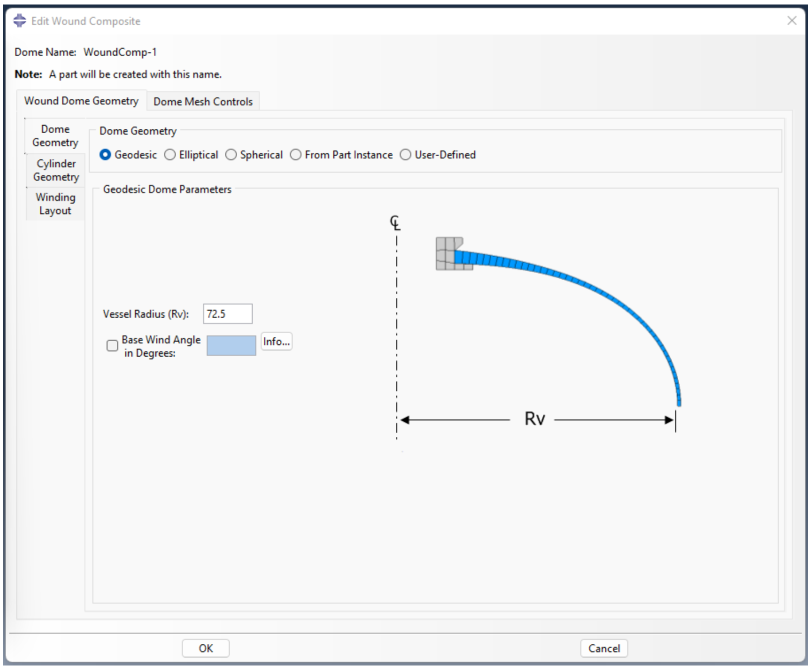

Figure 16 - Pint screen of the Abaqus WCM dome geometry input parameters.

Figure 17 shows a picture of the difference between the wind angle chosen to generate the geodesic dome profile in Abaqus WCM.

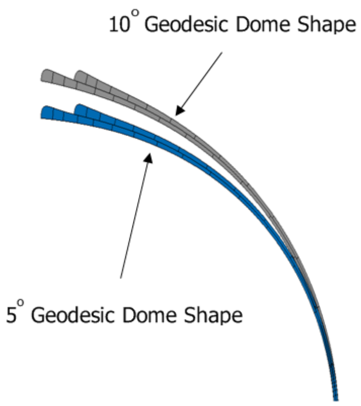

Figure 17 - Difference in the geodesic dome profile for two different winding angles.

The theoretical models presented above have been compared with the geodesic dome profile generated by Abaqus WCM. In the calculated dome, it was used a polar boss opening radius of 15 mm. In the Abaqus WCM, it was used a winding angle of 12° which is an approximation of the first polar angle used to wind a vessel with 290 mm of length and with a polar boss opening radius of 15 mm. The vessel's cylindrical part radius was 72,5 mm. Figure 18 is a graphic that contains the two dome profiles, which differ around 5 mm from each other in height.

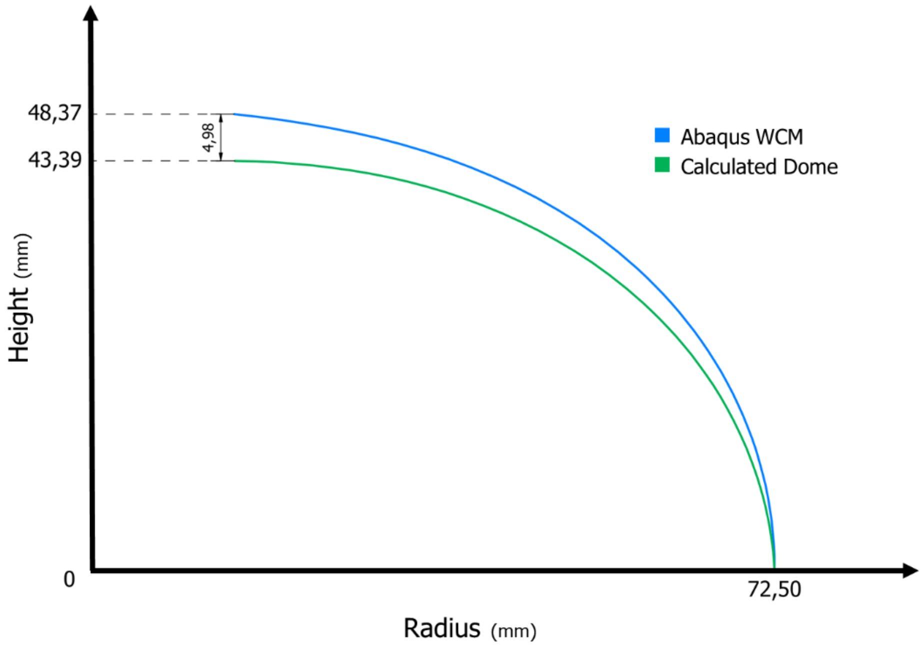

Figure 18 - Comparison between the theoretically calculated dome and the WCM plug-in dome profile.

2.3.3 Polar Boss Fitting

The polar boss fitting is a very important part that has the function of making the interface between the composite and the high-pressure gas installation. Figure 19 is a representation of a polar boss fitting in a linerless COPV construction.

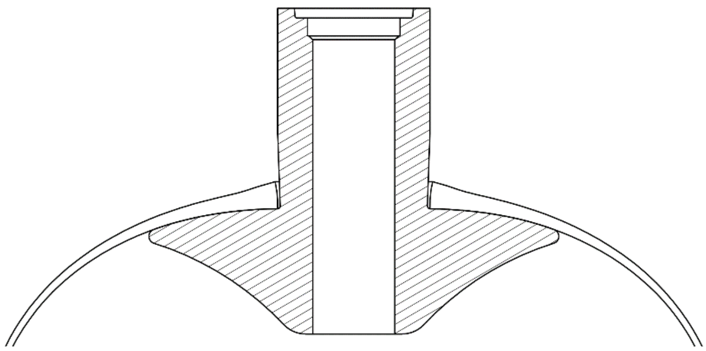

Figure 19 - Example of a polar boss in a linerless COPV construction.

The polar boss fitting is an important part that suffers some strain caused by the pressure applied inside the COPV. This part should be strong enough to bear the strain avoiding plastic deformation. However, it should suffer some strain in the outskirts to follow the strain that occurred in the CFRP, consequently avoiding gaps in the boss/CFRP interface.

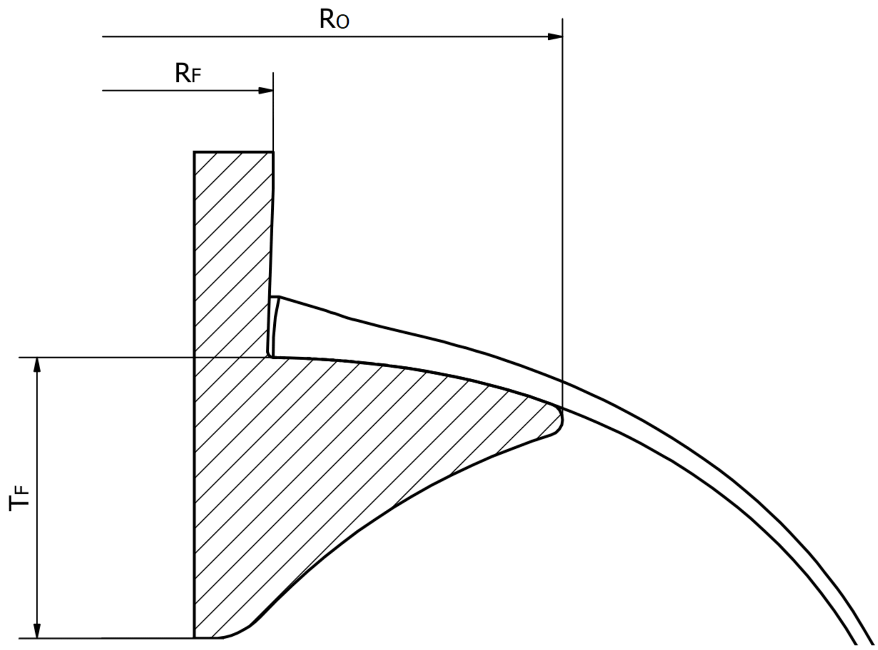

Figure 20 - Polar boss geometry main parameters.

Peters proposes a methodology for the design of the polar boss fitting based on a mathematical formulation. He recommends using finite-element analysis to confirm the final design, with a match in the composite dome deformation with the polar boss part, minimizing peaks in helical fiber stresses, etc. [16].

Considering the parameters presented in Figure 20, Peters proposes the following formulation, presented in Eq. (19):

$$\mathrm{T_F} \approx \sqrt{\frac{(R_O - R_F) \cdot {R_O}^2 \cdot P_{ULT}}{R_{NX} \cdot \sigma_{ULT}}} \tag{19}$$

Where P_{ULT} is the ultimate design pressure, σ_{ULT} is the polar boss allowable stress and R_{NX} is the radius to the center of the load, calculated by:

$$R_{NX} \approx R_F + \frac{1}{3} \cdot (R_O - R_F) \tag{20}$$

Vasiliev proposed a formulation that considers a boss with variable thickness loaded with internal pressure, p (acting inside the vessel), and reactive contact pressure, p_f. A scheme is presented in Figure 21.

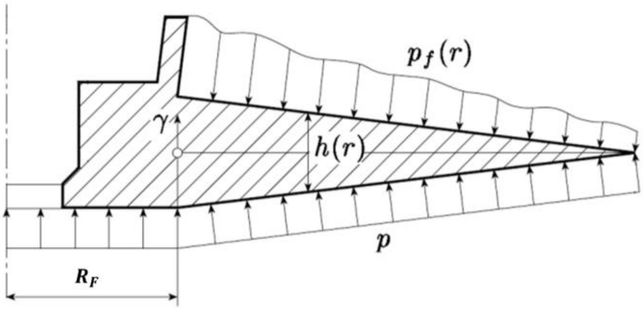

Figure 21 - Loading on the polar boss fitting, adapted from [42].

For the thickness of the polar boss, Vasiliev proposes a failure condition that is based on the bending moment that the part is subjected to [42]. The formulation is presented below:

$$T_F \geq 2{,}3 \cdot R_O \cdot \sqrt{\frac{P}{\sigma_{ULT}} \cdot m_r^0} \tag{21}$$

Vasiliev modeled the bending moment on the polar boss according to the R_0/R_F ratio, presented in Figure 22.

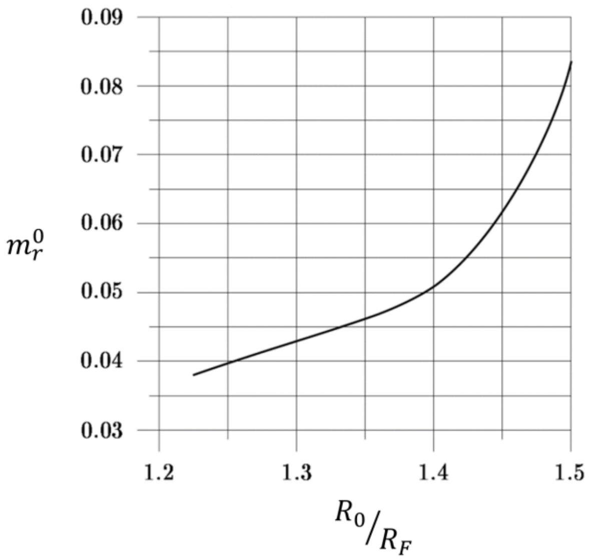

Figure 22 - Relation between the maximum normalized radial bending moment and the normalized radius of the boss polar fitting, adapted from [42].

Chapter 3

Linerless COPVs

The linerless COPV technology is relatively recent and because of that, there is not a lot of available literature on this subject. This technology is being developed by companies and institutes and just a small quantity of information is published. The main differences between the type V technologies from the others are the non-existence of liner and the challenges of having an all-composite material responsible for being a barrier to gas and liquid leakage.

This chapter first introduces the current development of type V technologies. Then, it is described the available technologies of removable mandrels that could potentially be used to fabricate linerless tanks. Finally, it is reviewed the main factors for gas and liquid leakage and possible permeation barriers to solve this problem.

3.1 Current Development

Composites Technology Development (CTD) has developed the first commercial type V pressure vessel in cooperation with the United States Air Force Research Laboratory and the University of Texas. It was installed on a student-built FASTRAC 1 satellite launched in 2010. It was a 1,9-liter tank with approximately 150 mm in diameter and 200 mm in length and weighed only 0,2 kg. It was filament wound with TORAYCA™ T700 embedded with the CTD's proprietary KIBOKO toughened epoxy resin. It had a MEOP of 1,38 MPa, a proof pressure of 6,9 MPa, and a burst pressure of around 15,5 MPa. The tank was used to store argon gas that would be micro-discharged in the satellite's plasma thruster for orbital attitude adjustments. Figure 23 presents a picture of the CTD tank in the micro-discharge plasma thruster system and two FASTRAC satellites [47].

Because the payload weight of aircraft and aerospace vehicles is sensitive, the CTD's linerless tank offers a significant performance advantage over type IV vessel versions by being 15 to 20 percent lighter. According to company studies, linerless tanks will be less expensive to produce once they are in full-scale production, most obviously because the costs of liner materials and liner fabrication will be eliminated. In addition, because liner fabrication is not necessary for linerless technology, engineers have more freedom to modify pressure vessel designs in their development [47].

The CTD company also argues that because tank design is something that is often left to last when designing an aircraft, with the type V technology is much easier to create conformable tanks that can be fitted in the available spaces [47].

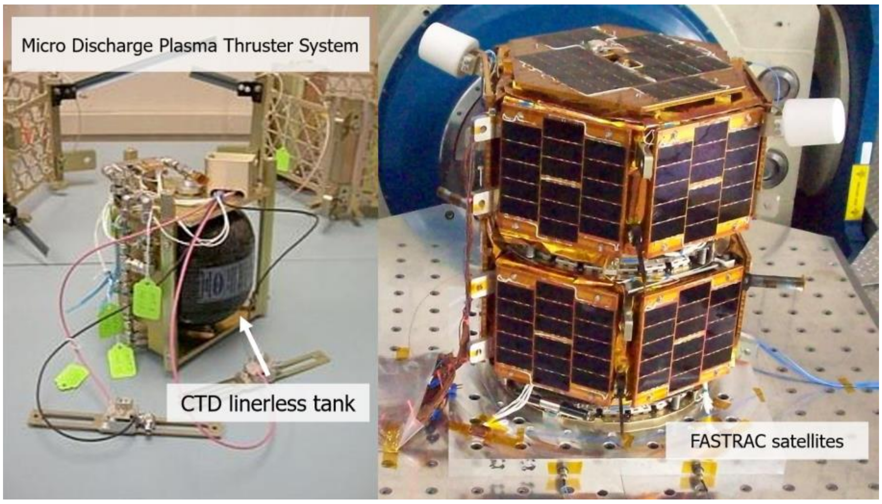

Figure 23 - Micro discharge plasma thruster system and 2 FASTRAC satellites, adapted from [48].

CTD company provides tanks to the UAV market weighing approximately 0,25 kg with a usable volume of more than two liters. They are suitable to house liquid propane to power the high-performance solid oxide fuel cells increasing UAV flight endurance. They already delivered hundreds of these tanks to use in various missions ranging from military and government applications to forest and wildfire management [49].

They have produced an 8,6-liter linerless tank weighing less than 0,9 kg to store liquid propane gas to power one UAV from Lockheed Martin called Stalker VXE UAS, used for pipeline inspection, forest and wildfire management, and other operations where it is important to capture information over a long duration. Figure 24 presents a picture of this vehicle. With the lightweight CTD linerless vessel this UAV achieved a record on the UAV Groups 2 category of flight duration, the flight was done in February 2022 and lasted more than 39 hours [50].

Figure 24 - Stalker VXE UAS unmanned aerial vehicle, adapted from [50].

According to Composite Technology Development company, innovation in this field will continue to meet high operating pressure requirements for new applications like hydrogen-powered UAVs and lightweight breathing apparatuses for use in hazardous environments [49].

For space applications, linerless COPV cryogenic storage has great potential. Cryogenic propellant tanks are an important part of any spacecraft. The tanks take up a lot of space and add a lot of weight to the spacecraft, thus they're the key weight-cutting components. The entire service performance of the spacecraft is determined by a lightweight cryogenic propellant tank. Linerless composite cryogenic propellant tanks, compared with traditional metal tanks, can achieve a weight reduction up to 40 % [51].

Space X company tested in 2016, a 12-meter diameter full composite tank that was considered to be used in their Starship interplanetary vehicle [52]. Because of the high reentry temperatures that the spaceship will experience when entering Mars's atmosphere, the team eventually decided to employ stainless steel in their tanks [53]. Figure 25 presents a picture of the linerless composite tank produced by Space X.

More recently, Boeing has fabricated a linerless cryogenic fuel tank that has passed a critical series of tests at NASA's Marshall Space Flight Center. The tank was made in the same sizer as the one used in the upper stage of NASA's space launch system rocket, which is the foundational capability in NASA's Artemis lunar. If this new tank was implemented in evolved versions of their space launch system rocket, the weight saving could increase payload mass by 30 % [54]. These two application cases were pressure vessels made from automated fiber placement and not the traditional filament winding production process.

Figure 25 - Space X all-composite cryogenic tank [52].

Infinite Composites is an American company founded in 2010 that produces linerless COPVs. They already made projects for NASA centers, Space X, the United States Air Force and Army, and a lot of other companies. Their target market consists of launch vehicles and spacecraft subsystem manufacturers who seek their products due to the importance of weight reduction in these systems. Other clients include satellite manufacturers, who can enhance their useful payload to support additional transponders, instruments, and other systems [6].

In 2020, the company has delivered 26 linerless tanks. Infinite Composites is expected to produce 780 tanks by the end of 2022. They recently supplied high-pressure pressurant tanks for a lunar lander propulsion system, hydrogen tanks for aviation applications, and a 55-unit series production of helium pressurant tanks for a small launching vehicle, which will be delivered by the end of 2023 [6].

3.2 Removable Mandrel Types

Type III and IV composite pressure vessels have a thin rigid liner that serves as the mandrel for winding the fibers. An all-composite, type V pressure vessel does not have any rigid component that can be used to wind the fibers and matrix in. That is why it needs a removable tool that can be used to wind the composite in.

Some factors that are important to account for when choosing the mandrel type are the size and complexity of the part geometry, size of openings, the resin system and curing cycle, and what type of production it will be done (high or low volume production). Other factors to take into account are the following:

- it should have enough strength to support its weight and the winding tension, besides the fiber tension pressure and curing pressure (if applicable);
- it must be dimensionally stable having a CTE appropriate to the reinforcement and curing cycle used;
- it should have the appropriate weight to avoid bending the wind axis as it can add uncertainty to the winding fiber path;
- it should be easy to remove after the curing process;
- the cost should be appropriate to the value of the part and the number of produced items.

This section reviews the different types of removable mandrels that may be used in the fabrication of pressure vessels or other composites with hollow geometries.

3.2.1 Metallic Collapsible Tooling

Metallic collapsible structures are very common when there is enough exit area for tool removal after the filament winding and curing processes. Steel is more used than aluminum to produce the tools. It has a lower CTE, a very important factor for the curing step of the composite. Aluminum tools can be used in lower temperature curing cycles and, in some cases, where a larger CTE can help in the curing process. The higher expansion can properly be used to press the composite against an external mold fabricated in a lower CTE material like steel [55].

These tools have the disadvantage of requiring long lead times to produce and being costly to fabricate and finish. Metallic tools are also typically heavier when compared with other solutions and for that reason sometimes is required to have lifting equipment to help the operators move the mandrels [55].

3.2.2 Inflatable Tooling

US Patent Number 4,684,423 describes a technique that involves a rigid tool that is covered intercalary by layers of nitrile rubber strips (disposed of longitudinally) and coatings of rubber solution. At the end of the layer's placement, there is a curing step. After the cure, the layers are cut into two parts, removed from the rigid tool, and rejoined using reinforcing straps along the seam of the joined parts. The next fabricated mandrels will not have a seam or joint, since, after constructing the second mandrel on the first inflated collapsible mandrel, the first mandrel would be deflated, collapsed, and removed from the interior of the second mandrel [56, 57].

3.2.3 Shape Memory Polymers

There are some materials with shape memory characteristics that are used as mandrels in composite materials fabrication. These materials have the capability of changing their shape in a predefined way when exposed to an appropriate stimulus. They are used in intelligent medical devices, implants for minimally invasive surgery, self-deployable systems in spacecraft, and many other applications [58].

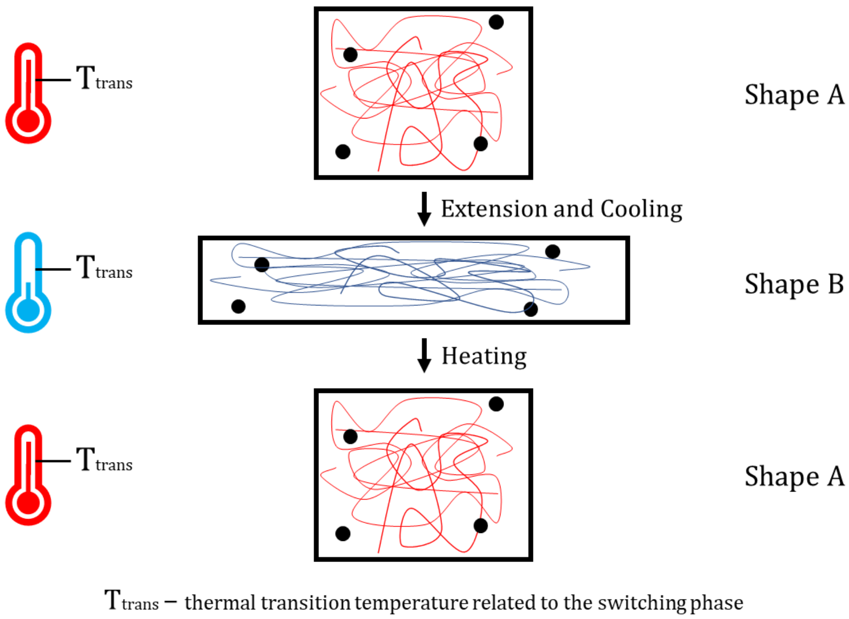

Figure 26 - Molecular mechanism of thermally induced shape-memory effect, adapted from [58].

From conventional processing such as extruding or injection molding, the polymer is formed into its initial permanent shape A. The polymer is then deformed and cooled below the T_{trans} to a temporary shape B. When heat is applied above the T_{trans}, the polymer recovers its shape. Figure 26 demonstrates the polymer deformation and shape recovery mechanism [58].

Smart Tooling is a division of Spintech Holdings company, that provides formable and reusable tooling solutions for manufacturing composite parts with complex and trapped geometries. They are indicated for a two-stage composite cure, during the initial composite cure at 121 °C the Smart Tool remains rigid and sets the inner mold line geometry of the composite part. As the temperature rises to the post-cure of the composite part at 177 °C, the Smart Tool becomes elastic and can be easily removed from the cured composite part, reformed in a mold, and reused. This technology has the capability of being reusable between 20 and 100 cycles (typically 50 to 70 cycles) [59].

Figure 27 describes the production process of a UAV inlet duct made of carbon fiber with an epoxy matrix. It was hand laid up directly in the Smart Tooling that has a release film pre-applied. After the curing step, the tool is extracted from the composite part and put into a heated reforming mold. A vacuum bag is pulled through the Smart Tool and sealed to the mold, then, vacuum is applied, and the tool and the mold cooled. In the end, the Smart Tool recovers the original geometric shape and is ready to make another inlet duct [60].

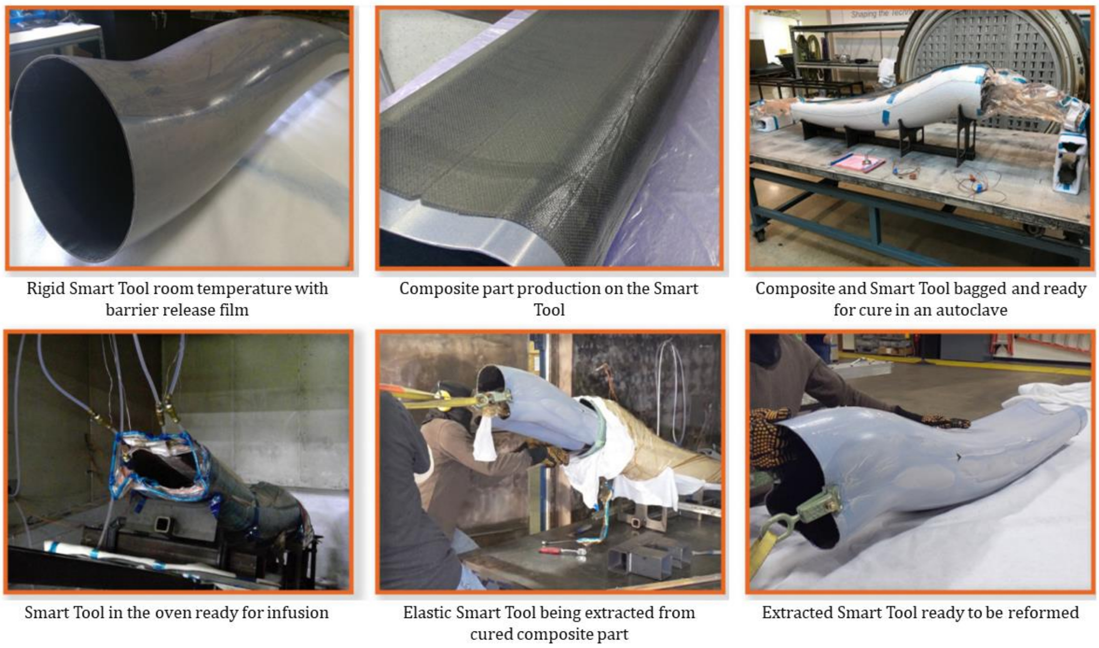

Figure 27 - UAV inlet duct production with Smart Tooling, adapted from [60].

3.2.4 Shape Memory Foam

The MUPET™ (Multiple Use Precision Extractable Tooling) is a patent-pending technology from Composite Technology Development company, which is a composite tooling system based on a SMP (Shape Memory Foam) [61].

The process uses an open-cell shape memory foam encased in a bladder. This foam is stiff enough to support loads from composite manufacturing processes like filament winding, VARTM, fiber placement, or automated fiber placement techniques. It can be machined to net-shape, high-precision forms that can impart subtle and discrete details and complex geometries. Once the lay-up is complete, the foam is pressurized to consolidate the composite during the curing process. After, the tool is removed by exercising vacuum on the still-warm SMP foam rapidly reducing its volume to allow easy tool extraction from trapped regions [47, 61].

CTD (Composites Technology Development) employed this method to make reinforced panels, tanks, tidal turbine blades, high-frequency antenna reflectors for NASA, and many other structures [61].

3.2.5 Thin Composite Layer Wounded in a Rigid Tool

This method was patented by Kaiser Compositek company to produce linerless pressure vessels. It involves a thin composite shell that is obtained by filament winding with a hard tooling. The hard tooling has the interior shape of the finished pressure vessel. The thin composite shell is cured in an autoclave and then is sectioned in half longitudinally. Then, it is done the fitting installation, the two composite halves are joined together, and a permeation coating is applied. The set is then placed in the filament winding machine and the rest of the composite is wounded to the required design thickness [9, 62].

3.2.6 Washable Mandrels

The types of mandrels presented in this section are solid blocks that can be washed with water after the composite production.

3.2.6.1 PVA (Polyvinyl Alcohol)

PVA is a biodegradable thermoplastic polymer. When exposed to water, this material dissolves, and this feature makes it a very useful material for disintegrable applications. It is used in 3D printing applications as the support structure material for complex shapes or enclosed cavities where is difficult to remove standard supports. When printing is complete, it is just necessary to dissolve in warm water to remove the PVA material [63].

It has a decomposition temperature of 180 °C however the melting point range from 180 °C to 240 °C depending on the degree of hydrolysis [64]. There was a project by the University of New South Wales, Omni Tanker, and Lockheed Martin for producing a linerless COPV, and for the concept they utilized PVA machined to the tank profile as the mandrel [65].

3.2.6.2 Sand and Sodium Silicate Mixture

Sand and sodium silicate mixtures are used to produce the foundry males. The sand is mixed with liquid sodium silicate, the mixture is placed in a mold with the interior shape of the final geometry, and then it is hardened by CO_2 gas. In the end, it is possible to have a rigid sand tool to be used as a mandrel [66].

Iqbal used this method in his Master's Thesis to produce the mandrel to fabricate a pressure vessel. The mold was made in two halves with a top opening to put the sand mixture. It was coated with talcum powder as a releasing agent, the sodium silicate was mixed with sand in a 3,5/96,5 ratio and placed into the mold. Using vibration and pressure the sand mixture filled the whole mold and then small tunnels were dug from the mold opening. CO_2 with a pressure of 0,07 MPa was released into these tunnels to diffuse it throughout the sand for the hardening process. The upper half mold was removed for inspection and some faults were found on the mandrel surface. The reason for that was the lack of CO_2 gas in those regions that were the furthest regions of gas supply. To solve this problem some gas tunnels were dug along the cylindrical part of the cylinder to apply extra CO_2. To dismantle the sand mandrel from the finished part it was placed in a container with water for eight hours, the sand lost its bonding, and the winding shaft was removed from the mandrel. Then, the set was placed in water at 45 °C for fourteen hours and after it, the cylinder was placed near a dehumidifier to dry the sand, a hair dryer and a dehumidifying bag were used to increase the water removal rate. This method was applied for two days. When the sand was completely dried, with the help of a scraper the sand was completely removed. In the end, the internal surface of the pressure vessel did not present any crack or damage [67].

3.2.6.3 Additive Manufacturing of Washable Ceramic

ExOne is a company that is specialized in binder jet 3D printing technology. They offer solutions for 3D sand printing that can be used to make foundry cores or molds and water-soluble parts. The 3D printing water-soluble production process is the same as the other sand printing systems and the raw sand particles can be the same, the difference is in the binder that in this case is water soluble [68, 69].

Figure 28 - Example of ExOne 3D printed mandrels with coating [68].

This 3D printing process can build parts up to 1800 mm x 1000 mm x 700 mm, and if bigger structures are needed, it is possible to build parts that can fit together making this technology very scalable and versatile. The binder holds its properties up to 180 °C. If silica sand is used, it is expected to have a CTE of 20 µm/mK but if it is needed for a lower CTE, the ceramic sand delivers a CTE of 3 µm/mK. After the sand tool shape is created, the part is surface coated to prevent resin migration into the porous tool during the composite fabrication. There are some coating materials to choose from, ExOne offers two coating materials, one of them hold temperature up to 180 °C and the other up to 132 °C, it can be also coated with PTFE tape. Figure 28 shows produced mandrels with a coating that holds the temperature up to 180 °C. To remove the tool, it is only necessary to wash it out with water [68, 69].

This technology is environmentally friendly and sustainable since all the washed-out sand can be recovered and reused for future print cycles [68, 69]. Some of its characteristics are presented in Table 3.

Table 3 - Some ExOne 3D printed washable part's mechanical properties [68].

	Compressive Strength MPa	**Density** g/cm^3	**CTE** µm/mK
Silica Sand	> 3,45	1,44	20
Ceramic Sand	-	1,52	3

3.2.6.4 Commercial Products

Some companies supply soluble materials to be used as removable mandrels. Advanced Ceramics Manufacturing is an American company that is specialized in developing water-soluble composite tool solutions. Most of their technologies are based on ceramic or other types of particles bonded with a water-soluble material. When water is flushed the binder dissolves and the particles fall apart from each other [70, 71].

They have a wide range of options to produce from varied methods and different washable tooling solutions. Their products allow customers to fabricate seamless, hollow, one-part composite structures using tooling material that is suitable for mass or serial production. Mandrel part applications include aerospace air/cable ducts, high-pressure tanks, hat stiffener sections, flap support fairings, manifold intakes, motorcycle wheels, automotive parts, honeycomb stabilization (make them rigid to be machined), and any hollow structural component [72]. Next, is a simple review of some of their products.

3.2.6.4.1 Aquapour™

It is a fluid slurry that is castable. It is supplied as a dry powder, water is added to activate it, and then the mixture is dumped in a mold with the desired shape of the mandrel. After some time, the material will be set up (green cured stage). The part is removed from the mold and then placed in a convection oven to be completely dried. The mandrel is ready to be sealed with PTFE tape or by a sealing product to avoid resign infiltration in the porous mandrel material [71].

After the composite production around the mandrel, it is just needed to flush water into the mandrel and it will be washed away [71]. Some Aquapour™ characteristics are presented in Table 4.

Table 4 - Some Aquapour™ mechanical properties [71].

Compressive Strength MPa	**Dry Density** g/cm^3	**CTE** µm/mK
± 1,52 at 21 **°C**	0,57	6,48

3.2.6.4.2 Aquacore™

It is a moister powder that is used to form simple shapes via compression into molds. The molds can have the final shape of the part (if possible) or can be blocks that are machined later. After the compression, the part has to be dried in an oven. Like the Aquapour™ product, the mandrel must be sealed with PTFE tape or a sealing product to avoid resin infiltration. After the composite production around the mandrel, it is just needed to flush the ceramic with water to wash it away [71]. Some Aquacore™ characteristics are presented in Table 5.

Table 5 - Some Aquacore™ mechanical properties [71].

Compressive Strength MPa	**Dry Density** g/cm^3	**CTE** µm/mK
3,45 at 21 °C	0,53	4,68

3.2.6.4.3 Clavecore™

It is a rigid tooling material made from powder that develops expanding pressure once is thermally activated. The parts are made by filling a mold cavity with this powder and heating it from 80 °C to 100 °C. At this temperature, the powder reaches the activation point and the mixture became solid. Next, the object is cooled at room temperature and unmolded [71].

After the composite production around the mandrel, the set is placed in a female cavity mold for the curing process. Upon thermal activation, the mandrel expands pushing and consolidating the individual plies against the female tool surface. After the composite curing cycle, the mandrel can be removed with flushing water [71]. Some Clavecore™ characteristics are presented in Table 6.

Table 6 - Some Clavecore™ mechanical properties [71].

Compressive Strength MPa	**Density** g/cm^3
3,39 ± 0,83	0,60 - 0,80

3.2.6.4.4 RTM Core™

RTM Core™ is a material supplied in blocks to be machined to the shape of the mandrel. Is used to meet the rigorous demands of resin transfer molding (RTM). It is a material with properties that can subject the mandrel to hot, high-pressure resin. Is high strength, impermeable, and can be removed with tap water [71]. Some RTM Core™ characteristics are presented in Table 7.

Table 7 - Some RTM Core™ mechanical properties [71].

Compressive Strength MPa		**Shore D Hardness**		**Density** g/cm^3	**CTE** µm/mK
at 25 °C	**at 176 °C**	**at 25 °C**	**at 176 °C**		
85	60	85	70	1,86	± 100 - 120

3.2.6.4.5 CF4™

CF4™ is a powder that is melted and cast in a heated mold. The key property is to form complex shapes. The casting parts are non-porous and suitable for autoclave/non-autoclave composite processing. After the composite curing step, the mandrel is removed with tap water. Some CF4™ characteristics are presented in Table 8.

Table 8 - Some CF4™ mechanical properties [71].

Compressive Strength MPa	**Density** g/cm^3	**CTE** µm/mK
> 10	~ 2,17	45 - 55

3.2.6.4.6 Aqua Tool Bond™, Aquaseal™ and Aquafill™

Aqua Tool Bond™ is a water-soluble adhesive that is used to bond the other washable products. It is ideal for gluing large and complex parts or repairing them [71].

Aquaseal™ is a painting material that is used in the Aquapour™ and Aquacore™ ceramics to inhibit the migration of resin into the porosities. It makes a smooth finish to the ceramic surfaces. It can take curing temperatures until 193 °C [71].

Aquafill™ is used to patch defects that the Aquapour™ and Aquacore™ materials could have on their surface. It is easily applied on the mandrel surface, and dries at room temperature but can take slightly longer to wash out than the other products [71].

3.3 Permeation Barrier

The other types of pressure vessels (type III and IV) incorporate a thin metallic or polymeric inner liner which serves as an inert permeation barrier. The linerless technology does not use any rigid wall to avoid the permeation of liquid or gas at high strain levels. The composite laminate is subjected to bi-directional stresses that result in transverse microcracking that promotes leak paths to the fluid's escape [9, 17]. Figure 29 is a microscale photo of microcracks present in a composite laminate.

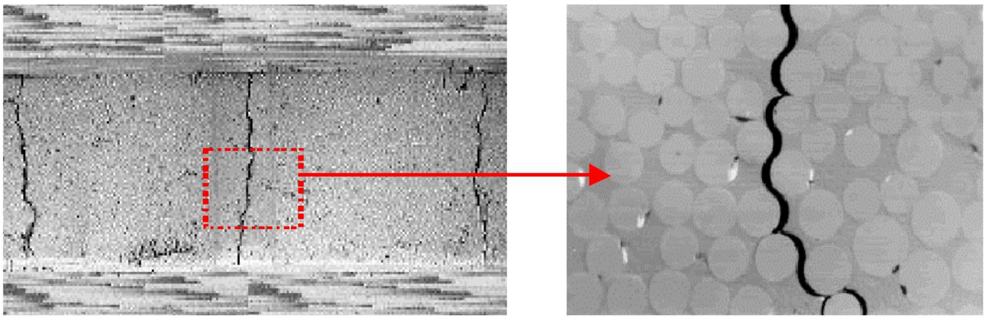

Figure 29 - Microcrack in a composite laminate, adapted from [14].

Designing a linerless COPV to be reusable over several fill-pressure-drain cycles requires that the composite materials must exhibit long-term structural integrity and minimal leakage due to mechanical fatigue load. The microcracking damage propagation and the resulting permeation of the composites under the tank's operation conditions is a very important subject when developing these tanks [73].

Besides the problem of fluid escape from the microcracking paths, is that all the polymers are gas permeable to different degrees, making the composite matrix subjected to another permeation mechanism. It is a problem that also occurs in type IV pressure vessels through the polymer liner [9].

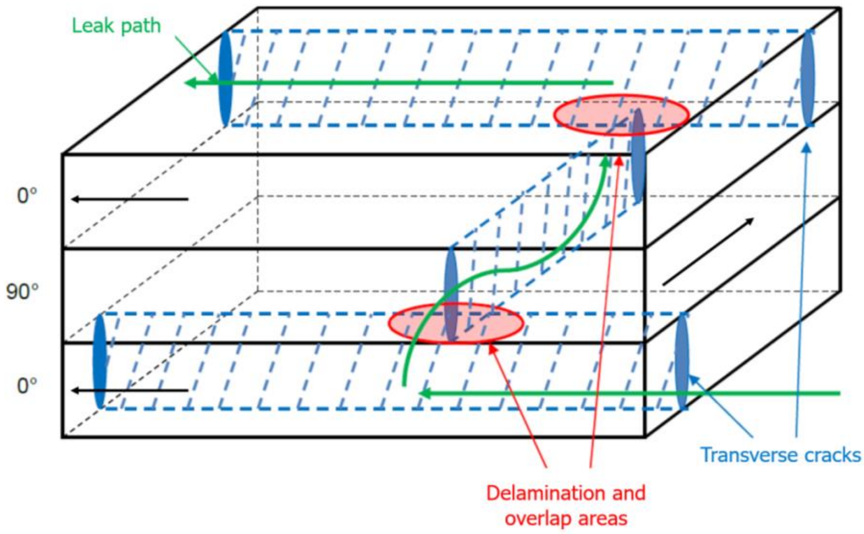

Figure 30 - Leakage pathway through the composite laminate defects, adapted from [7].

In a linerless COPV, high strains act perpendicular to the fibers and cause the composite plies to microcrack and create an interconnected pathway for leakage. The dome/cylindrical part transition region is typically where will first leak due to a combination of high local stresses and a thin-wall composite construction [74]. Figure 30 presents a scheme to explain the leakage pathway in a laminate with different types of defects.

A further concern that is necessary to prevent in some applications is the infiltration of moisture in the microcracking through the exterior of the pressure vessel. In very low-temperature environments the moisture can freeze and expand resulting in progressive damage to the composite laminate [9].

The matrix material utilized in the composite must reduce the composite microcracks under the COPV working conditions to completely prevent the possibility of leakage and permeation. It is crucial that the matrix can control permeation and it must also be sufficiently resistant to stop laminates from delaminating before the fiber performance limits are reached. A key element of optimizing the design of these lightweight pressure vessels is understanding the strains at which microcracking begins in a composite material [14].

A single-material tank that meets the required structural and barrier performance requirements is made possible by fine-tuning the design parameters, such as fiber angle, fiber volume, and laminate thickness. Although the laminate serves as both a structure and a barrier throughout the tank, engineers can change the design elements to vary the functionality. They can, for example, emphasize structural or barrier features in certain areas of the tank wall rather than changing the entire tank [47].

Composites Technology Development company has a patented producing method to place woven fibers in specific pressure vessel locations during the filament winding process that contributes substantially to the stiffness and strength of the composite wall and consequently promotes a superior barrier against leakage. When a composite pressure vessel is pressed monotonically or subjected to pressure cycles during service, woven fiber plies protect against the growth of manufacturing flaws, voids, and resin microcracks. According to the patent, at least one ply that composes the pressure vessel wall is designed to provide a leakage barrier while also providing a fraction of the overall needed stiffness and strength of the pressure vessel structure. The first mode of failure for this ply should be a rupture in the fiber reinforcement, confined to the barrier plies, resulting in leakage of the pressurized contents. This fiber-dominated failure mechanism is designed to be extremely repeatable and predictable, allowing the design of all-composite pressure vessels with highly repeatable and predictable leaking failure responses. To ensure that fiber rupture is the first mode of failure, the barrier ply (or plies) must contain a highly ductile resin material that resists the initiation and propagation of microcracks up to strains that exceed the rupture strain capacity of the fiber reinforcement [74].

3.3.1 Polymeric films

To prevent gas or liquid leakage through lamina defects, a thin layer of materials that can act as an internal barrier, such as certain polymeric films, can be applied.

A very important subject when using polymer films as a permeation barrier is the application process of these films in COPV fabrication. COVESS is a company that develops thermoplastic composite pressure vessels and they have a patented process for applying polymeric film in the production process of COPVs. It is based on the filament winding process but uses a polymer film strip. The filament winding machine can wind the strip around the mandrel in such a way that it is possible to guarantee that the mandrel is entirely covered with this polymeric film. The inventor argues that 50 % of the strip width is an optimal overlapping distance in terms of barrier effect versus the amount of strip material to achieve that effect. The optimal strip width can be determined by experiments, but the inventor reports that the strip should have a width near 10 % of the mandrel diameter. Figure 31 is a representation of the mandrel with the wounded strip [75].

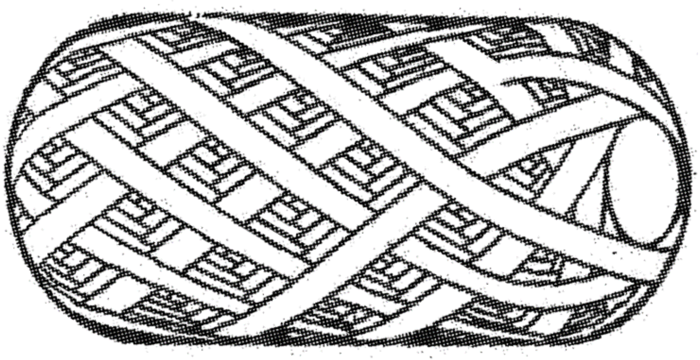

Figure 31 - Representation of the mandrel after being completely wounded with film strip, adapted from [75].

The big advantage of this method is the fact that it could be used with the same equipment used for the filament winding process. In mass production, this could be a disadvantage because it is necessary to change the machine setup for each process (if the same machine is used) [75].

3.3.1.1 Aluminized film

There are many references for using aluminized polymer films as a permeation barrier in high-pressure tanks.

In the COVESS patent, it is referred to that aluminum is very well suited as a barrier against cold and hot water or gasses such as oxygen and air [75].

Grimsley et al. studied the usage of aluminized Mylar™ film for gas permeation barrier purposes. Mylar™ is a trading name for polyethylene terephthalate (known as PET). It retains good physical properties over temperatures ranging from -70 °C to 150 °C, it is usually used in satellites for thermal protection. To improve the barrier properties, this film was coated with 99,9 % of pure aluminum by physical vapor deposition. The authors used samples with epoxy prepreg and aluminized Mylar™ films and evaluated the permeability following the ASTM D-1434 standard. The fluid used was argon gas. They compared specimens aluminized on one side with specimens aluminized on both sizes of the polymeric film and they concluded that the permeability is strongly dependent on the aluminum with better barrier performance results for the film coated on both sides [76].

3.3.1.2 EVOH film

Ethylene vinyl alcohol copolymer (EVOH) was first commercialized in 1972. It is a random copolymer with a semi-crystalline structure, consisting of ethylene and vinyl alcohol monomer units, it is usually supplied in film. Its outstanding oxygen barrier properties have made EVOH one of the most commonly used gas barrier materials in multilayer food packages. This material proved to be successful in fuel tanks to prevent fuel emissions to the environment, and to improve herbicide retention in agricultural films, among other applications [77]. Figure 32 is a graphic that compares permeability between the EVOH32 (32 % ethylene mol content) and the HDPE for different gases.

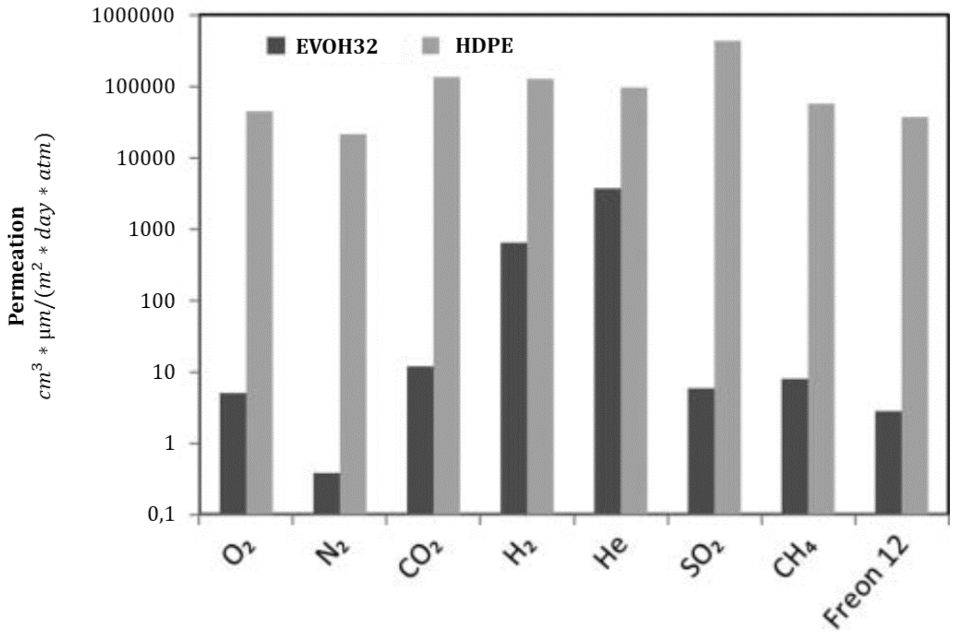

Figure 32 - Comparison of gas permeability between EVOH32 and HDPE at 23 °C and 0% relative humidity, adapted from [77].

There are some studies on the addition of nanoparticles to improve the permeation barrier capabilities of this material, one of these nanomaterials used is graphene. Kim and Lee incorporated graphene oxide nanoparticles in the EVOH32 film and they found out that 0,3 % wt of graphene oxide particles reduced the permeability of O_2 by 63 % when compared with EVOH32 pure film [78].

3.3.2 Nanoparticles

Polymers are not perfectly impermeable to gases and vapors, so it is important to enhance the barrier properties in some applications. The inclusion of impermeable lamellar fillers (e.g. clay or graphene) with sufficient aspect ratio makes the diffusing of gas-penetrant molecules follow longer and more tortuous pathways to pass through the polymer. Figure 33 represents a scheme where is possible to see the difference in the gas-penetrant molecules paths in a normal polymeric film and a polymeric film with nanofillers incorporated [79].

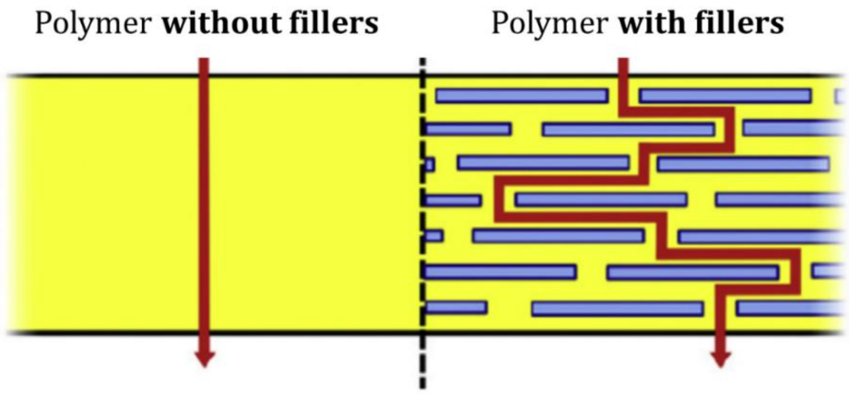

Figure 33 - Representation of the path of the gas-penetrant molecules in a normal polymeric film and a polymeric film with nanofillers incorporated, adapted from [79].

The gas barrier performance of the additivated polymer will depend on the filler properties (geometry and resistance to gas diffusion), on the barrier performance intrinsic to the polymer, and on the dispersion of the fillers in the polymer (orientation of the filler and agglomeration/free spaces) [79]. Jiao et. al has studied the effect of orienting the nanoparticles with a low magnetic field, using graphene nanoplatelets coated with Fe_3O_4 (magnetic) nanoparticles dispersed in epoxy. By scanning electron microscopy images, it was confirmed that the particles have aligned parallel to the direction of the magnetic field. The permeability was done using He gas and the gas permeability performance increased 65 % when compared with chaotic dispersed graphene nanoplatelets particles [80].

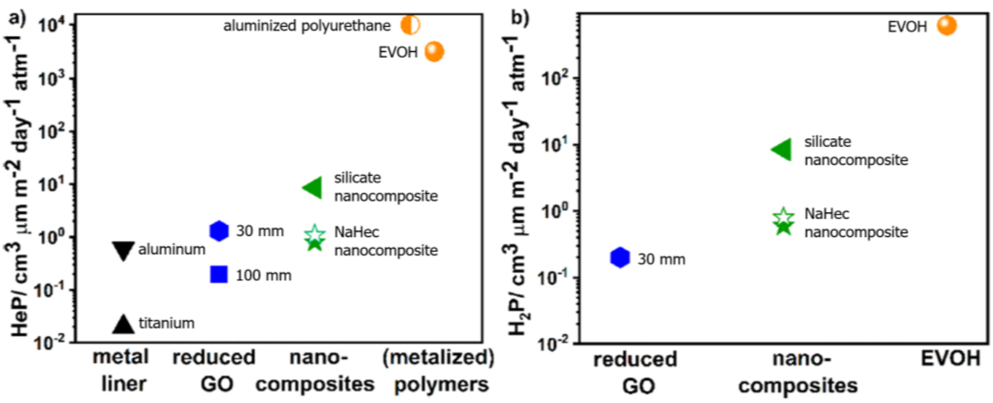

Figure 34 - Comparison of different permeation barrier materials concerning their helium and hydrogen permeabilities, adapted from [81].

Figure 34 presents two schemes describing the difference in the permeation barrier performance between the nanoparticles (reduced graphene oxide, silicate, and NaHec nanocomposites) and the traditional polymers [81].

Besides the high aspect ratio particles, some other particles could increase the crack propagation resistance such as organic rubber particles or spherical silica particles. Despite successfully enhancing the materials toughening behavior, these particles have several drawbacks, including a reduction in Young's modulus, and increasing the matrix viscosity [51, 82].

KIBOKO® is a particle toughened resin system developed by Composites Technology Development. The company discovered that incorporating nano-reinforcements into the matrix enhances resin modulus and considerably boosts inter-laminar shear strength at ply interfaces, allowing the composite material to fail only when the limits of the fiber performance are reached. CTD has also discovered that the insertion of appropriate nano reinforcements within composite plies can dramatically reduce the structure's permeability to low-molecular gaseous contents such as hydrogen [14]. Figure 35 presents a bar chart of the microcrack initiation strain value from 4 different types of laminates. It is visible the high resistance for microcracking in the laminates produced with the CTD's toughened resins.

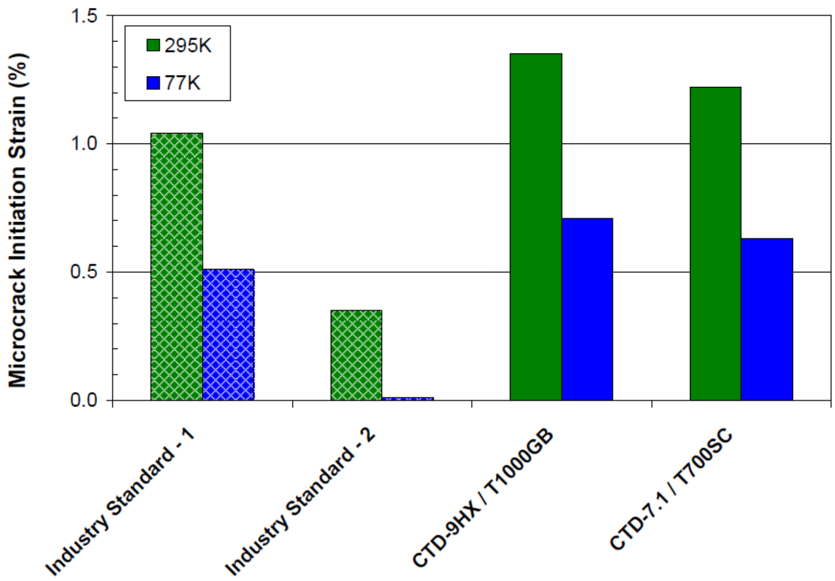

Figure 35 - Microcrack resistance of two industry-standard laminates and two CTD's toughened polymers laminate, adapted from [14]

3.3.2.1 Clay-based

Clays are widely used nanofillers for permeation barrier applications because of their high aspect ratio and compatibility with various polymers [79]. Clay represents a class of hydrous aluminum phyllosilicate minerals with an average diameter of less than 2 μm. When combined with epoxy resin, the cured material properties are noticed to be significantly increased when the clay is evenly distributed. These advantages can be seen even at very low nanofiller percentage weights [67].

Toyota researchers have found that the addition of 4 % wt of clay exfoliated in polyamide 6 has improved the elastic modulus by 90 % and 50 % in strength, however, the elongation at rupture was reduced with the increasing of clay content [67].

Due to the availability, affordability, and the high surface area-to-volume ratio of the individual clay layers, there is a lot of research on clay-layered silicates as inorganic fillers. Exfoliated clay platelets have been reported to have excellent barrier properties in nanocomposites, they are almost impermeable to small molecules like water vapor [83].

The Japanese National Institute of Advanced Industrial Science and Technology created a film called Claist®. Is primarily made of clay with a small amount of an organic binder. It is used in gas-barrier applications where is possible to have a high-temperature environment. This film is made by densely laminating clay crystals with a highly oriented structure and a platelet shape with 1 nm of thickness. Since only a small amount of organic binder is used, Claist® has a very high performance, particularly when it comes to the characteristics of hydrogen or oxygen gas barrier under high-temperature conditions. Besides these characteristics, it is also noncombustible [84]. Figure 36 is a scheme of the hydrogen leakage path through the oriented clay nanoparticles.

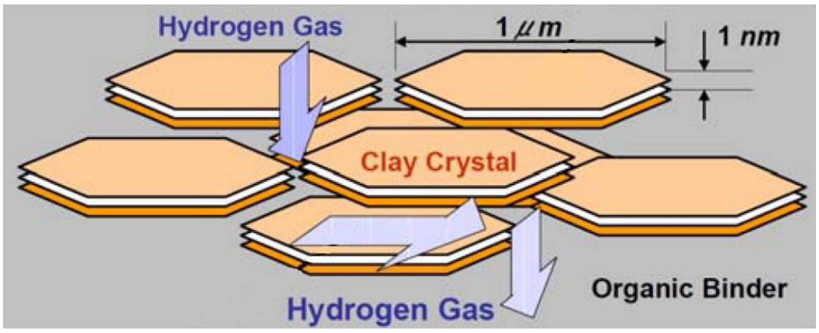

Figure 36 - Hydrogen gas permeation path through the Claist® film, adapted from [84].

Yonemoto et al. studied the gas barrier performance of incorporated Claist® film in a CFRP laminate and concluded that the permeance with hydrogen gas was two orders of magnitude lower than the CFRP alone. They made cryogenic thermal shock fatigue tests, and the permeation barrier characteristics were maintained until 100 cycles. At 1000 cycles the permeability increased drastically. The incorporation of highly oriented clays nanoparticles in CFRP could be a possible solution for a hydrogen composite tank with higher gas barrier performance [84].

3.3.2.2 Graphene-based

Graphene-based nanoparticles incorporated in polymers, compared with clays, show not only enhanced permeation barrier properties but also better mechanical strength and better electrical and thermal conductivity if properly dispersed in the polymer [79].

The high aspect ratio of graphene-based materials allows much longer paths for gas-penetrant molecules than other nanofillers. Compton et al. reported that the barrier performance of graphene nanosheets is approximately 25 to 130 times superior when compared with clay nanofillers, at low concentrations [85].

Single-layer flakes were initially separated in 2004 at Manchester University when Andre Geim and Konstantin Novoselov using sticky tape removed single layers from the surface of graphite and deposited them onto a silicon wafer. The isolation of graphene was a breakthrough and Geim and Novoselov ultimately won the 2010 Nobel Prize for Physics [86].

What was once a fascinating subject for fundamental physics is now the focus of research by academics from many different fields. While engineers create unique devices to take advantage of graphene's remarkable features, organic and materials scientists are hard at work developing new synthetic pathways to high-quality single layers [87].

Graphene is a monolayer of carbon atoms bonded in a hexagonal lattice. It has been viewed as the basic structural unit of all other graphitic carbon allotropes, including graphite, and carbon nanotubes [79]. It has an elastic modulus of 1 TPa and tensile strength of 130 GPa [88]. The surface area is around 2600 m^2/g [89]. In addition to exceptional mechanical qualities, monolayer graphene is also gas impermeable. The relatively high aspect ratio of graphene-based two-dimensional materials can undoubtedly provide significantly longer paths for gas-penetrant molecules than other nanofillers if they are fully exfoliated and evenly distributed throughout the polymer material [79]. Figure 37 presents a scheme of the different types of graphene-based particles.

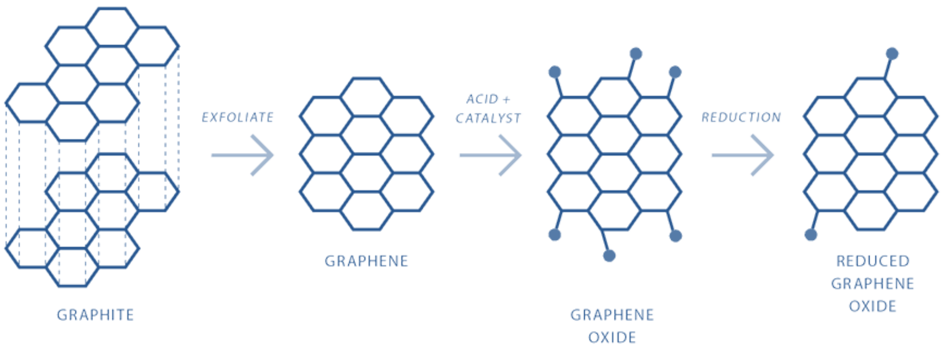

Figure 37 - From graphite to reduced graphene oxide nanoparticles, adapted from [90].

Some different graphene-based nanoparticles are defined by their production method. These particles can be produced by CVD (chemical vapor deposition), however, it is a costly solution because of the high energy consumption. The most promising approaches for large-scale production of graphene-based materials are based on exfoliation and reduction of graphite oxide [79].

Graphnest is a Portuguese company with a patented technology process to produce graphene-based particles from the liquid-phase exfoliation process. A fully green aqueous solution (organic solvent-water) is used to exfoliate graphite that is sourced from fourteen distinct locations. The van der Walls bonds between the carbon atoms in graphite are weakened by the organic solvent (with temperature control), preparing it for mechanical/physical direct exfoliation. High-quality graphene nanoplatelets can be manufactured using this method in a range of grades (from monolayer to multi-layer) and forms, dispersions, or powders [91]. A dispersion is a mixture of dispersed particles in a liquid solution. Figure 38 is a scheme of the described process.

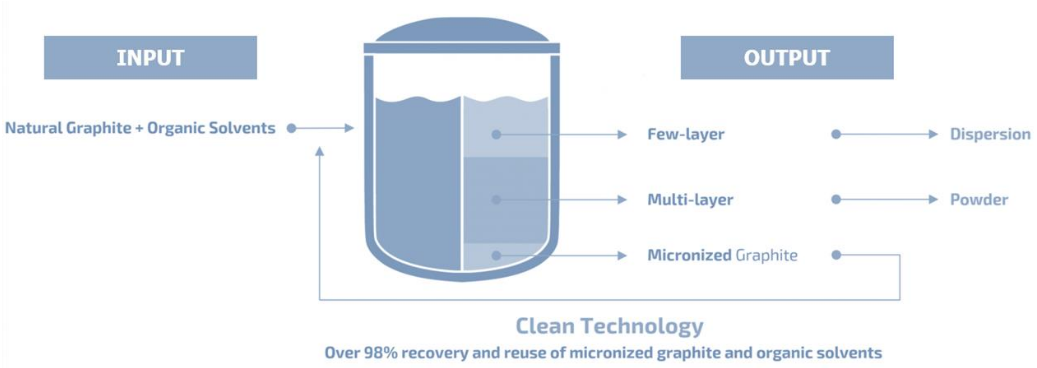

Figure 38 - Graphenest patented graphene-based particle production process, adapted from [91].

Their particles have a wide distribution size from 1 µm to 20 µm and thicknesses below 10 nm comprising 2 to 30 atomic layers of graphene for each particle [92].

Applied Graphene Materials is another graphene company that is based in the North of England and produces high-quality graphene nanoplatelets and dispersions. They have patented protected technologies to produce a range of different graphene nanoplatelets. The company argues that 1 gram of their graphene powder contains 11200 billion individual particles, 20 grams of the same powder has the equivalent surface area of an entire football pitch and that 10 grams of their graphene powder would occupy a volume of one liter [93].

They sell anti-corrosion and additive paints to use in different applications, even in the most extreme conditions such as offshore areas and those that experience high levels of salt spray. The impact of 0,1 % wt of graphene in a kg of industrial paint is to add particles with a surface area of 350 m^2, these particles will increase the tortuous path preventing the penetration of atmosphere molecules that would cause corrosion [93].

This company worked with Infinite Composites to additive their resins and enable the production of pressure vessels that outstand higher pressures and can work with cryogenic fuels. The difference in CTE between the CFRP plies can lead to cracking and leaking when exposed to cryogenic temperatures. Also, the resin system can become brittle at these extreme cold temperatures, exacerbating these issues [8]. The usage of their particles removed nearly all microfractures in resin samples after exposure to an extreme cryogenic environment, improving the permeation barrier of those structures. They also argue that the composite gets stronger over pressure cycles with the addition of graphene nanoparticles [94].

Graphene also strengthens the bonds between the layers. The resin becomes brittle and begins to fracture at low temperatures; as pressure is applied to the fibers, they begin to slide across each other, breaking the chemical bonds between them. The graphene platelets act as mechanical reinforcement between the fiber layers, decreasing their mobility and fracture [8].

Chapter 4

Development of a Linerless COPV

This academic work was done to project a COPV that has a maximum operating pressure of 30 MPa, considering a safety factor of 2, the burst pressure should be around 60 MPa.

This chapter first explains how the mandrel geometry was developed, then presents the materials used and their properties. Thereafter, it explains how the polar boss fitting design was achieved. Next, presents the steps to applicate a permeation barrier. Lastly, is an explanation of how the removable mandrel technology was chosen.

4.1 Mandrel Geometry

It was decided to produce a pressure vessel with a design similar to a high-pressure 6,8-liter pressure vessel. Figure 39 is a picture of one of these tanks. This geometry was chosen because is widely used in the high-pressure COPV market. Their design is approximately 145 mm in diameter and 460 mm in length.

Figure 39 - Example of a 6,8-litre COPV produced by CTS [95].

This was the first COPV prototype produced by the company. To simplify the geometry, due to the lack of experience with the mandrel's material and in the vessel's winding process, it was decided to reduce the length of the mandrel from 460 mm to 290 mm, making the length of the mandrel double size of its diameter. Peters recommends that the length/diameter dimensions should be less than two to prevent fiber slippage and simplify the winding process [16].

To design the dome, it was used the theoretical foundations presented in section 2.3.2, the coordinates were obtained using the trapezoidal integration method. Table 9 presents the variable values to make the dome profile coodinates generation.

Table 9 - Input parameters for the dome profile coordinate generation.

	Description	**Value**
R_F	polar boss fitting opening radius	15,2 mm
R_O	exterior radius of the polar boss fitting	40,1 mm
R	cylindrical part radius	72,5 mm
k	transversal/longitudinal stiffness parameter	0,1

Microsoft Excel was used with steps of 0,3 mm to generate the r values. The winding simulation software's are usually limited to a certain number of points that compose the mandrels geometry. CADWIND, for example, is limited to mandrels composed of 400 points. Using a 0,3 mm step each dome would have 191 points composing its coordinates and leaving 18 points available to write the coordinates in the cylindrical part of the vessel. Table 10 presents an example to explain how the coordinates were generated.

Table 10 - Coordinates generation table using the trapezoidal integration method.

r	$x = r/R$	$y_1(x, k, x_B)$		Z/R	Z
(···)	(···)	(···)	(···)	(···)	(···)
42,2	0,58207	- 0,40365	- 0,00168	- 0,0139	- 1,0076
42,5	0,58621	- 0,40955	- 0,00171	- 0,0139 + (- 0,00171) = - 0,0156	- 1,1313
42,8	0,59034	- 0,41553	- 0,00173	- 0,0156 + (- 0,00173) = - 0,0173	- 1,2569
43,1	0,59448	- 0,42158	- 0,00176	- 0,0173 + (- 0,00176) = - 0,0191	- 1,3843
(···)	(···)	(···)	(···)	(···)	(···)

$$* -0{,}00171 = \frac{(-0{,}40955) + (-0{,}41553)}{2} \cdot (0{,}59034 - 0{,}58621)$$

The above table presents the method utilized to generate the coordinates from the radius of 40,1 mm to the cylindrical part. From 15,2 mm to 40,1 mm the method was the same but using Eq. (16).

There were some adjustments made for the integration methodology to be functional between the 15,2 to 72,5 mm interval (like increasing the R value in some decimals).

In the end, an Excel file was created relating the r and Z values. It was uploaded in the Autodesk Inventor CAD design software and the profile presented in Figure 40 was created.

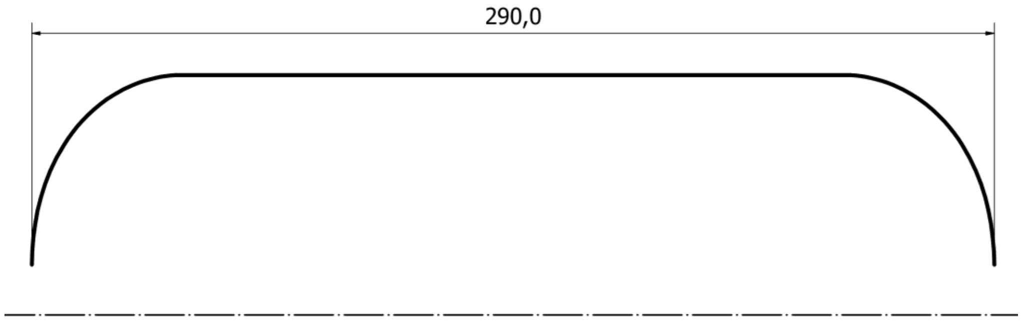

Figure 40 - Final mandrel profile.

4.2 Composite System Selection

The available production process of COPVs at FHP was wet filament winding. The carbon fiber available to use was the high-strength TEIJIN Tenax™-E HTS45 E23 carbon fiber. The resin matrix available to use was the Olin LITESTONE® 2130E epoxy resin with the 2142H Hardener used in industrial and structural composites, pressure vessels, and sporting goods. This system has low viscosity and a long pot life at ambient temperatures. Table 11 presents some of its properties.

Table 11 - Considered properties of the Olin resin [96].

E	2,6 GPa
ν *	0,35
Tensile strength	75 MPa
Elongation at break	5,2 %
Viscosity at 25 °C	400 - 600 mPas
Gel time at 25 °C	> 48h
Gel time at 90 °C	20 - 30 min
T_g	120 - 130 °C

*assumed value: 0,35 is a typical value for an epoxy thermoset.

The Tenax™ carbon fiber datasheet only presents the fiber tensile modulus in its principal direction. To calculate the unidirectional ply stiffness properties, it was used Abaqus WCM Micromechanics module which is based on the rule of mixtures. The elastic properties of the fiber in the transversal direction were needed too. Donnet et al. presented in their book the elastic properties of the Amoco T-650 carbon fiber [97]. Mounier et al. studied the transverse elastic properties of the Torayca T700 carbon fiber using laser resonant ultrasound spectroscopy and conclude that the transversal tensile modulus of the fiber was 1/15 of the longitudinal one [98].

The Amoco T-650 longitudinal elastic modulus is 243 GPa, a value very similar to the HTS 45 E23 carbon fiber (240 GPa). The value for the transverse elastic modulus is 13,8

GPa. It is an acceptable value when compared with the Mounier et al. study. The considered mechanical properties values for the HTS 45 E23 fiber are presented in Table 12.

Table 12 - HTS 45 E23 carbon fiber considered properties [99].

E_{11}	240 GPa
E_{22}	13,8 GPa
ν_{12} and ν_{13}	0,29
G_{12} and G_{13}	23,1 GPa
G_{23}	5,0 GPa
Tensile strength	4500 MPa
Elongation at break	1,9 %
Density	1,77 g/cm^3
Number of filaments	12000
Nominal linear density	800 tex

It was possible now to determine the properties of a unidirectional laminate using the mechanical properties of the epoxy resin and carbon fiber. This calculation was done in Abaqus WCM using the Micromechanics module, it calculates these properties by simulating uniaxial states of stresses in the composite. It assumed a fiber volume content of 60 %, which is a typical value, as described in section 2.3.1. Table 13 is the calculated stiffness properties of the ply.

Table 13 - Abaqus WCM calculated stiffness properties of the unidirectional ply.

E_{11}	145,04 GPa
ν_{12} and ν_{13}	0,312
E_{22} and E_{33}	6,48 GPa
ν_{21} and ν_{31}	0,014
ν_{23} and ν_{32}	0,412
G_{12} and G_{13}	3,36 GPa
G_{23}	2,29 GPa

4.3 Netting Analysis

The chosen geometry has an interior radius of 72,5 mm, a MEOP of 30 MPa with a minimum burst pressure of 60 MPa. It was considered a fiber volume fraction of 60 % with a bandwidth of 5 mm, the winding software calculated that the helical wind angle was 12,02 ° and the hoop winding angle 89,37 °.

The helical and hoop allowable stress were inputted in calculus with a factor of 0,7 and 0,93 respectively, values used by Peters in an example presented [16]. The stress ratio was around 75 %, a value recommended by Madhavi et al. (60 % to 80 %) to prevent failure in the dome or by boss blowout [100]. If the fiber tensile strength value is 4500 MPa, the allowable stress for the helical layers is 3150 MPa and for the hoop layers 4185 MPa. The fiber elastic modulus is 240 GPa. The loads can then be defined as:

$$N_{\emptyset} = \frac{2 \cdot 30 \cdot 72{,}5 \cdot (1 + 4185/240000)}{2} = 2213\ \mathrm{N/mm}$$

$$N_{\theta} = 2 \cdot 30 \cdot 72{,}5 \cdot (1 + 4185/240000) = 4426\ \mathrm{N/mm}$$

The total fiber thickness can then be calculated as:

$$t_{hel} = \frac{4426 \cdot \cos^2 89{,}37 - 2213 \cdot \sin^2 89{,}37}{3150 \cdot (\cos^2 89{,}37 \cdot \sin^2 12{,}02 - \sin^2 89{,}37 \cdot \cos^2 12{,}02)} = 0{,}734\ \mathrm{mm}$$

$$t_{hoop} = \frac{4426 \cdot \cos^2 12{,}02 - 2213 \cdot \sin^2 12{,}02}{4185 \cdot (\cos^2 12{,}02 \cdot \sin^2 89{,}37 - \sin^2 12{,}02 \cdot \cos^2 89{,}37)} = 1{,}034\ \mathrm{mm}$$

To calculate the thickness of the final composite, it is only needed to divide the fiber thickness by the fiber volume fraction. The helical layers have a final thickness of 1,223 mm, the hoop layers are 1,723 mm and the final composite thickness in the cylindrical region is 2,946 mm. These results should be tuned by changing the allowable stresses for the helical and hoop layers, and it should be compared with a FEA to understand if this was a conservative way of quickly calculate the COPV wall thickness.

4.4 Polar Boss Fitting

To develop the polar boss fitting part, first, it was chosen the material and then the design was created. First, it was used the Peters formulation to have an order of magnitude of the fitting size, and then it was used Abaqus WCM to make simulations of different instances in an iterative way to tune the design.

4.4.1 Material Selection

Regarding other linerless COPV projects, some of them used aluminum alloys as the polar boss material, and others used stainless-steel alloys.

The aluminum has the advantage of having a higher specific strength that makes the part lighter, which is something very important in this type of pressure vessel technology. The disadvantage of aluminum over stainless steel is the higher coefficient of thermal expansion. In the curing step, the higher CTE of aluminum promotes more stress in the dome region which could promote the non-adherence between the CFRP and the polar boss. Iqbal in his Master's Thesis project used aluminum alloy A380 for the polar boss fitting of a linerless tank [67].

The stainless steel alloys have the disadvantage of a smaller specific strength than aluminum alloys but have the advantage of a lower CTE that would promote less stress in the CFRP curing step, besides that, since this project has the goal of projecting a COPV for space applications it is important to choose a material that would minimize the CTE effects in a big range of temperatures (that is a characteristic of the space environment).

The chosen material for the polar boss fitting was the stainless steel AISI 304. It was important to minimize the chances of failure in the adhesion of the polar boss with the CFRP in a so preliminary phase of this project and furthermore, this material is used in commercial linerless COPVs such as Infinite Composites products.

The considered properties for the AISI 304 stainless steel are presented in Table 14.

Table 14 - Considered properties of the 304 stainless steel [101].

Elastic Modulus	200 GPa
Poisson's Ratio	0,29
Shear Modulus	86 GPa
Tensile Strength, Yield	210 MPa
Tensile Strength, Ultimate	505 MPa
Elongation at Break	70 %
Hardness, Vickers	129
Density	8 g/cm^3

4.4.2 Specifications

For the interface between the polar boss fitting and the external gas installation, first, it was idealized a boss with a flange interface like the one presented in Figure 41.

Figure 41 - Polar boss interface in an Infinite Composites pressure vessel, adapted from [102].

Soon, it was understood that in the small-diameter vessel geometry chosen, the polar boss fitting would be too big. The sealing system should be designed to hold 60 MPa of gas pressure and it was a problem too. It was difficult to find solutions for these specifications. Another problem with this flange solution was the hypothesis of colliding with the machine head in the filament winding process.

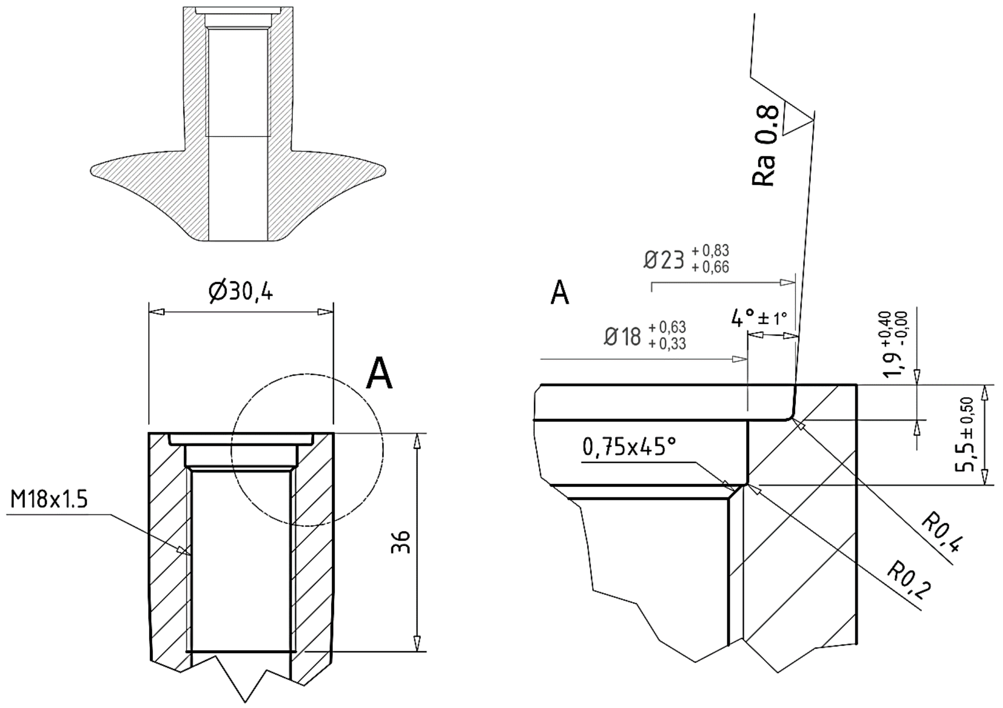

Figure 42 - Polar boss fitting threaded interface dimensions according to ISO 15245-1:2021.

The solution chosen for the polar boss fitting interface was a high-pressure valve threaded system, the common inlet connections are M18x1,5, M25x2, E17con, or 25E. In this case, it was chosen the M18x1,5 threaded connection that is under the standard ISO 15245-1:2021.

It was determined that the polar boss fitting neck had a diameter of approximately 30 mm, resulting in a boss wall thickness of 6 mm. Figure 42 is presented the interface connection chosen for the polar boss fitting.

4.4.3 Geometry

To develop the geometry of the polar boss, it was used first the equations presented by Peters and Vasiliev described in section 2.3.3.

The parameters used in Peters equations to calculate the polar boss thickness are:

- Port radius (R_F) - 15,2 mm;
- Exterior radius of the polar boss (R_O) - 40,1 mm;
- R_{NX} is calculated using equation (20) - 23,5 mm;

- P_{ULT} is the ultimate design internal pressure - 60 MPa;
- σ_{ULT} is the polar boss allowable stress - 210 MPa.

The polar boss allowable stress (σ_{ULT}) was chosen to be 210 MPa because is the approximate value for the 304 stainless steel yield strength. This value was considered without a safety factor, so the final result gives the minimum value for the polar boss thickness.

$$\mathrm{T_F} \geq 22{,}1 \text{ mm}$$

The Vasiliev formulations could not be used because the graphic that gives the maximum normalized radial bending moment has the value of R_O/R_F limited to 1,5 and in this case this value is 2,6. Having a big difference between R_O and R_F causes a bigger bending moment that is not beneficial to the composite and the polar boss stress, but was important in an early stage of the linerless development project to increase the contact surface area to increase the probability of adhesion between the polar boss and the CFRP. It also increased the weight of this part which is undesired when developing a linerless COPV.

After the calculation of the recommended thickness with the formulation proposed by Peters, Abaqus WCM was used to make an iterative geometry development.

The coordinates of the vessel profile were uploaded, and it was only considered half a vessel. The simulations were done using an axisymmetric modulation with static analysis, the element type used was CAX4. The polar boss part was created after the composite generation, starting the polar boss part design with the composite dome Abaqus sketch. Figure 43 is a scheme of the Abaqus model developed.

The boundary conditions used were the locking of displacement in the vertical direction and rotation in the plan and the horizontal direction for the bottom nodes in the cylindrical part.

Utilizing the contact type interaction property with tangential behavior and a friction coefficient of 1,0, the interaction between the polar boss surface and the composite inner surface was created. This was a simplified way to avoid slipping between the two surfaces, but the best way to make this simulation was to use cohesive elements. These elements are commonly used when modeling adhesive joints.

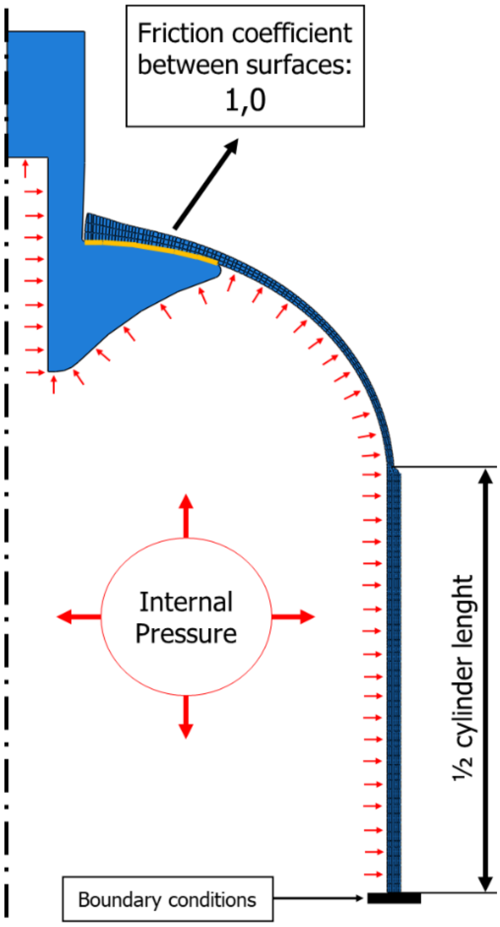

Figure 43 - Axisymmetric Abaqus model of the linerless COPV.

The composite layers were selected taking into account the netting analysis calculus. The total hoop layer's thickness was 1,723 mm and the helical ones were 1,223 mm making up a total composite thickness of 2,946 mm. The hoop layers were rounded for a thickness value of 0,45 mm and the helical ones for 0,4 mm. Four hoop layers and three helical layers were used making the final thickness 3 mm. A screenshot of the winding lay-up used in these simulations is shown in Figure 44.

Winding Layout

	Active	Layer Type	Material	Thickness	Wind Angle	Inner Radius	Outer Radius	Hoop Height	Band Width
1	☑	HELICAL_FRIC	HTS45 Carbon Fiber	0.4	15	15.2			8
2	☑	HOOP	HTS45 Carbon Fiber	0.45	80.0			0.0	
3	☑	HELICAL_FRIC	HTS45 Carbon Fiber	0.4	15	15.2			8
4	☑	HOOP	HTS45 Carbon Fiber	0.45	80.0			0.0	
5	☑	HELICAL_FRIC	HTS45 Carbon Fiber	0.4	15	15.2			8
6	☑	HOOP	HTS45 Carbon Fiber	0.45	80.0			0.0	
7	☑	HOOP	HTS45 Carbon Fiber	0.45	80.0			0.0	

Figure 44 - Winding lay-up used in the Abaqus WCM simulations.

It was done 12 simulations in Abaqus WCM testing different geometries in an iterative process. The part was created using the Abaqus sketching tools, the 304 stainless steel elastic properties were assigned, the interaction between the polar boss and the CFRP was created, and then the 60 MPa pressure load was created in the inner surface of the pressure vessel.

The von Mises criteria was used to evaluate the polar boss part stress. It was selected a limit of 210 MPa in the color scale (approximately the yield strength of the AISI 304 stainless steel) to identify the locations where the part would start plasticizing. The aim was to have a part with the minimum chances of plasticizing and minimum weight.

The geometry decision was an iterative trial and error process. It will be presented below the different geometries tested (from Figure 45 to Figure 56).

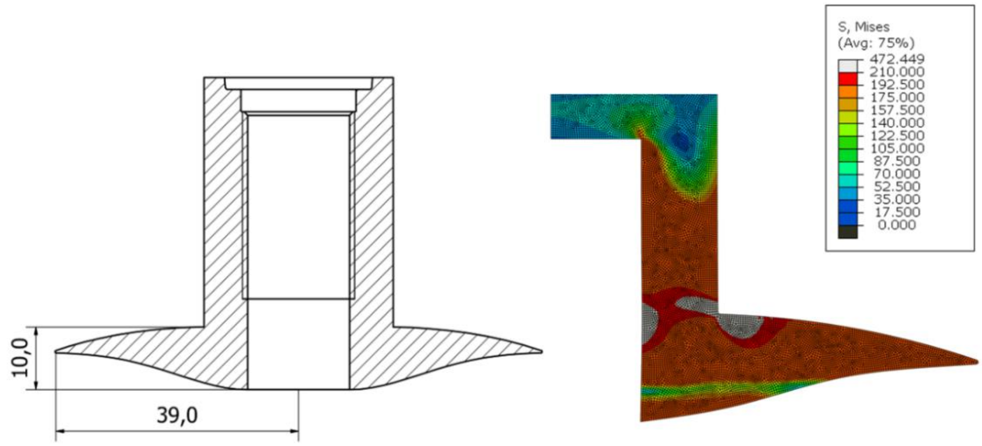

Figure 45 - Polar boss geometry test number 1.

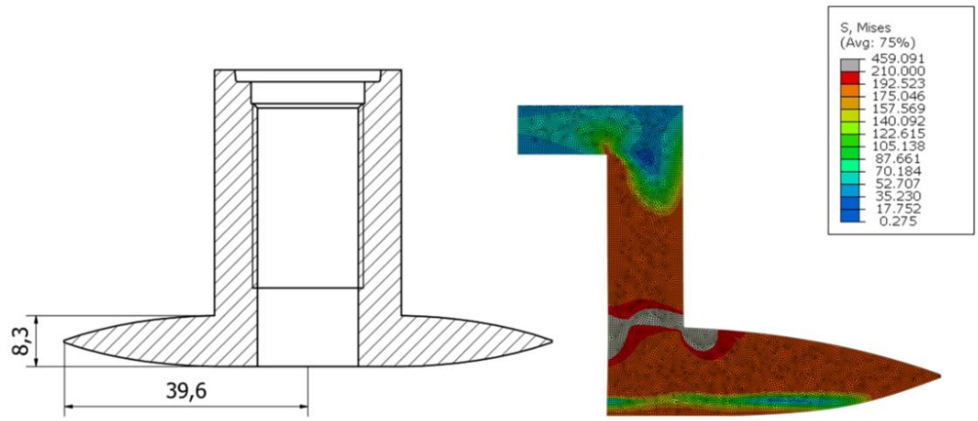

Figure 46 - Polar boss geometry test number 2.

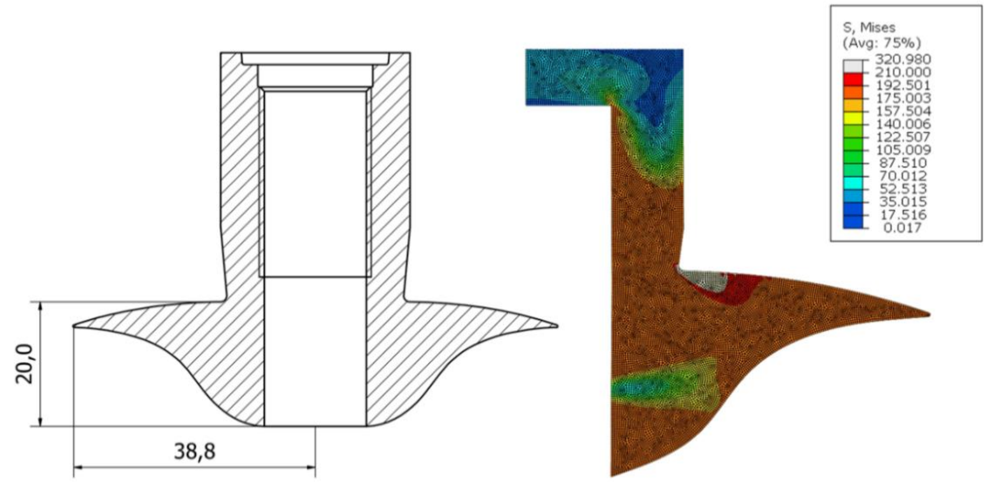

Figure 47 - Polar boss geometry test number 3.

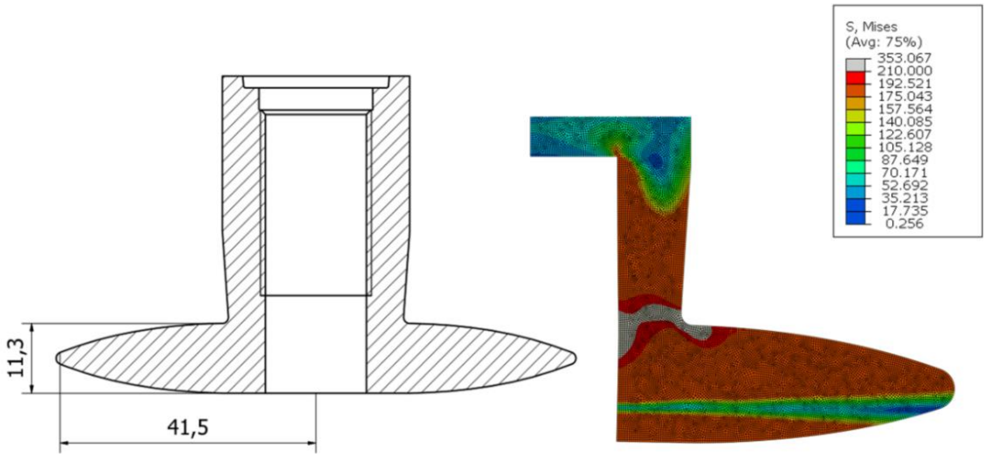

Figure 48 - Polar boss geometry test number 4.

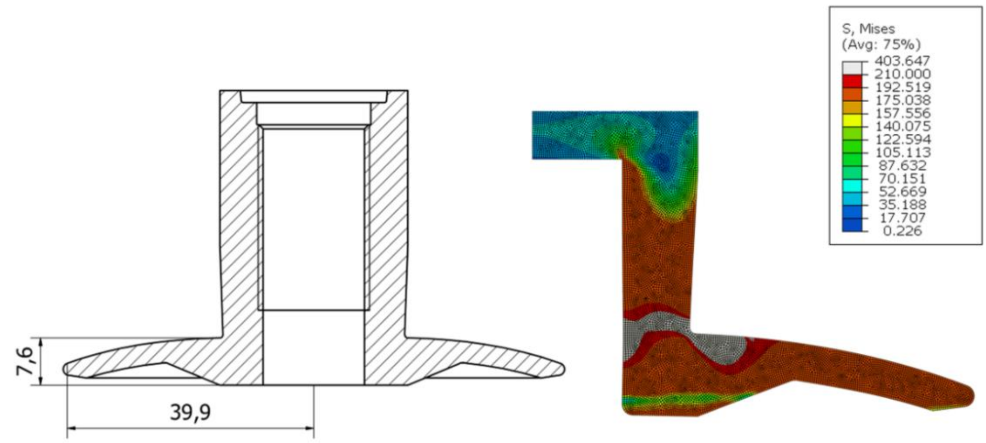

Figure 49 - Polar boss geometry test number 5.

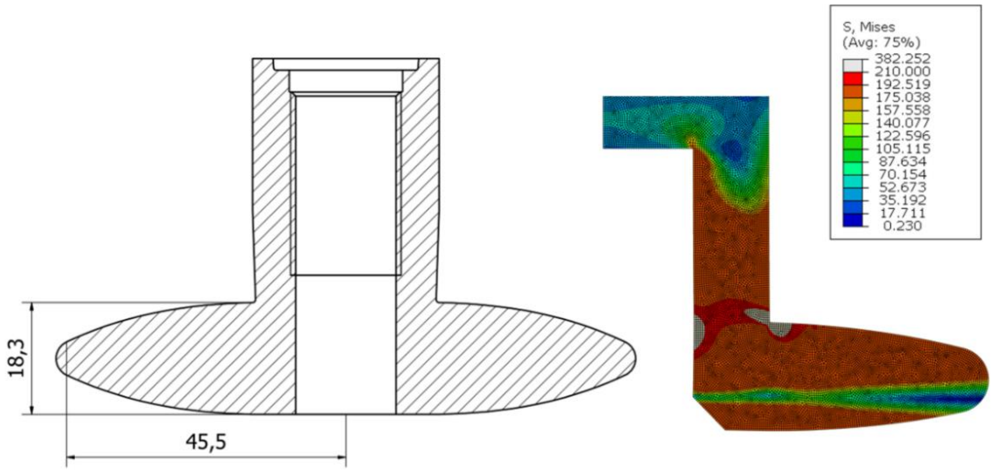

Figure 50 - Polar boss geometry test number 6.

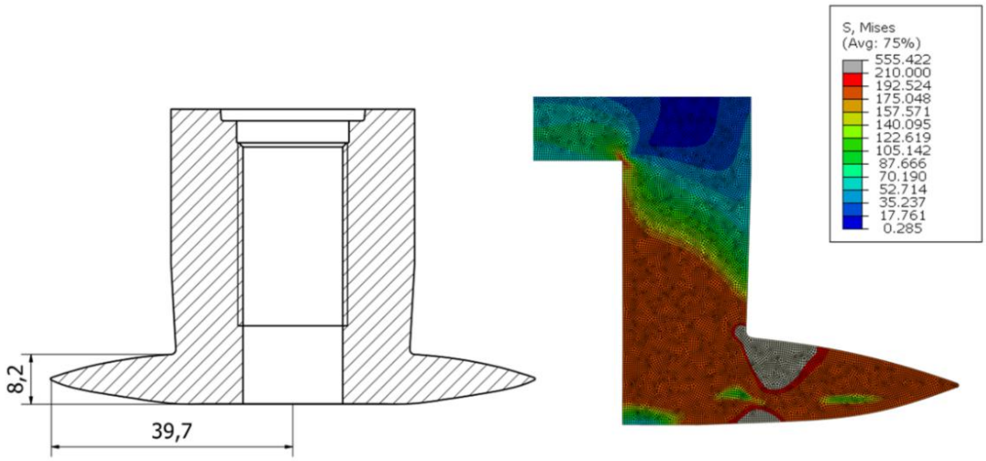

Figure 51 - Polar boss geometry test number 7.

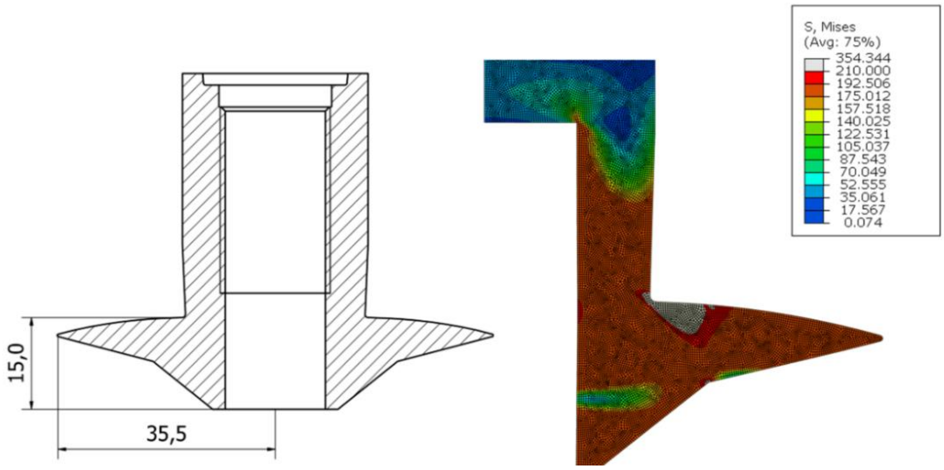

Figure 52 - Polar boss geometry test number 8.

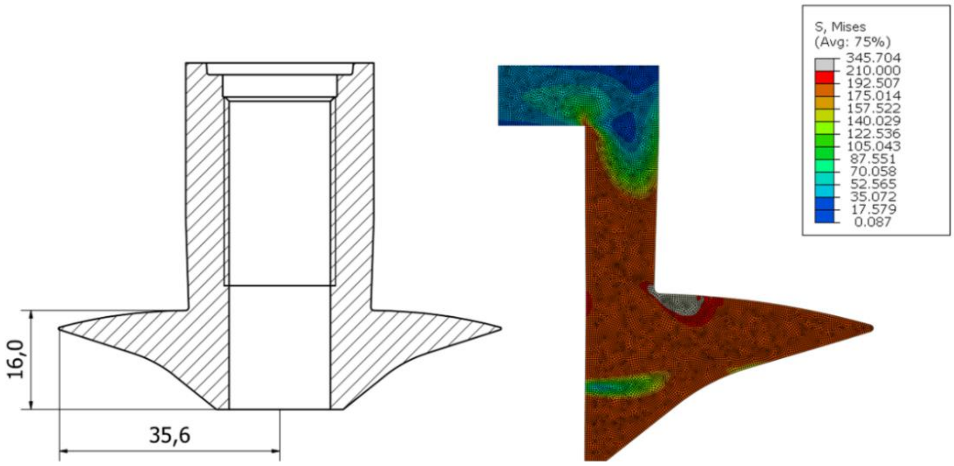

Figure 53 - Polar boss geometry test number 9.

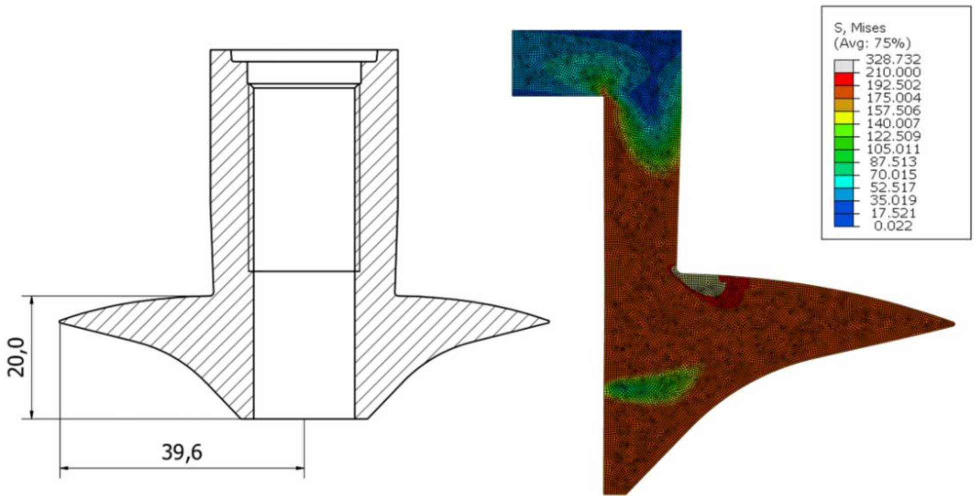

Figure 54 - Polar boss geometry test number 10.

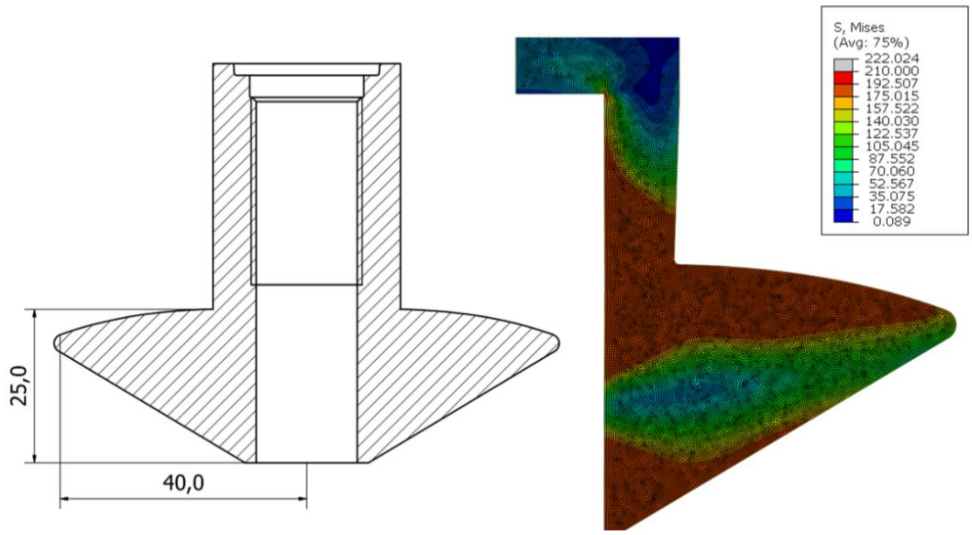

Figure 55 - Polar boss geometry test number 11.

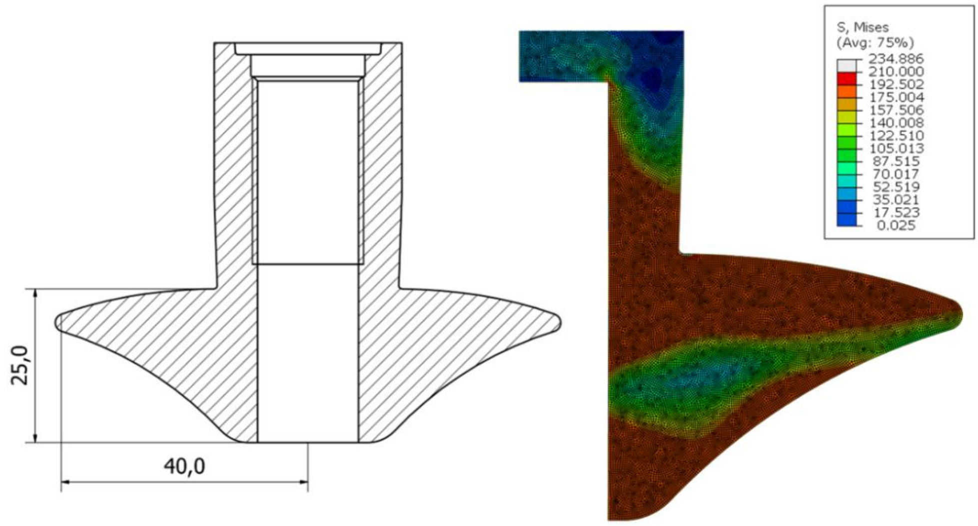

Figure 56 - Polar boss geometry test number 12.

To resume all the simulation results, Table 15 presents the von Mises maximum stresses ordered in ascending order.

Table 15 - Summary of results with von Mises maximum stress ordered in ascending order.

Test number	Thickness mm	Exterior radius mm	Von Mises Maximum Stress MPa
11	25,0	40,0	222,0
12	25,0	40,0	234,9
3	20,0	38,8	321,0
10	20,0	39,6	328,7
9	16,0	35,6	345,7
4	11,3	41,5	353,1
8	15,0	35,5	354,3
6	18,3	45,5	382,3
5	7,6	39,9	403,6
2	8,3	39,6	459,1
1	10,0	39,0	472,4
7	8,2	39,7	555,4

The iteration began with a low-weight polar boss geometry. The plan was to have a robust central portion that would get thinner as it got closer to the polar boss's edges. This design geometry type was applied also in tests number 3, 8, 9, and 10. The idea was to have a solid central boss part that would suffer elastic strain in its thinner parts accompanying the strain that the composite suffers under pressure.

The adhesion of the CFRP-boss interface could be stressed by an all-rigid polar boss since the CFRP would deform under pressure, but the metallic component, which would be rigid, would not experience the same strain.

The aim of the geometries used in test numbers 2, 4, and 6 was to have an approximately symmetrical profile in the CFRP contact surface and on the inner surface under internal pressure. Nearly symmetrical distribution of load in this part could benefit the appearance of a plasticized strain peak.

Test number 7 was an attempt to understand if increasing the polar boss neck diameter would help avoid plasticized sections. The part has plasticized and had the highest value of von Mises stress. The dome geometry was not updated to this geometry, and this was a potential aggravating factor.

Analyzing Table 15 is visible that having a central thick section is the mechanism for creating a more robust part. Test number 11 was the part that had the minimum von Mises Maximum stress. It was decided to give a more curved shape to this piece generating the last and final iteration, the test number 12 part. It suffers some plasticizing but is negligible. It was finally the design chosen to construct the polar boss part.

Analyzing Figure 57 is possible to see the composite-boss interface at the maximum pressurization point where is visible that the surfaces did not separate from each other. It was interesting to understand if depressurizing would induce separation between these surfaces. However, the plastic material properties were not employed in the simulation so the piece would return to its original form along with the composite material. Furthermore, it was not expected that this situation could happen in a real situation with the pressure vessel, the currently applied load is 60 MPa and the MEOP is 30 MPa. At this load level, plasticization would not occur.

The final part weight was 611 g calculated using the Autodesk Inventor CAD software.

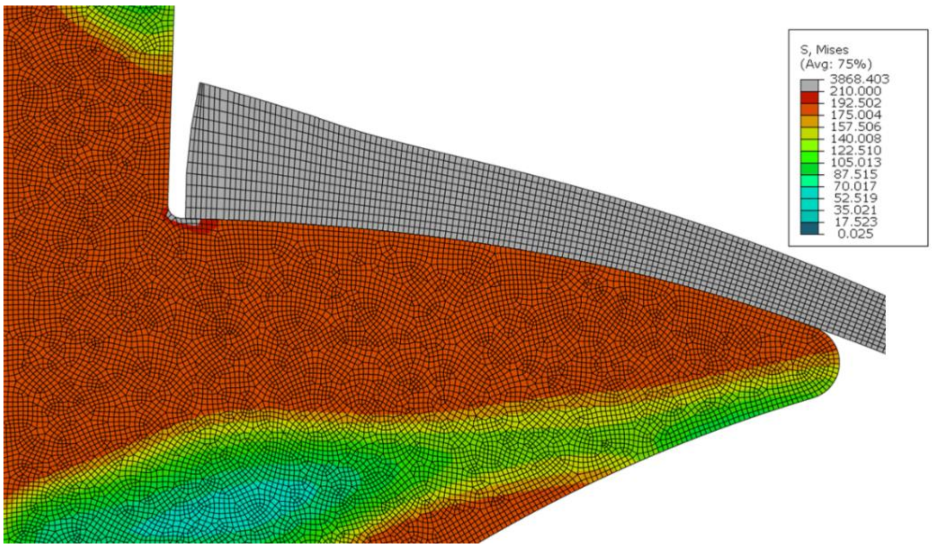

Figure 57 - Interface between the test number 12 part and the composite pressurized at 60 MPa

.

4.5 Permeation Barrier

With the help of the Applied Graphene Materials company, it was mapped out a route to apply permeation barrier mechanisms in the production of linerless COPVs.

Using the Olin LITESTONE® 2130E epoxy resin with the 2142H Hardener, it would be possible to disperse graphene nanoparticles. A sample of resin would be sent to the Applied Graphene Materials facilities, and they would make the dispersion of particles in this sample. These are reduced graphene oxide particles that are usually used to improve fracture toughness in pre-preg resins and filament winding systems.

The sample would then return to the FHP facilities and would be mixed with the rest of the matrix components using a dissolver mixer. Figure 58 is a photo of a dissolver mixer head. This additivated resin matrix would be used in the wet filament winding process.

Figure 58 - Dissolver mixer head, adapted from [103].

Besides the additivated matrix, a permeation coating would be applied to the top of the mandrel before beginning the filament winding process, making it an interface between the CFRP and the pressurized gas or liquid. Another methodology to apply this permeation barrier was to apply it inside the pressure vessel after the curing step and ceramic removal process. It was needed to have a process to homogeneously distribute the liquid permeation coating and to cure it if the desired base material was a thermoset material like epoxy.

This permeation coating would have as a base, the same epoxy used in the CFRP matrix, but additivated with other high-quality graphene particles supplied by Applied Graphene Materials.

If more additives would be added to this permeation coating resin, it is recommended that they are mixed before the graphene-based particles to avoid breaking them. These particles could be rubber particles that would increase the flexibility of the epoxy as presented in section 3.3.2. Increasing the flexibility would prevent the emergence of microcracking at a low strain level of the composite. Infinite Composites argues that they use two additives to the resin matrix, one is graphene particles and the other is an additional proprietary additive that makes the laminate more ductile at low temperatures and creates more insulative properties in the laminate [8].

Because of time constraints, it was impossible to apply a permeation barrier in the first linerless prototype. There was also a lack of experience in the general production of COPV and the priorities were to tune the filament winding process. A permeation barrier would be something to apply after achieving a developed stage for the structural and production COPV steps.

4.6 Mandrel Material Selection

The metallic collapsible and inflatable tools are solutions time and cost-intensive and would be very difficult to apply in this case. These solutions should be considered in large productions. It is unfeasible to apply this solution in a prototype or a low-series production.

The shape memory polymer Smart Tool is impossible to implement in the pressure vessel mandrel because the small opening of the tank will not allow the removal of the softened material after the curing step. In addition, it would be very difficult to fix this polymer tool to the filament winding shaft.

The shape memory foam reviewed cannot be used as the mandrel tool because this foam is only able to reduce its volume from 10 % to 20 % and it is impossible to remove the tool from the produced COPV with this small volume reduction. It would have been possible if the tank opening was large enough. The company argues that the MUPET™ technology could be used to manufacture large composite tanks for NASA launch vehicles making it possible to join the fuel and oxidizer (which are usually two different tanks) in a single tank with two compartments [47].

The PVA mandrel solution is a potential use for washable mandrel production, but it is a material difficult to find in commercial solutions that could supply PVA blocks to be machined. The 3D printed solution could be considered, but the PVA filament is an expensive material and the prices range from 57 € to 123 € per kilogram [104]. Moreover, there is not much literature about the usage of this single material in a mandrel, so it was not considered.

The sand/sodium silicate solution could be a possible solution because it was already used with success to produce a COPV by Iqbal [67]. The advantage of this solution is the low cost of raw materials. However, this solution is very complex and requires a lot of steps to produce and dismantle the mandrel. It requires a specific mold with tunnels for the hardening process, requires a vibration machine to ensure the entire filling of the sand in the mold, and requires a specific mold for each different geometry of the tank. Moreover, the dismantling process is very time and labor-consuming and for those reasons, this solution was not considered too.

The ExOne 3D printing ceramic that can be washed out by water is a very promising technology to produce the sacrificial mandrel. The problem with this solution is that this printing capability is not available in Europe at the time this work took place. There are ExOne 3D printers in Europe but none of them is using water-soluble binders. The only solution was to import the printed mandrel from the ExOne facilities in the United States of America. This solution was considered, the price for the first idealized 6,8-litre vessel mandrel geometry was around 375 € with a PTFE coating, and the lead time was 4 weeks plus shipping time.

The Advanced Ceramics Manufacturing products were the most promising solutions since they have a wide range of products that could be possible to use as the pressure vessel mandrel and they are represented in Europe by a Swedish company called Aero Consultants AG.

4.6.1 Options Comparison

The ExOne 3D printed mandrel could be an option since it holds up to 180 °C of curing cycle temperature. The problem with this solution is that the mandrel had to be shipped from the USA, the shipping price was around 150 €. From the adjudication of the mandrel production order to the delivery could be around 6 weeks and that was impracticable for this thesis project.

Advanced Ceramic Manufacturing products were the most promising solutions for this project. When consulting Aero Consultants AG they offered the solution of supplying the ready-to-use mandrel wrapped with PTFE. The CAD file of the mandrel was sent to them and the shaft to fix the mandrel would be sent too. They were responsible for producing the mandrel and fixing it to the shaft. When asking for a quotation for this solution they gave the price of 5300 € for one unit mandrel and 3500 €/unit if the asked quantity were two units. It was then asked the price for the Advanced Ceramic Manufacturing products so the mandrel can be fabricated in-house. Table 16 is the price list that was given.

Table 16 - Advanced Ceramics Manufacturing price list from Aero Consultants AG.

Product	Volume / Dimensions	Price per unit
Aquacore™	18,9 liters	199,00 €
Aquapour™	18,9 liters	199,00 €
Aqua Block	620 x 620 x 80 [mm]	310,00 €
	620 x 620 x 150 [mm]	684,00 €
Aqua Tool Adhesive™	1,89 liters	189,00 €

The Aqua Block is a block made from Aquacore™ that is supplied ready to be machined, the advantage of this product over Aquacore™ is that is not necessary to fabricate the block from the powder.

If the Aquacore™ product was chosen, it would have been necessary to have a mold to compress the powder and an oven that was large enough to put the block. Then, it was necessary to machine the block to the pressure vessel interior design.

If the Aquapour™ product was chosen, it would have been necessary to have a mold with the internal shape of the pressure vessel so that the liquid mixture could be shaped to the internal design of the pressure vessel.

If the Aqua Block product was chosen, it would have been necessary to decide what block was the best to choose. The diameter of the pressure vessel mandrel is 145 mm. If the 80 mm height block was chosen, it was necessary to machine the two halves of the pressure vessel mandrel (split axially) in a CNC milling machine and then bond them together, the other option was to split the block into two halves, glue them together and then machine the bonded block. If the 150 mm block was chosen, it was only necessary to cut a ¼ of the block and then machine it in a CNC lathe.

Next, a summary of considered options is presented.

4.6.1.1 Aquapour™

The advantage of this solution is that is not needed many steps for mandrel production. It is only necessary for the mold with the internal shape of the pressure vessel and an oven to dry the material. The steel rod can be included into the mold to secure the ceramic to the shaft, for example, by using indentations in the steel part.

The disadvantage of this solution is that the mold will be a very complex and expensive tool that will only justify making if the mandrel would be mass production. The other disadvantage is that the Aquapour™ product is more complex to work with than the other materials, and defects are more common than the other Aqua products. Figure 59 presents some of its common defects.

Figure 59 - Aquapour™ production common problems, adapted from [105].

4.6.1.2 Aqua Block

The advantage of this solution over the Aquacore™ is that the block was ready to machine. This would avoid problems because there is a lack of experience in working with these materials and costs around the block making.
The disadvantage of this solution is that the blocks have a parallelepiped shape and it is necessary to machine them to a cylindrical shape which generates a lot of waste material that could be saved. Another problem is that the blocks must be stored in vacuum because humidity can ruin the ceramic. The cost of shipping would be high for these products because they had to be transported in a pallet.

4.6.1.3 Aquacore™

The advantage of this solution is that there is freedom of creating the blocks in terms of size and shape. It gives the possibility of creating cylindrical blocks instead of parallelepiped blocks and this is a big advantage when producing pressure vessel mandrels, the cylindrical shape implies less waste and time in the machining step. Another advantage of this product is the simpler storage.

The disadvantage of this solution is that it requires more labor work and equipment to produce the blocks. Although, this was the chosen solution. It was the cheaper and most interesting solution.

Chapter 5

Experimental Characterization

After the review of production parameters and steps to be accounted for in the development of a linerless COPV, it is next presented the experimental characterization to obtain a linerless tank prototype. This chapter explains all the setups used in the production of the linerless pressure vessel. Then, all the steps for the removable mandrel production are presented. Next, it is presented tests that were done to understand the adhesion between the polar boss surface and the CFRP. Finally, the different phases of the linerless COPV production are explained, from the filament winding process to the ceramic mandrel removal.

All results and comments for this experimental work are presented in section 6.

5.1 Manufacturing Setup's

To produce the linerless COPV was necessary first to produce the Aquacore™ mandrel, then to fix the mandrel to the filament winding machine to overwrap it with CFRP, and then cure the overwrapped tank in the oven.

5.1.1 Mandrel Assembly

To have more freedom in the length of the pressure vessel, it was decided to produce the Aquacore™ mandrel in many parts and then join them in the same shaft. Figure 60 represents the assembly of the two blocks in one mandrel.

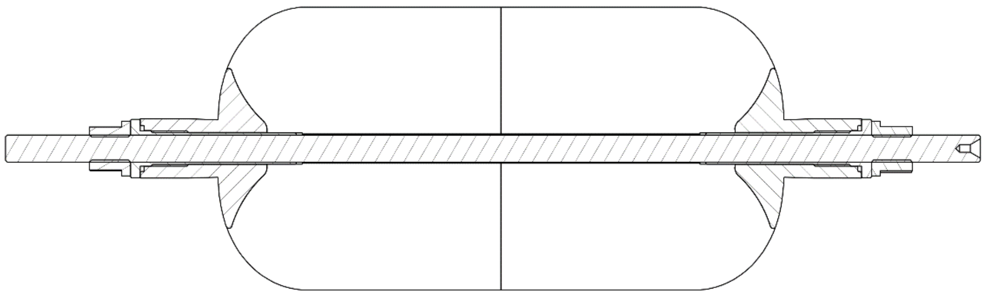

Figure 60 - Scheme of the two blocks assembly in one mandrel.

The decided geometry has two equal openings. Therefore, the shaft could pass all over the mandrel. The advantage of making the mandrel in many parts and then joining them is that the cylindrical mold can be shorter which makes the compressing step easier.

The other advantage of producing the mandrel with more than one Aquacore™ block is that the fixation in the machining center is easier.

If one opening solution was applied, the different Aquacore™ blocks could be glued together using Aqua Tool Adhesive™ product.

Since the boss polar fitting has an M18x1,5 threaded hole the shaft that would pass through the mandrel have to be less than 16,5 mm (subtracting the pitch to the thread diameter). It was decided to make an interface part that could pass the M18x1,5 thread to a 14 mm hole and to use a threaded rod M14 grade 10.9 (higher grade to make the part more stiffener) as the shaft. Figure 61 is a scheme of the assembly detail where is possible to see the interface part “M18 coupling screw”.

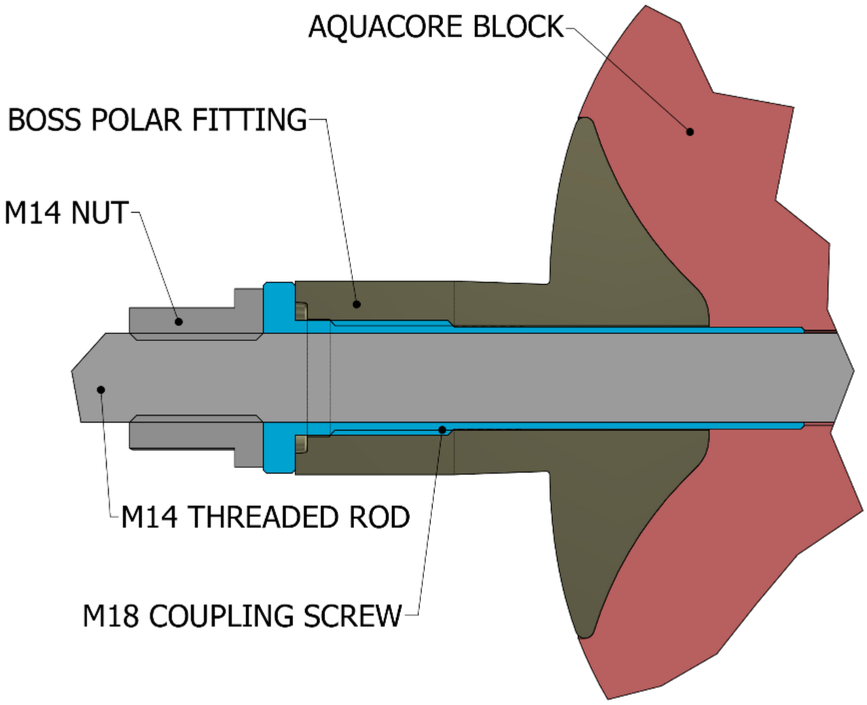

Figure 61 - Detail of the mandrel assembly.

5.1.2 Filament Winding Machine Assembly

The filament winding machine has two chucks. One transmits the torque necessary to rotate the mandrel. The other has the function of supporting the opposite end of the shaft, it has free rotation, but it can be blocked.

Because of the movement of the filament winding machine, it was decided to use two support shafts to move away the machine carriage from the chucks. These support shafts have a diameter of 50 mm and a length of 750 mm. Figure 62 is a scheme of the described setup.

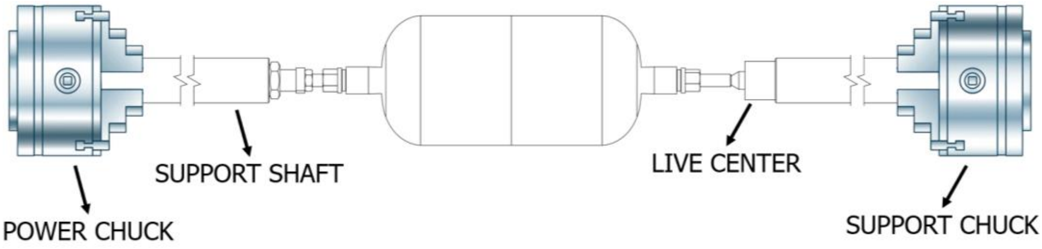

Figure 62 - Mandrel assembly in the filament winding machine.

The support shaft attached to the power chuck has an M24x2 female thread to make the interface between the support shaft and the mandrel rod. It was chosen the M24 thread so the company can have more freedom in attaching bigger mandrel shafts. To pass from M24x2 to the M14x2 thread was done an interface part. Figure 63 represents this part.

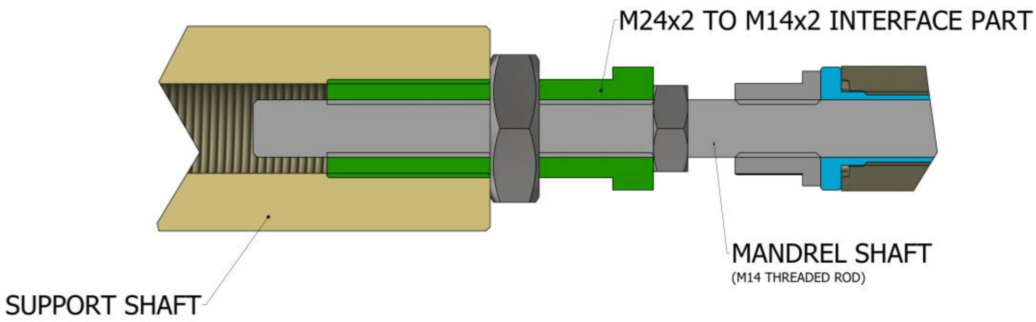

Figure 63 - Scheme in detail of the mandrel rod assembly in the support shaft.

On the other side of the assembly, it was decided to use a live center as the interface part between the mandrel and the shaft attached to the support chuck. It would be much easier if there was a direct plug to the shaft and the whole system rotate, but the problem is that the support chuck would promote unnecessary inertia forces in the M14 shaft because these two parts are heavy (support chuck and support shaft).

5.1.3 Oven Assembly

The oven is used to cure the CFRP as a system to rotate the mandrel so the epoxy can be homogeneously distributed in the overwrapped carbon fibers. Figure 64 is a photo of the oven used.

Figure 64 - Curing oven with a rotation system.

To make the mounting between the oven and the mandrel assembly, it was machined in two pieces that have an M14x2 threaded hole and a round outside surface measuring 25 mm in diameter. One of these parts is plugged directly into the oven electric motor coupling and the other part is coupled to a bearing mounted in a part that works as second support. Figure 65 presents the two parts that connect the mandrel to the oven.

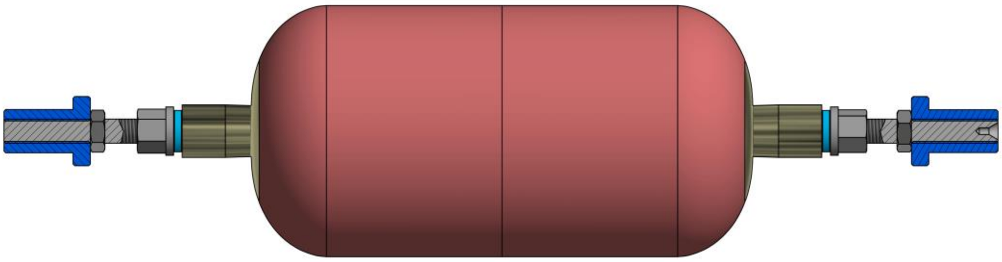

Figure 65 - Oven interface parts in the mandrel assembly.

5.2 Mandrel Production

To produce the mandrel, first, it was done some tests to get to know the Aquacore™ material and how to process it, then the mandrel production started with the ceramic block manufacturing followed by the machining step. Finally, using the Aquaseal™ and Aquafill™ products, it was done the finishing and sealing of the mandrel's surface.

5.2.1 Aquacore™ Test

This test was done to get some sensibility to the Aquacore™ material. It was used two hydraulic cylinder rectified tubes with an internal diameter of 60 mm and another with 95 mm to be the shaping mold for the specimens. In the Ø 60 mm, it was done a simple compression of cylinder blocks, Figure 66 presents a scheme of this setup.

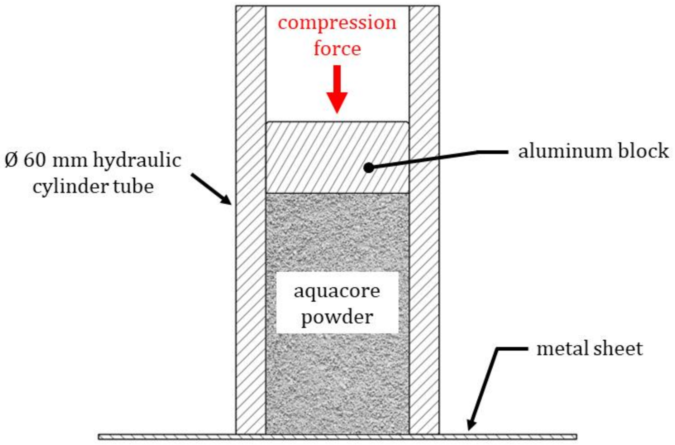

Figure 66 - Cylindrical mold compression setup.

In the Ø 95 mm, it was done a compression with a Ø 30 mm cylinder inside, the main goal of this mold setup was to understand if was possible to make a cylinder block with a hole inside. Figure 67 presents a scheme of this setup.

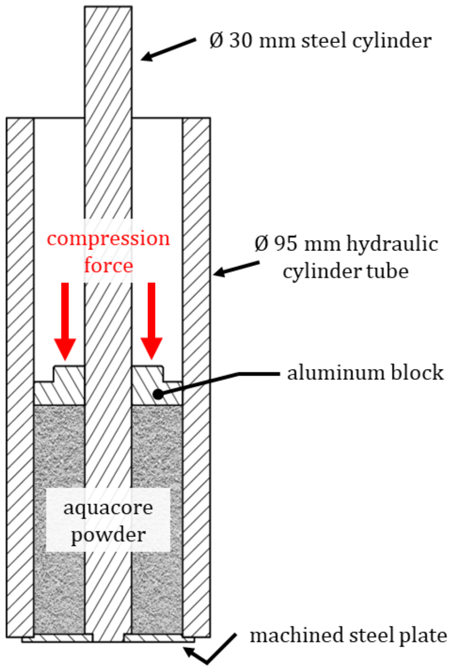

Figure 67 - Cylinder with a hole compression setup.

In the Ø 95 mm mold, it was just done compression and unmoulding of the block. This test aimed to understand if the compressed powder was able to be unmoulded without damage. First, the machined steel plate was fitted in the cylinder tube, and then it was placed in the Ø 30 mm steel cylinder. It was then filled the tube with Aquacore™ powder and finally, the aluminum block was placed in the setup. Using a pneumatic cylinder with a pressure regulator, it was done the powder compression. The pneumatic pressure was adjusted so that a pressure of 0,8 MPa was applied to the powder (a pressure slightly above that recommended by the supplier). The pressure was held for 2 minutes. The steel cylinder and the machined steel plate were carefully removed. Finally, the mold has been turned upside down, and pushing up carefully the aluminum block, the Aquacore™ cylinder was extruded with no faults.

In the Ø 60 mm setup, four different cylinder blocks were done. The aim was to understand the effect of the compression pressure on the characteristics of the Aquacore™ blocks. All the blocks were weighted to have 100 g. The compression was made using a pneumatic cylinder for specimens 2 and 3 and a hydraulic cylinder for specimen 4. After the compression, the blocks were measured and placed in an oven at 125 °C for 2 hours. To prevent thermal shock, the blocks were cooled down inside the oven. It was then cut a small part of the blocks to place in water and understand the difference in disintegration time

5.2.2 Mandrel Block Production

To produce the Aquacore™ block to be machined, a cylinder mold used to produce concrete specimen molds was utilized. The advantage of this mold is that it has an opening system that could make the extraction of the block easier. Figure 68 presents the mold used. It has an interior diameter of 150 mm and measures 300 mm in height.

Figure 68 - Concrete specimen cylinder mold used, adapted from [106].

It was machined a piece made of polyoxymethylene (POM) to make the compression. A Ø 10 mm hole in the center of the steel base plate was made and a steel rod measuring Ø 15 mm was machined and used to make the Aquacore™ block cylindrical hole. The steel base plate was covered with unmoulding tape Flashbreaker® from Airtech to avoid adhesion between the Aquacore™ block and the base plate.

Using a pneumatic cylinder with a Ø 125 mm piston, the pressure was regulated to 0,4 MPa and it was done the powder compression. A 0,4 MPa pressure in the cylinder piston is equivalent to a pressure of 0,28 MPa applied in the Aquacore™ powder, this pressure was chosen because was the maximum allowable pressure of the concrete mold. The pressure applied was limited by the mold's mechanical strength, to achieve this pressure the mold was tied up with a lashing strap in addition to the mold's fastening system. Figure 69 presents a scheme of the setup used in the compression of the Aquacore™ block.

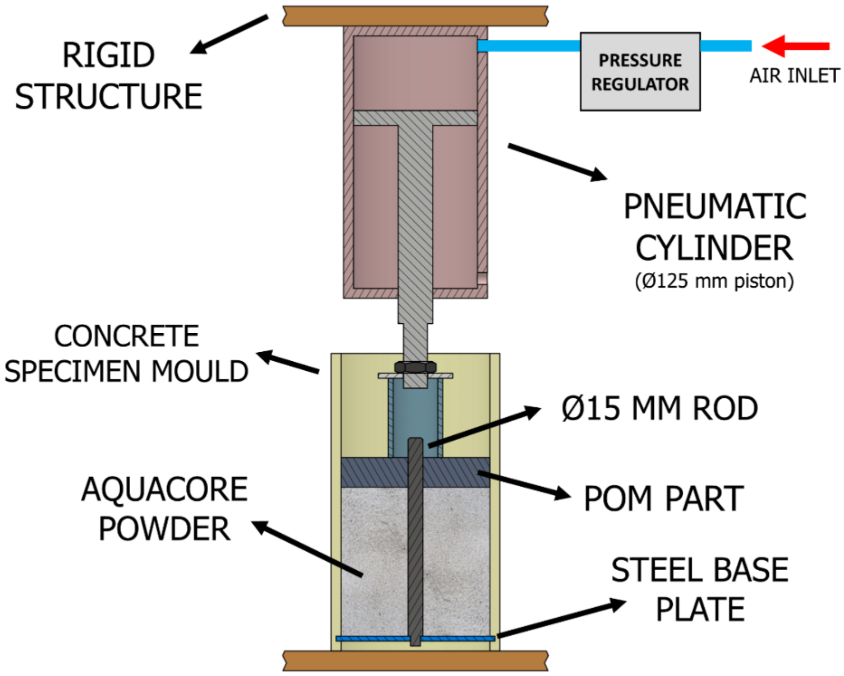

Figure 69 - Scheme of the Aquacore™ block compression step.

The quantity of Aquacore™ powder used per block was 1400 g. The inside walls of the mold were coated with Loctite® Frekote 770-NC which is a permanent release polymer. This release agent was recommended by the supplier.

After the compression of the powder with the pneumatic cylinder, the lashing strap and the Ø15 mm steel rod were removed. The mold was opened and the POM part was removed. The steel base plate with the compressed Aquacore™ powder was removed very carefully from the mold and this set was placed in the oven, where it stayed for 12 hours at 130 °C (these parameters were recommended by the supplier).

After twelve hours in the oven, the block was removed from the steel base plate and was ready to be machined.

5.2.3 Machining

The Aquacore™ blocks produced measured around 160 mm in height. Due to the high pressure of compression and the low rigidity of the plastic mold the upper cylinder end was not perpendicular to the cylindrical surface.

The first step was to use a conventional mechanical lathe to machine the cylindrical block. It was attached to the lathe using a Ø15 mm rod and an aluminum part pushed by the live center locked the part against the chuck. It was done with a facing operation so that was possible to guarantee that the machined face was perpendicular to the block center hole. This facing operation was done in just one cylinder end and it was done in the two blocks that will configure the mandrel. The lathe spindle speed was adjusted to 630 RPM.

The next step was to join the two blocks in one shaft with the machined surfaces contacting each other, the lathe fixation was the same as the one used in the previous step. The two external surfaces were turned in the same operation so it could be possible to guarantee the same external diameter in the two pieces. Figure 70 is a photo of this process. The two surfaces were machined to a diameter of 145 mm which was the desired mandrel cylindrical diameter. The longitudinal speed was adjusted to 150 mm/min and was used a maximum of 0,5 mm depth of cut.

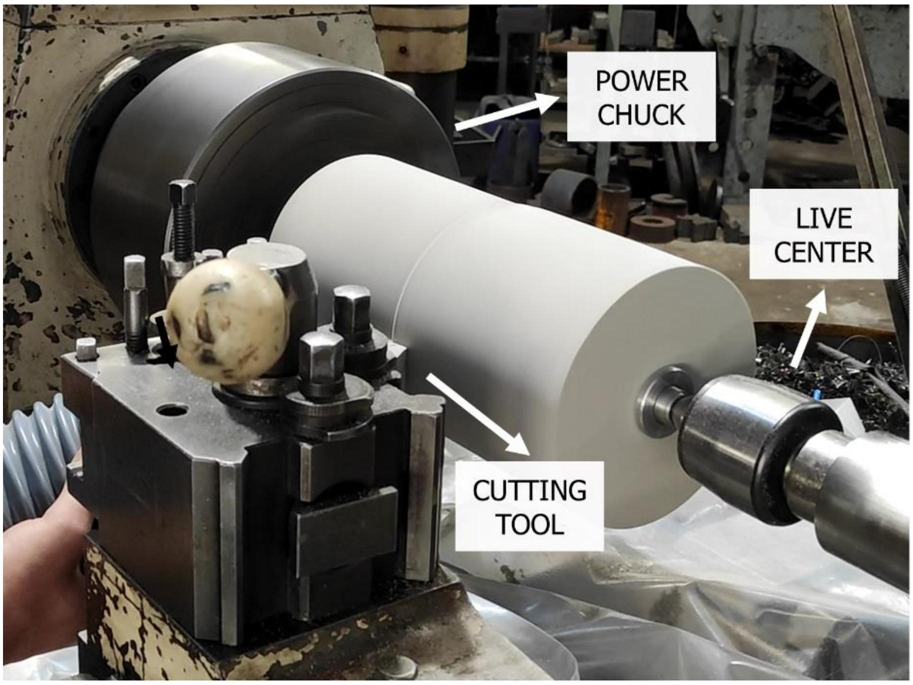

Figure 70 - Turning operation of the two blocks.

The following step was to machine the dome and the polar boss seating surface. One way to machine, it was to use a CNC milling machine with an integrated aspiration system. However, it was used other solutions. Since this Aquacore™ material was such an easy material to machine and the maximum diameter to machine was 145 mm, it was decided to create a tool to machine the material directly in a milling machine.

The tool created was a laser-cut steel sheet welded to a Ø15 mm rod. The rod was machined to fit the 3 mm thickness sheet ensuring the centricity of the sheet in relation to the rod so the part could have the correct dimensions. Figure 71 is represented a photo of the machining operation and a scheme to explain the design of the cutting tool.

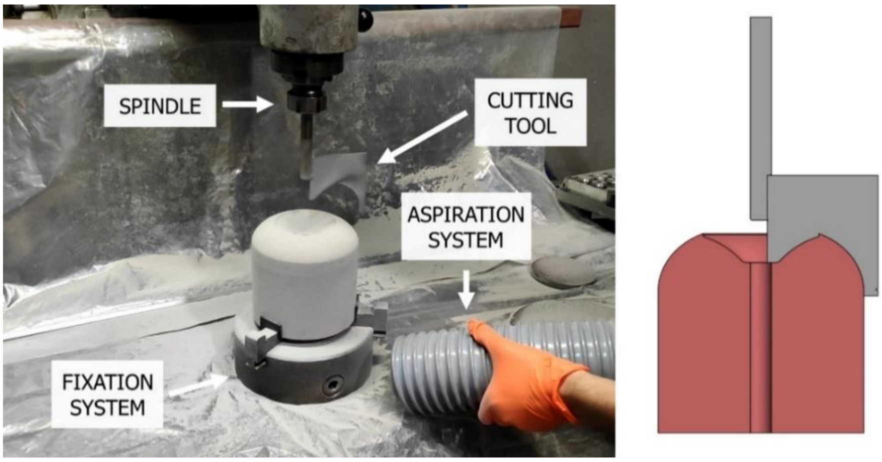

Figure 71 - Photo of the machining operation in the milling machine and a representation of the tool design.

To make this machining operation the milling machine was cleaned from any oil to avoid powder sticking and covered with plastic film. It was also used an aspiration system to avoid powder dispersed in the air. To fix the Aquacore™ block to the milling machine worktable, it was used a self-centering chuck with 3 clamps. To make a better fixation in this fragile material, a rubber sheet was placed between the clamps and the Aquacore™ block. The cylinder end that was fixed to the chuck was the lathe machined surface so it could be possible to guarantee that the block hole was perpendicular to the milling machine worktable.

To center the machine spindle with the Aquacore™ block hole, it was utilized a Ø15 mm rod and only then it was attached the cutting tool. The rotation speed of the tool was 1268 RPM. The depth of cut was controlled manually by the quill feed hand lever, so that was possible to feel the axial force that was being applied to the Aquacore™ block. The desired height was controlled by a caliper and making use of the present scales in the milling machine.

The advantage of this solution over a conventional CNC milling machine is that this solution can promote less machining time in a high-series production and besides that, it is just needed a more simple machine like a milling machine.

5.2.4 Sealing and Finishing

To avoid infiltration of the CFRP resin during the filament winding process, it was necessary to seal the surface that would have contact with the composite matrix. Due to a polar boss opening hole of 16,5 mm, it was difficult to use PTFE tape because it would complicate its removal after the mandrel washout process. It was decided to use the Aquaseal™ product.

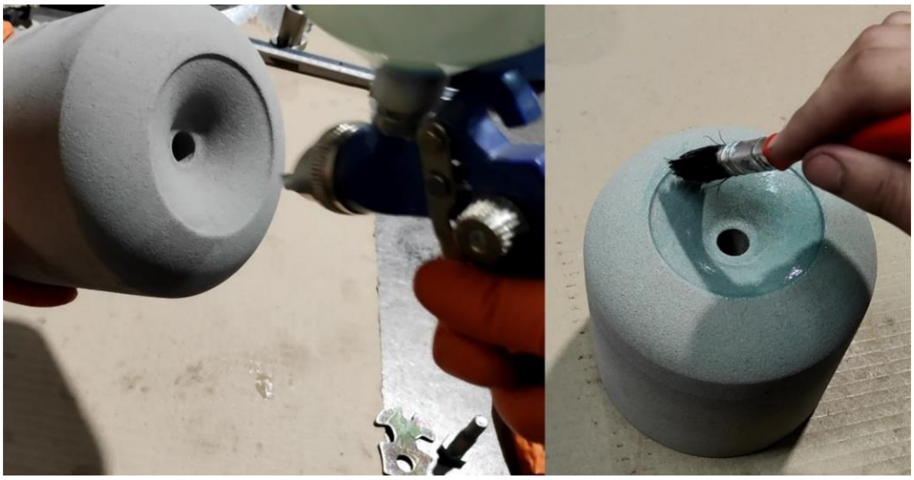

Figure 72 - Photo of the painting process; on the left the spray gun applying the first coat and on the right the application of the following coats by paint brush.

To prevent resin infiltration in the boss/mandrel interface the machined polar boss seating surface was coated with Aquaseal™ before the mandrel assembly. This sealing is applied in 4 to 6 coats and it should be dried for 20 minutes at 60 °C between coats. The first coat should be applied by a spray gun because the ceramic surface absorbs the liquid paint and starts to dissolve. If a brush was used the ceramic would be deformed. The second and next coats were applied by brush because the first paint layer gives enough sealing to avoid permeation of the following coats. Figure 72 is presented a picture of the Aquaseal™ painting steps.

The next step was to assemble all the parts that contain the mandrel and apply Aquafill™ in the gap between the two cylindrical blocks. Some defects occurred during the fixation of the block in the milling machine that was also patched. Figure 73 is a photo of the application with a metallic blade of Aquafill™ in the gap that exists between the two Aquacore™ blocks.

Figure 73 - Photo of the application of Aquafill™ to patch the gap between the two cylindrical blocks.

The Aquafill™ was left to dry overnight and then the mandrel was fixed in the lathe to machine the exterior surface and remove the excess dried Aquafill™.

Figure 74 - Application of the Aquaseal™ paint in the mandrel fixed to the cure oven.

The last step was to fix the mandrel to the cure oven and paint with Aquaseal™ the rest of the ceramic. Six coats were applied and dried at 60 °C for 20 minutes between coats. For practical reasons, all the coats were painted by brush with the first layer painted carefully. The oven rotation system was turned on when the part was drying. Figure 74 presents a picture of the application of Aquaseal™ on the mandrel surface.

5.3 Polar Boss Adhesion Tests

There was a concern in other linerless COPV development projects about the polar boss adhesion to the CRFP tank lay-up. For that reason, it was done some tests to compare the adhesion of the CRFP to stainless steel in 3 different cases. The main goal was to compare the torque necessary to rotate a M8 bolt that pushed and peeled off a CFRP hand laid up in a stainless steel sheet.

The stainless steel sheet was a square with 90 mm side and had a thickness of 2 mm. A M8 hex head nut was welded in the center of the stainless steel sheet and a hole was made so that a M8 bolt could pass the sheet to push a small piece of aluminum measuring Ø 20 mm with a thickness of 1,5 mm. This small piece pushed the CRFP lay-up peeling off from the stainless steel sheet. With a torque wrench was measured the applied binary that was necessary to peel off the CFRP lay-up. Figure 75 is a scheme of this setup.

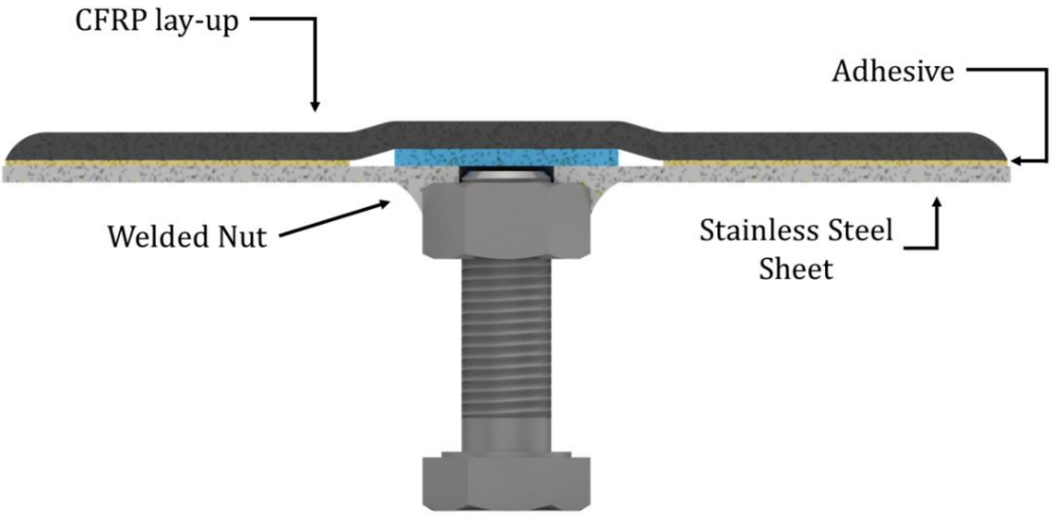

Figure 75 - Scheme of the third specimen.

The Ø 20 mm piece was covered with unmoulding tape to avoid the adhesion between this piece and the epoxy from the CFRP. The threaded hole was tapped with a small piece of tape to avoid the infiltration of epoxy on the thread. All specimens were hand laid up using six pieces of dry carbon fiber woven fabric with an epoxy matrix (Araldite® LY556 epoxy with Aradur® HY 906 hardener and the accelerator DY 070). All the sheets were degreased with propyl alcohol before the hand lay-up process. Figure 76 is a photo of the specimen production.

Figure 76 - Specimen production (hand lay-up).

The first specimen was hand laid up on top of a brushed surface sheet and the second specimen was in a grit-blasted surface sheet. The third specimen was hand laid up in a grit-blasted surface sheet with an adhesive between the CFRP and the stainless steel, the adhesive used was the Araldite® AV 138 M-1, an adhesive used to bond many different types of materials, and usually used by the company to bond CFRP to steel.

After the curing cycle, the specimens were fixed in a bench vise and with a Tohnichi DB3N4 torque wrench the screw was rotated pushing the small Ø 20 mm piece against the cured CFRP. This toque wrench has an analogic scale, to record the torque variation in the time the analogic display was filmed.

5.4 Filament Winding Process

The second-to-last step to the production of the linerless COPV was to filament wind it and cure the CFRP in the oven.

5.4.1 Filament Winding Machine and Software

The machine used to produce the linerless COPV was a MIKROSAM MAW 20 FB5/1, it is a five-axis machine specially designed for the production of optimized space structures [107]. Figure 77 presents a picture of the MIKROSAM filament winding machine.

Figure 77 - Picture of the model MAW 20 FB5/1 produced by MIKROSAM, adapted from [107].

It has its own programming software developed by MIKROSAM called Winding Expert™. It gives the possibility to import and create pressure vessel mandrels with ellipsoid, sphere, and paraboloid dome forms. Besides these forms, it gives the possibility to import a dxf file or to import an Excel file with the points that define the mandrel profile. When creating the mandrel, it is necessary to input the position length and the weight of the mandrel. The position length is the dimension that the machine needs to read the position of the mandrel in the longitudinal axis. Figure 78 is indicated what is the position length dimension, which is the length from the power chuck face to the starting point of the cylindrical part of the pressure vessel.

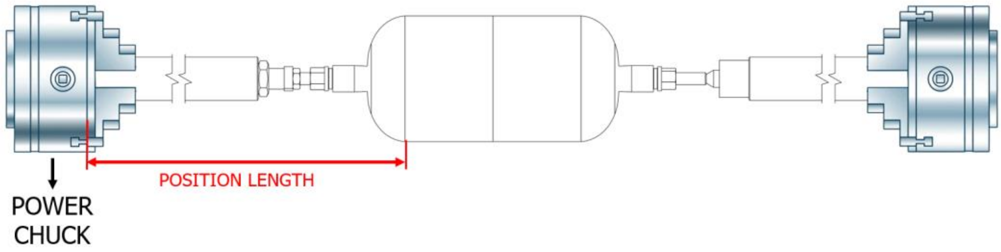

Figure 78 - Scheme of the position length dimension.

After the creation of the mandrel geometry, it is possible to make helical, hoop and transition layers around the mandrel. The mandrel geometry will update when creating and adding new layers to the filament winding program. Figure 79 presents a print screen of the software with the parameters for a helical layer in a vessel.

For a helical layer, the input parameters are the bandwidth, fiber speed, direction and opening diameter for each side. The software calculates the recommended winding angle, but this value can be changed. After the parameters are input, the software calculates a list of patterns, and for each pattern is possible to see the number of cycles that the machine will do, the covering percentage and the dwell for each side.

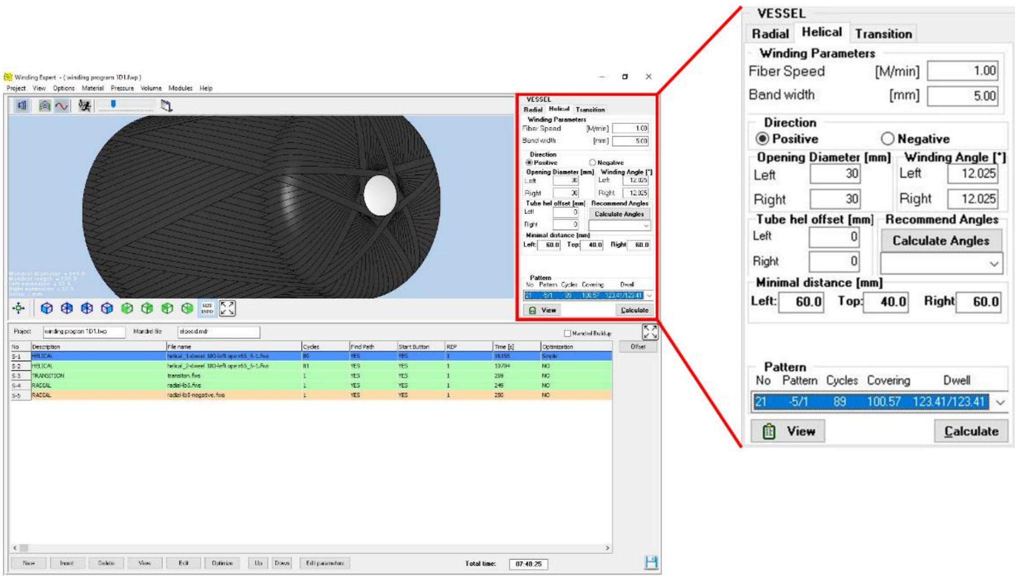

Figure 79 - Print screen of the Winding Expert™ software.

For a hoop layer, the input parameters are the bandwidth, fiber speed, number of layers, direction, and starting/ending point (if the user wants to give an offset for the cylindrical part).

To make the transition from helical to hoop layers or vice versa, it is used the transition layers, the input parameters are the bandwidth, fiber speed, starting/ending diameter, and the number of cycles (the software calculates the recommended number of cycles, but this value can be changed). These layers do not contribute to the structural performance of the COPVs.

It is possible to input the physical and mechanical properties of the fiber and resin. The software calculates a report that presents the thickness along the mandrel (this is advantageous to understand the correct height for the polar boss neck), presents an estimation of the burst pressure and estimates the material consumption for each layer (fiber length and weight, resin weight and material cost).

It also gives the possibility of exporting FEA data files to calculate and analyze filament winding products. It exports to FEA software like Abaqus, Ansys, ESAComp, Nastran, et cetera.

5.4.2 Programming and Testing

The mandrel chosen to overwrap was the one with 144 mm in diameter and 285 mm in length. The first step was to create the mandrel in the filament winding software. The dxf and Excel files with the corrected geometry were created but when importing the files to the computer program, errors appeared in different stages of the winding program. It was then decided to approach the vessel geometry with an ellipsoid dome shape that is a predefinition in the Winding Expert™ mandrels. Figure 80 is a graphic that has the calculated and ellipsoid dome geometry profiles for comparison.

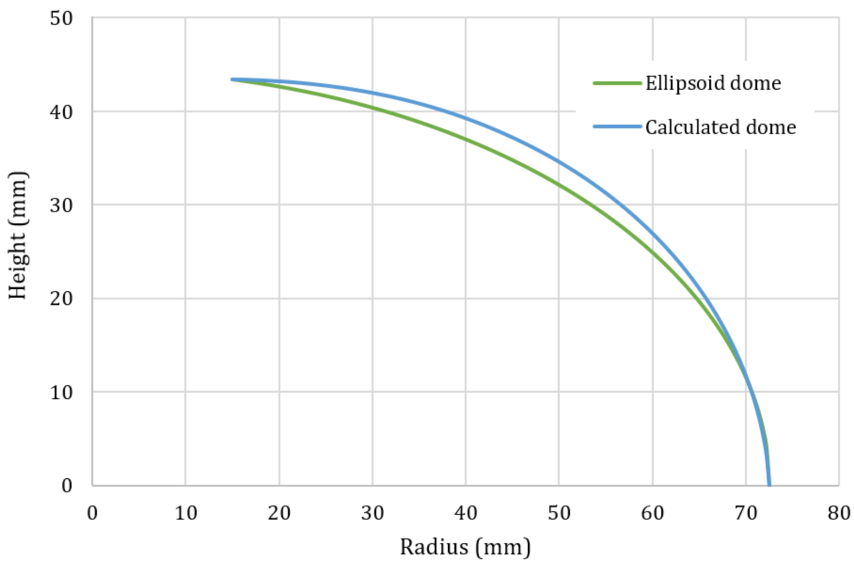

Figure 80 - Profiles of the calculated and ellipsoid dome geometry.

This was the first pressure vessel prototype made in the company so there was a lack of experience in using the filament winding machine to produce vessels and to program the winding and machine parameters. It was decided to simplify the CFRP lay-up into two helical layers and two hoop layers since this prototype was only needed to validate the production process of the linerless COPV technology. The layers used are presented in Table 17.

Table 17 - Layers used in the winding program.

Position	Layer type			
1^{st}	**Helical** Pattern -5/3	**Coverage** 100,27 %	**Cycles No.** 88	**Angle** 12,03 °
2^{nd}	**Helical** Pattern -5/1	**Coverage** 100,57 %	**Cycles No.** 89	**Angle** 12,03 °
3^{rd}	**Transition**	**Starting Diameter** 30 mm		**Ending Diameter** 144 mm
4^{th}	**Hoop**	**Direction** Positive		**Angle** 89,37 °
5^{th}	**Hoop**	**Direction** Negative		**Angle** 89,37 °

Using two carbon fiber bobbins the bandwidth was about 5 mm. The machine, winding parameters, and winding program were tuned by trial-and-error testing using dry carbon fibers before using impregnated fibers. Figure 81 is a picture of the first cycles of the helical winding process with dry fibers.

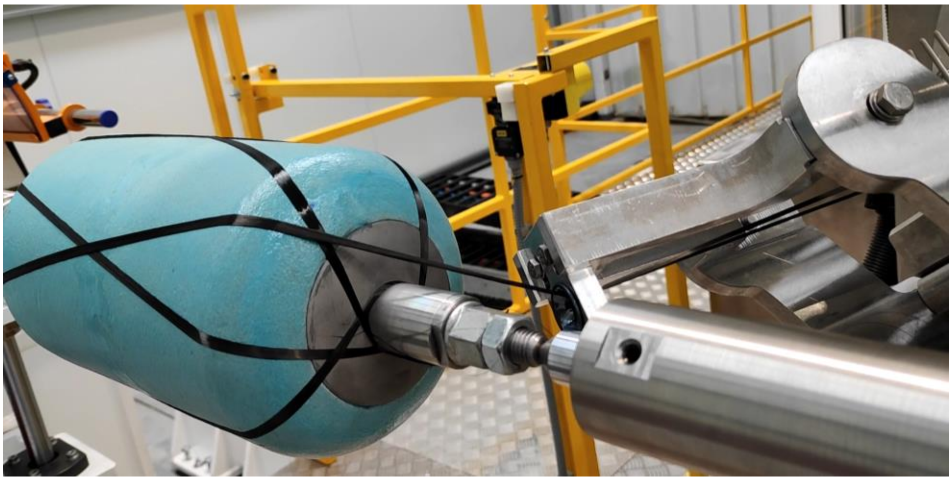

Figure 81 - Helical layer overwrap with dry fibers.

Figure 82 is a picture of the 4^{th} layer, a hoop layer, overwrapped in dry fiber where is possible to see that in the polar boss region the last cycles of the helical layers were overwrapped far away from the polar boss grit-blasted surface. It was a defect that could be fixed with the correct winding and machine parameters but because of time constraints was not possible to fix in this prototype.

Figure 82 - Hoop layer overwrap with dry fibers.

5.4.3 Mandrel Preparation

After the program testing with dry fibers, the overwrapping with impregnated carbon fibers was started. The mandrel was prepared to start the filament winding.

Three coats of Frekote 770 NC were applied in the mandrel with 5 minutes of drying time between coats for solvent evaporation.

Using isopropyl alcohol cleaner, the polar boss surfaces were degreased and Aquaseal™ paint that was accidentally painted on the metallic surface was also removed.

To make a better adhesion between the polar boss and the CFRP lay-up, the upper polar boss surfaces that have contact with the CFRP were already grit-blasted and a thin layer of Araldite® AV 138 M-1 was applied to these surfaces using a steel blade. Figure 83 is a photo of the applied adhesive on the polar boss surfaces.

Figure 83 - Mandrel with a thin layer of Araldite® AV 138 M-1 adhesive.

The threaded zones in the mandrel assembly and the support shaft interface were covered by paper tape to avoid epoxy infiltration.

5.4.4 Filament Winding and Curing Step

Right after the application of the adhesive on the polar boss surface, it was started the filament winding with the impregnated carbon fiber. The two components (epoxy and hardener) Olin LITESTONE® were already prepared and placed in the resin bath heated at 30 °C. Figure 84 is a picture of the machine impregnation system.

Figure 84 - Picture of the machine impregnation system.

The winding was started, and the bandwidth was confirmed to see if was necessary to update the winding program, it measured around 6,50 mm because of the fiber impregnation. Despite the winding program having a bandwidth of 5 mm, this difference was ignored, it could give an unnecessary overlapping, but this was not taken into consideration for the first prototype.

It was brushed epoxy matrix on the mandrel during the first cycles simulating the application of the permeation coating described in section 4.5.

The machine pay-out eye used that is not recommended for vessel winding production caused some fraying in the carbon fibers.

During the filament winding process, there was some fiber slippage in some cycles, to reverse this defect the fiber was forced to the mandrel with a finger in the slipping areas. This winding defect could be justified by a weak tuning of the winding and machine parameters in the winding program.

In the end before the hoop layers, occurred slippage in the transition layer made it useless. The winding of hoop layers had good behavior, except in the extremities where occurred fiber slippage to the dome area.

When the filament winding process finished, it was used shrink tape overlapped in the cylindrical part of the vessel, to give a good finish in this region and to consolidate the CFRP. Two heaters were placed in the bottom of the tank and the mandrel was left rotating for one hour. The temperature was controlled by a thermometer and was around 70 °C, the main goal was to achieve the gel time of the resin because the curing oven was in another facility and was needed to transport the pressure vessel for some time. Figure 85 is a picture of the shrink tape application in the filament wound mandrel and where is possible to see the heaters.

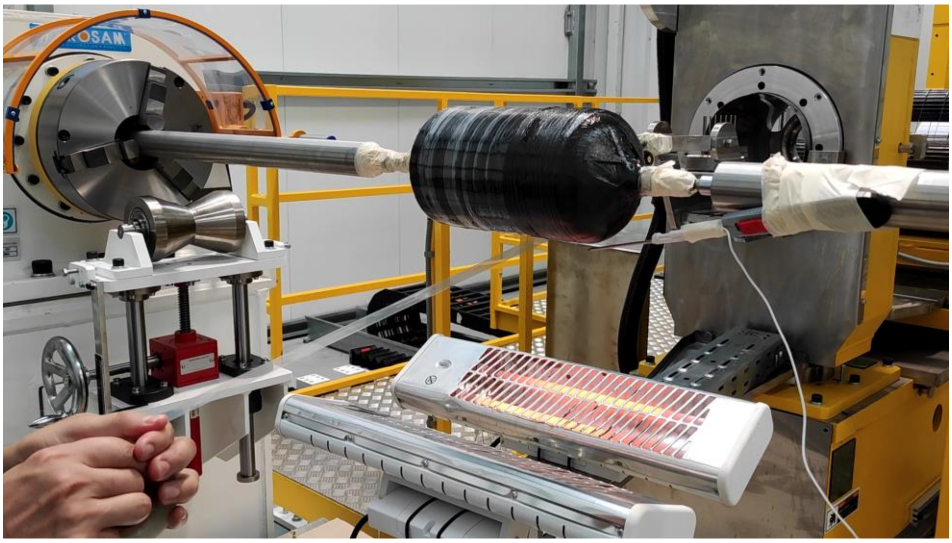

Figure 85 - Picture of the shrink tape application.

The final step was to remove the mandrel assembly from the filament winding machine, assemble the oven interface parts and attach the mandrel assembly to the oven.

With the oven rotation system turned on, the pressure was left to cure for one hour at 90 °C and then four hours at 110 °C. This curing cycle is recommended by the Olin Corporation for a type IV pressure vessel (there was no information about type V pressure vessels). Figure 86 is a picture of the curing process.

Figure 86 - Pressure vessel at the curing stage in the oven.

5.4.5 Mandrel Washout

When the cured pressure vessel and mandrel cooled down from the curing step, the shrink tape was easily removed and the ceramic washed out. Warm water was used because facilitates the ceramic and Aquaseal™ removal. The washout lasted about one hour but at the end, using a light, the interior was inspected and all Aquaseal™ and ceramic were removed. There was some ceramic that was bonded to some Araldite® adhesive that penetrated the outskirt of the polar boss part but can be considered residual. Figure

87 is a picture of the washout process where it is possible to see pieces of Aquaseal™ and Aquacore™ ceramic that were washed from the vessel.

Figure 87 - Aquacore™ and Aquaseal™ washout.

Chapter 6

Results and Discussion

This section presents results from the Aquacore™ material and adhesion experiments for the polar boss/CFRP interface. The mandrel fabrication defects are referred, and the proposed methods to avoid these defects are presented. Finally, is presented a discussion of the prototype characteristics and proposed solutions to improve the efficiency of the pressure vessel.

6.1 Soluble Mandrel

Regarding the first Aquacore™ tests, they were made to understand the solid ceramic block quality in relation to the compression pressure applied in the production step. After the oven step, the blocks were weighted and measured. A resume of the results is presented in Table 18 and Table 19.

Table 18 - Characteristics of the cylinder blocks before the oven step.

Specimen	**Compression pressure** MPa	**Weight** g	**Height** mm	**Diameter** mm
1	compressed by hand	100	67	60
2	0,83		64	
3	1,67		59	
4	3,53		51	

Table 19 - Characteristics of the cylinder blocks after the oven step.

Specimen	**Weight** g	**Density** g/cm^3	**Height** mm	**Diameter** mm
1	86,8	0,46	67	60
2	85,8	0,47	64	
3	84,9	0,51	59	
4	86,5	0,60	51	

It was concluded that there was no volume reduction in the oven step, the samples had the same dimensions before and after this step. The loss of mass is explained by the water evaporation that occurs in the powder.

Comparing the density values with the manufacturer data (the aqua block has a density of 0,46 g/cm^3), specimen 1 which was compressed by hand had the same density as the supplier aqua blocks.

When the specimen 1 and 4 samples were placed in water, it was visible that sample number 1 was much faster to disintegrate itself than the fourth sample. This can be an important factor when accounting for the mandrel washout time.

The compression pressure was already an important factor when unmoulding the Aquacore™ compressed powder from the Ø 150 mm mold. With higher compression, the risk of the compressed block having defects was minimized.

In the machining step, it was understood that higher compression pressure in the block production would produce better surface quality. Figure 88 is a picture of the dome customized tool machined surface where is visible the great finishing that the surface has.

Figure 88 - Photo of the machined dome and polar boss seating surface.

To conclude this topic, about the compression applied in the Aquacore™ block production, it was understood that any pressure would make a solid block that could serve as a mandrel base material. Although lower compression increases the risk of the compressed powder block having defects. It is recommended to use higher compression to have a greater block quality to detriment of ceramic washing time and powder spent material.

After the Aquaseal™ paint step, the mandrel was ready to be overwrapped in but to have a better understanding of its final geometry, length and diameter dimensions were checked using a large caliper, Figure 89 represents the measuring procedure.

Figure 89 - Mandrel length measure procedure.

Two mandrels were produced, one of them had a diameter of 144 mm and 285 mm in length, and the other had a diameter of 146 mm and 287 mm in length. The aim was to achieve a diameter of 145 mm and 290 mm in length. Besides these differences in dimensions from those projected, the mandrels presented some defects in the surface that could have been corrected if the machining step was made differently.

In the lathe machining step, the exterior surface should not have been machined to 145 mm but a slightly bigger diameter (like 146,50 mm). The justification for this is that if a bigger diameter was chosen in this step, it was easier to have a better surface after the Aquafill™ patch. Every defect that the blocks could have in the cylindrical part would have been filled by Aquafill™ and machined with a higher depth, achieving the desired diameter.

It was not accounted for the Aquaseal™ thickness, and it was something that should be taken into account if is desired a perfect diameter dimension. This compensation should have been given in the dome and polar boss seating surface machining tool too. Although, the thickness of the Aquaseal™ is something difficult to control when manually painting the ceramic.

The length did not achieve the desired dimension because in the Aquaseal™ painting step, during the painting of the several coats the ceramic became ductile in the dome area (probably because of the infiltration of liquid in the ceramic porosities) and that has loosen the hex M14 nuts. When tightening the set, the polar boss penetrates a few millimeters in the dome area and that explains the fact of having lengths shorter than 290 mm. When the ceramic cooled down after the last coat application the mandrel became hard again. It should have been used locknuts instead of normal M14 nuts or two nuts on each side tightened one against the other to avoid loosening.

6.2 Polar Boss Adhesion Tests

Watching the recorded videos of the torque analogic display made it possible to understand the torque range values that have dominated in the CFRP peeling-off step. These test results are presented in Table 20.

Table 20 - Adhesion test results.

Specimen Number	**Description**	**Maximum Torque Exerted** Nm
1	brushed sheet with CFRP	8 - 9,5
2	grit-blasted sheet with CFRP	4 - 4,5
3	grit-blasted sheet with adhesive and CFRP	11,5 - 12,5

The torque applied when peeling off the CFRP from the stainless steel showed that there was adhesion in all specimens between the two materials. Figure 90 presents a photo of the specimens after the peeling-off step.

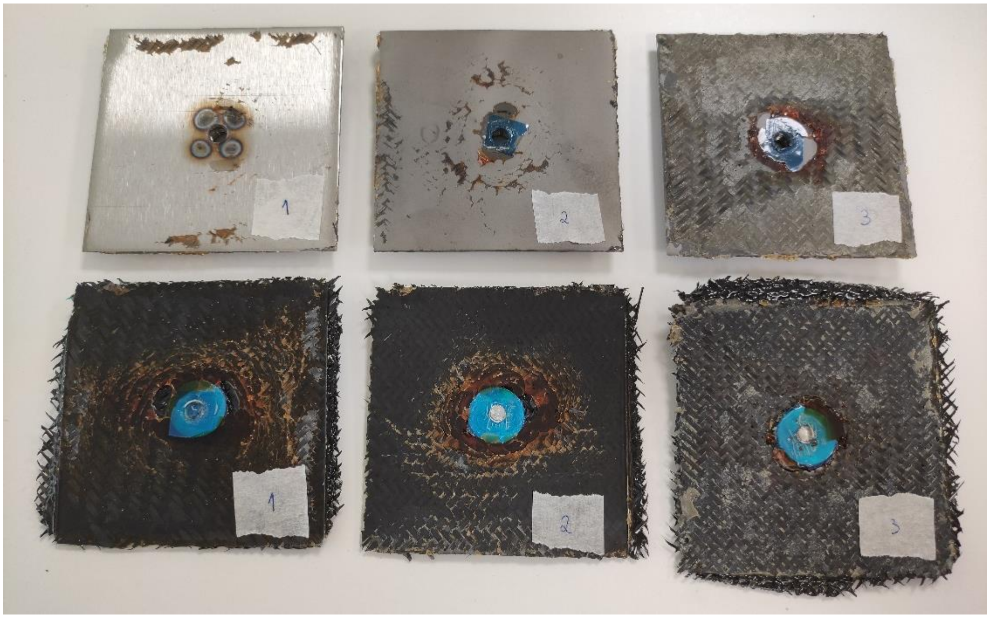

Figure 90 - Picture of the specimens after the peeling-off step.

The Araldite® adhesive had a positive result assisting the bonding of the CFRP to the grit-blasted stainless-steel sheet. Comparing specimen 1 with specimen 2 it was concluded that the brushed finishing had a good result having a maximum torque value next to specimen 3. Specimen 2 had an unexpected result because it was predictable that a grit-blasted surface could have better adhesion properties than a brushed surface. This difference could be explained by any type of grease that did not have been removed from the sheet or by any type of stress in the adhesive bond promoted by a cutting process that has taken place to remove the excess of cured CFRP in the sheet borders. This test should have been repeated to understand if it was a sample defect or if effectively the adhesion of the CFRP with a grit-blasted surface is weaker than a brushed surface.

It should have been done another test with the Araldite® adhesive on a brushed sheet to compare it with the other results.

It is known that the brushed surface treatment is not the same as a finished machined surface, but it was possible to apply the brushing finish to the polar boss surface if needed.

6.3 Linerless COPV Prototype

The first linerless and COPV prototype built in the FHP company is presented in Figure 91. It weighed 1,8 kg, the winding simulation software calculated a total weight of 0,46 kg for the composite, and the two polar bosses weighed 1,22 kg, the Araldite® adhesive is a thin layer that can be ignored (it weighs less than 0,01 kg). The total tank weight supposedly should be 1,68 kg following the filament winding simulation program calculus, giving a difference of 0,12 kg from the produced one. This difference can be explained by the extra resin that the tank has accumulated during the filament winding process.

Figure 91 - First linerless COPV prototype produced in the FHP company.

The winding defects are noted in the picture presented above. The incorrect winding and machine parameters have rolled up the fibers in the wrong position of the mandrel. These defects were already noted when testing the overwrapping with dry fibers as described in section 5.4.2. It is also noted the fiber slipping from the hoop layers to the dome area, was something that could be corrected if the hoop layer had an offset not too close to the cylindrical part edges.

To understand the final design and characteristics of the pressure vessel, it was compared with the linerless COPVs produced by the Infinite Composites company. It was assumed a burst pressure of 25,2 MPa calculated by the Winding Expert™ software. Table 21 presents the comparison between the produced tank with the Infinite Composite linerless COPVs.

Table 21 - Comparison between the linerless prototype and the Infinite Composites products [108].

Diameter mm	**Length** mm	**MEOP** MPa	**Minimum burst pressure** MPa	**Volume** L	**Weight** kg	**Category**	**Efficiency** x10^{-4} m
65,6	88,5	3,4	6,9	0,12	0,11	Cryogenic	0,75
144	**285**	**-**	**25,2**	**4,3**	**1,8**	-	**6,02**
151,1	1209,5	6,9	10,3	18,9	3,18	Low-Pressure	6,15
607	645	3,4	6,9	110,01	10,91	Cryogenic	6,95
268	531	1,0	4,1	27,27	1,15	Low-Pressure	9,81
276,9	2229,6	6,9	20,7	112,91	19,55	Cryogenic	11,95
151	144	30,0	45,0	1,4	0,5	High-Pressure	12,60
650,2	946,4	3,4	13,8	256	26,36	Cryogenic	13,39
338	340	34,5	51,7	22,2	4,8	High-Pressure	23,92
281,6	975,4	27,6	82,7	43	14,1	High-Pressure	25,23
586,7	1524	31,0	69,8	327	84,1	High-Pressure	27,14
508	1564,6	37,9	75,8	236,1	61,4	High-Pressure	29,16

It is quite clear that the developed tank has a low efficiency when compared with already finished and ready-to-sell Infinite Composite products. One of the main reasons is in the polar boss fittings. These parts represent more than 66 % of the total tank weight. It means that the criteria used to select the most promising part could have not been the right one.

Autofrettage is a metal forming technique that is commonly used to reinforce thick-walled cylindrical and spherical pressure vessels. The technique is based on the premise of first submitting the cylindrical or spherical vessel to partial plastic deformation and then unloading it, resulting in the creation of compressive residual stresses [109]. This is something that can be considered in the design of the polar boss part, if it is assumed that the part will have partially plasticized in the first pressurized cycle, the part could be less robust, and consequently lighter, as demonstrated in section 4.4.3.

The simulation done to develop the geometry of the polar boss part should have been done with the complete stress-strain curve for the AISI 304 stainless steel. Unfortunately, it was not found in the literature on the stress/strain points to input the plastic characteristics of this metal. Although to find the relation of the stress/strain curves, it could have been searched for classical equations parameters like Hollomon, Ludwigson, or Swift law, for example [110].

Another solution to reduce the weight of the polar boss parts was to change the material for others with higher specific resistance. Although higher CTE, as explained in section 4.4.1, aluminum alloys could be a potential substitute for the polar boss material.

Aluminum 7075 is a very high-strength material used in highly stressed structural parts such as aircraft fittings, gears, shafts, fuse parts, worm gears, aircraft, aerospace, and defense applications. It has a yield strength of around 500 MPa, the elastic modulus is 71,7 GPa and the Poisson's ratio is 0,33 [111]. Using the CAD software, it was calculated weight of 0,215 kg if the developed polar boss was made in this aluminum alloy. To understand the behavior of this part, it was used the same simulation was done to develop the other polar boss part and the material was changed for this aluminum alloy, Figure 92 presents the simulation stress results.

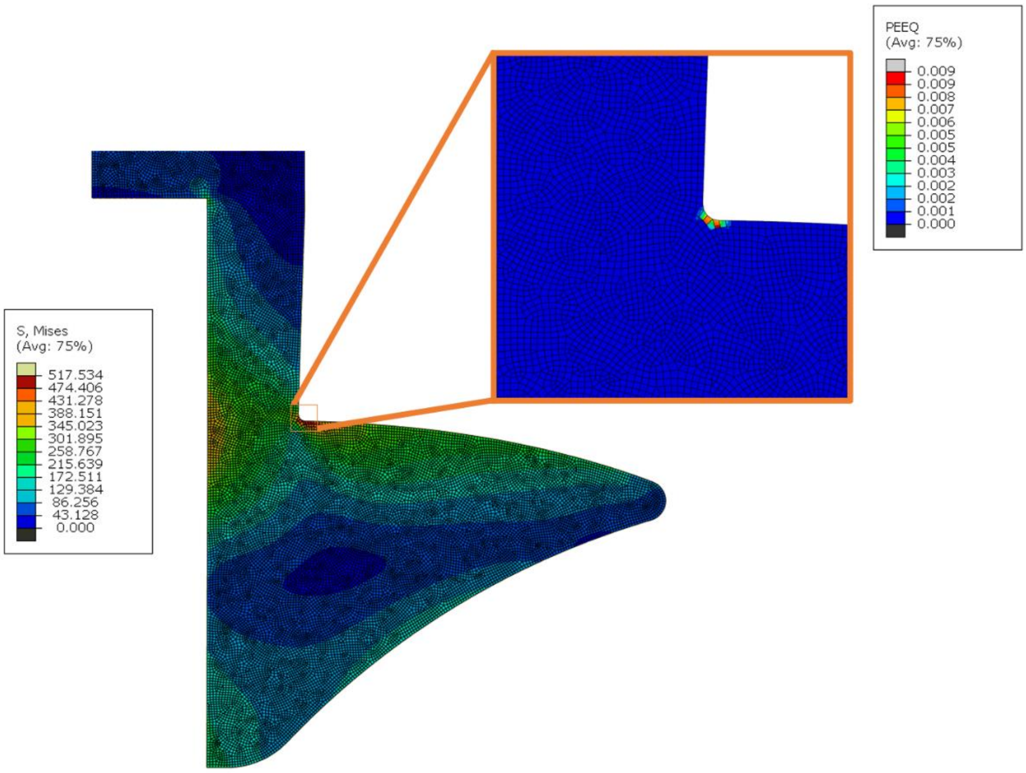

Figure 92 - Simulation of the polar boss stress with the aluminum 7075 alloy.

Using the swift law with the parameters presented by Li et al. the plastic stress/strain values were inputted into the model [112]. It is visible that only a very small region had plasticized. It was made pressurization until 60 MPa and depressurized after. The equivalent plastic strain (PEEQ) had a maximum of 0,009 in the maximum stress point presented in Figure 92. The deformation of the part was nearly zero and did not compromitted the CFRP polar boss interface.

If the produced tank had these aluminum parts, it would weigh 1,03 kg and the efficiency would jump from 6,02 to 10,52. Analyzing the CTE from the AISI 304 stainless steel to the aluminum 7075 alloy is a difference from 17,3 µm/mK to 23,4 µm/mK [101, 111]. It is important to study if this CTE difference could be a problem in the curing stage or in a space application where the pressure vessel is subjected to a high-temperature range.

It is also necessary to consider the adhesion between the CFRP (or Araldite® adhesive) and this aluminum alloy.

Chapter 7

Conclusions and Future Work

7.1 Conclusions

From what was presented in this document, it is clear the potential that the linerless COPV's technology has in this promising future of space exploration. Cryogenic storage is something that has great potential for an all-composite pressure vessel although other successful projects use linerless technologies to store other propellants. It is expected that the usage of this type V COPV technology continues to rise, especially in applications where weight savings are a priority.

The main goal of this work was to overcome the challenge of filament winding a pressure vessel with no liner to overwrap the fibers in. This problem was solved through the use of washable products. Another possible route to have washable mandrels with different geometries was to order a 3D printed mandrel directly from the ExOne company, however, since this printing option is only available in the United States, lead time and logistical problems could be a handicap factor.

The knowledge that has been acquired with the usage of washable ceramic materials will allow FHP company to produce different types of tank geometries inexpensively. The Aquacore™ block can be fabricated in any size and the machining process is easy to do. If machining with a customized tool (methodology used in this work) could not be applied, because of size constraints, the block could be machined using a 3-axis CNC milling machine.

Since mandrel fabrication is an easy and cheap process, FHP has the freedom now to test any type of geometry. This is important because gives the company the possibility to rapidly create and test different mandrel geometries, without design constraints and look up for better characteristics of the tank performance.

Using Abaqus WCM to simulate the polar boss stress was a potential route to the future development of new geometries. Although, the criteria used to accept or reject the tests done in each iteration were overly conservative, resulting in a heavy piece. These simulations should have been done with the plastic properties of the material used. Cycles of pressurization (until burst pressure) and depressurization should have been done to understand if the part would plastically deform to the extent of creating a big gap between the polar boss/CFRP interface or not. Besides that, cohesive elements should have been used with the properties of the Araldite® AV 138 M-1 instead of using surface contact with a high friction coefficient.

With the linerless COPV production technology validated, the focus should be now to solve the permeation problem that these tanks would have. Graphene nanoparticles are the most promising materials for creating a tortuous path inside the thermoset. A methodology to apply these particles was presented, although it is known that only these particles type would be not sufficient to have a fully functional permeation barrier. Other companies, such as Infinite Composites, have already admitted to using nanoparticle reinforcements other than graphene-based ones. The involved strain in the composite shell is also something to study because is directly related to the microcracking issue that causes higher permeation rates.

7.2 Future Work

The fabrication of the linerless COPV prototype was the first step in the development of these products. There is still much to do to obtain a promising and secure product. Since the production methodology was already validated, future development should focus on structural and weight optimization, and solve the permeation problem.

Firstly, it is important to modify the polar boss part because of its large weight. It could be searched for other lighter materials besides the aluminum alloy suggested in section 6.3. Although, Infinite Composites has already a long experience in linerless COPVs, continues to use the AISI 304 stainless steel to produce these parts. So, the most promising methodology is to change this part design to make it lighter, as explained in the previous section.

After having a lighter polar boss part, it is then possible to have a tank that could compete in efficiency with the other tank types. The second challenge is to solve the permeation problem. Firstly, it is recommended to search for other important nano reinforcements particles that could be added to the resin matrix besides the graphene-based particles, as explained in section 4.5. Then, it is suggested to work with the Applied Graphene Company that would additive the epoxy resin. It can be produced in a series of small tanks with the suggested permeation barrier route presented in section 4.5. These tanks could be submitted to simple permeation tests. The most important variables that would be interesting to test are:

- quantity of graphene dispersed;
- lay-ups configurations (for each lay-up a different strain field, that would cause different microcracking densities);
- number of fatigue cycles of pressurization/depressurization.

Because of its small molecule size, helium gas is a typical gas utilized in permeation tests. These tests could be, for example, filling the tanks at the same pressure and analyzing their weight reduction over time. This methodology is proposed by the international standard ISO 11119-3-2013 [113]. Being small tanks, another setup that could be done is to have the tanks pressurized in a closed chamber with vacuum applied inside. The two pressures (inside the chamber and inside the tank) would be recorded for a period of time. Having this data is possible to calculate the quantity of gas that has passed from the COPV to the chamber and to calculate the permeation rate. Instead of pressure recording, a helium mass spectrometer could be used in the vacuum chamber. Mallick et al. have utilized this technique to measure the permeation of their linerless tanks [14].

It was critical to do additional studies to determine the influence of dome profile geometry on tank performance. To test it, different dome geometries in equal length and diameter tanks could be simulated utilizing the full capabilities of Abaqus WCM or any other FEA analysis software. A second technique was to make pressure vessels with these various dome geometries (for example, using the Abaqus WCM generated geodesic profile and the theoretical profile developed in this work). These tanks would be burst tested to see what type of failure the tank would present and which one would have the highest burst pressure. Cho et al. have researched three different dome profiles in type IV pressure vessels using the methodology explained above [111].

A study should be done to understand if the Araldite® AV 138 M-1 adhesive has an influence on the stress of the pressurized CFRP, in the dome region, and if there is a rupture of the adhesive joint in fatigue cycles of pressurization/depressurization. This study, firstly, should be done using FEA analyses software, with the cohesive characteristics of the adhesive joint to understand the CFRP resultant stress in that region. After the FEA analyses, make a test with a linerless prototype subjected to fatigue cycles of pressurization/depressurization to analyze if there is a rupture of the glued joint.

Lastly, it is suggested that the company should develop an internal burst test setup. It is essential to have internal tools to test produced tanks, in an early stage of development like this and in the future to control the quality of the produced COPVs. It is also important to validate lay-up configurations, test different domes profile geometries (as explained in the previous section), and make fatigue cycles of pressurization/depressurization for the permeation tests.

References

[1] P. Gąsior, R. Rybczyński, J. Kaleta, S. Villalonga, F. Nony, and C. Magnier, "High Pressure Composite Vessel With Integrated Optical Fiber Sensors: Monitoring of Manufacturing Process and Operation," in *Pressure Vessels and Piping Conference*, 2018, vol. 51661: American Society of Mechanical Engineers, p. V005T05A013.

[2] Cannae. "Space Freighter." http://cannae.com/space-freighter/ (accessed Aug. 08, 2022).

[3] A. Technology. "Astrobotic Lunar Landers - Payload User's Guide." https://www.astrobotic.com/wp-content/uploads/2022/01/PUGLanders_011222.pdf (accessed Sep. 05, 2022).

[4] S. Clark. "Mars rover ready for riskiest part of $2.7 billion mission." https://spaceflightnow.com/2021/02/17/mars-rover-ready-for-riskiest-part-of-2-7-billion-mission/ (accessed Sep. 15, 2022).

[5] G. S. G. I. Research, "Profiles in Innovation: Space – The Next Investment Frontier," 2017. [Online]. Available: https://www.gspublishing.com/content/research/en/reports/2017/04/04/49ead899-a05b-4822-9645-2948f2050a31.pdf

[6] S. Ventures. "Infinite Composites, Inc." https://www.spacedventures.com/offers/infinite-composites-inc/pitch (accessed Sep. 10, 2022).

[7] D. M. Grogan, "Damage and permeability in linerless composite cryogenic tanks," Ph.D. dissertation, National University of Ireland, Galway, Ireland, 2015.

[8] H. Mason. "Developing a linerless, all-composite, spherical cryotank." https://www.compositesworld.com/articles/developing-a-linerless-all-composite-spherical-cryotank (accessed Jun. 14, 2022).

[9] B. Jones and M.-C. Li, "Liner-less Tanks for Space Application - Design and Manufacturing Considerations," in *5th Conference on Aerospace Materials, Processes, and Environmental Technology*, Marshall Space Flight Center, Alabama, Nov. 2003. [Online]. Available: https://ntrs.nasa.gov/citations/20040084010

[10] G. Gardiner. "Composites end markets: Pressure vessels (2022)." https://www.compositesworld.com/articles/the-markets-pressure-vessels-2022 (accessed Aug. 23, 2022).

[11] A. S. Technologies. "Composite Overwrapped Pressure Vessels (COPV) [Ultimate Guide]." https://astforgetech.com/composite-overwrapped-pressure-vessels-copv-ultimate-guide/#What_are_Composite_Overwrapped_Pressure_Vessels_COPV (accessed Aug. 25, 2022).

[12] I. Composites. "About Tank Types." https://www.infinitecomposites.com/composite-pressure-vessel-resources (accessed Aug. 26, 2022).

[13] P. J. P. Berro Ramirez, D. Halm, J.-C. Grandidier, S. Villalonga, and F. Nony, "700 bar type IV high pressure hydrogen storage vessel burst – Simulation and experimental validation," *International Journal of Hydrogen Energy*, vol. 40, Jul. 2015, doi: 10.1016/j.ijhydene.2015.05.126.

[14] K. Mallick, J. Cronin, P. Fabian, and M. Tupper, "Microcrack Resistant Polymers Enabling Lightweight Composite Hydrogen Storage Vessels," *Materials Challenges in Alternative and Renewable Energy*, p. 91, Dec. 2011, doi: 10.1002/9781118019467.ch9.

[15] C. Red. "Pressure vessels for alternative fuels, 2014-2023." https://www.compositesworld.com/articles/pressure-vessels-for-alternative-fuels-2014-2023 (accessed Aug. 25, 2022).

[16] S. T. Peters, *Composite Filament Winding*. ASM International, 2011. [Online]. Available: https://books.google.pt/books?id=nciMwbQfymQC

[17] K. Mallick *et al.*, "Ultralight linerless composite tanks for in-space applications," in *Space 2004 Conference and Exhibit*, doi: 10.2514/6.2004-5801.

[18] S. Alam, G. R. Yandek, R. C. Lee, and J. M. Mabry, "Design and development of a filament wound composite overwrapped pressure vessel," *Composites Part C: Open Access*, vol. 2, p. 100045, Oct. 2020, doi: 10.1016/j.jcomc.2020.100045.

[19] M. Azeem *et al.*, "Application of Filament Winding Technology in Composite Pressure Vessels and Challenges: A Review," *Journal of Energy Storage*, vol. 49, p. 103468, May. 2022, doi: 10.1016/j.est.2021.103468.

[20] T. C. M. A. Inc. "Carbon Fiber." https://www.toraycma.com/products/carbon-fiber/#pattern4_1 (accessed May 05, 2022).

[21] H. Corporation. "HexTow® " https://www.hexcel.com/user_area/content_media/raw/HexTowSelectorGuide.pdf (accessed May. 05, 2022).

[22] X. Wang *et al.*, "Evaluation of embedded buckypaper sensors in composite overwrappedped pressure vessels for progressive damage monitoring," *Composite Structures*, vol. 284, p. 115223, Mar. 2022, doi: 10.1016/j.compstruct.2022.115223.

[23] L. ZU, "Design and optimization of filament wound composite pressure vessels," Ph.D. dissertation, Delft University of Technology, 2012. [Online]. Available: http://resolver.tudelft.nl/uuid:3392af2c-9ff5-4ccf-af2d-7829b95701cb

[24] S. K. Mazumdar and K. C. Manufacturing, *Materials, product, and process engineering* (Plast. Eng). 2002.

[25] A. Anvari, "Thermomechanical Fatigue of Unidirectional Carbon Fiber/Epoxy Composite in Space," *Journal of Engineering*, vol. 2020, p. 9702957, Jun. 2020, doi: 10.1155/2020/9702957.

[26] G. T. P. Ltd. "Filament Winding." https://www.grptubing.com/images/filament_3.jpg (accessed Sep. 14, 2022).

[27] R. d. L. A. Furtado, "Filament Winding Simulation," FEUP, UP, Porto, Portugal, 2016. [Online]. Available: https://repositorio-aberto.up.pt/bitstream/10216/83321/2/125942.pdf

[28] I. H. Dalibor, T. V. Lisbôa, R. J. Marczak, and S. C. Amico, "A geometric approach for filament winding pattern generation and study of the influence of the slippage coefficient," *Journal of the Brazilian Society of Mechanical Sciences and Engineering*, vol. 41, no. 12, p. 576, Nov. 2019, doi: 10.1007/s40430-019-2083-2. [Online]. Available: https://doi.org/10.1007/s40430-019-2083-2

[29] J. Scholliers and H. Van Brussel, "Computer-integrated filament winding: computer-integrated design, robotic filament winding and robotic quality control," *Composites Manufacturing*, vol. 5, no. 1, pp. 15-23, Mar. 1994, doi: 10.1016/0956-7143(94)90015-9.

[30] M. Quanjin, M. R. M. Rejab, J. Kaige, M. S. Idris, and M. N. Harith, "Filament winding technique, experiment and simulation analysis on tubular structure," *IOP Conference Series: Materials Science and Engineering*, vol. 342, no. 1, p. 012029, Apr. 2018, doi: 10.1088/1757-899x/342/1/012029.

[31] M. Urbaniak and K. Grudziński, "Time-temperature-transformation (TTT) cure diagram for EPY® epoxy system," *Polimery*, vol. 52, no. 2, pp. 117-126, Feb. 2007, doi: 10.14314/polimery.2007.117. Accessed: 2022/09/23.

[32] F. C. Campbell, "Chapter 6 - Curing: It's a Matter of Time (t), Temperature (T) and Pressure (P)," in *Manufacturing Processes for Advanced Composites*, F. C. Campbell, Ed. Amsterdam: Elsevier Science, 2004, pp. 175-221, doi: 10.1016/B978-185617415-2/50007-1. [Online]. Available: https://www.sciencedirect.com/science/article/pii/B9781856174152500071

[33] N. Zobeiry and A. Poursartip, "3 - The origins of residual stress and its evaluation in composite materials," in *Structural Integrity and Durability of Advanced Composites*, P. W. R. Beaumont, C. Soutis, and A. Hodzic, Eds.: Woodhead Publishing, 2015, pp. 43-72, doi: 10.1016/B978-0-08-100137-0.00003-1.

[34] E. Oromiehie, B. G. Prusty, P. Compston, and G. Rajan, "Automated fibre placement based composite structures: Review on the defects, impacts and inspections techniques," *Composite Structures*, vol. 224, p. 110987, Sep. 2019, doi: 10.1016/j.compstruct.2019.110987.

[35] F. Henne. "Thermoplastic in situ fiber placement for future solid rocket motor casings manufacturing." https://silo.tips/download/thermoplastic-in-situ-fiber-placement# (accessed Sep. 10, 2022).

[36] L. Zhang, X. Wang, J. Pei, and Y. Zhou, "Review of automated fibre placement and its prospects for advanced composites," *Journal of Materials Science*, vol. 55, no. 17, pp. 7121-7155, Jun. 2020, doi: 10.1007/s10853-019-04090-7.

[37] F. Henne *et al.*, *Termoplastic in situ fiber placement for future solid rocket motor casings manufacturing*. 2014.

[38] N. C. Centre. "Demonstrating the future of composite space tank technology." https://www.nccuk.com/news/demonstrating-the-future-of-composite-space-tank-technology/ (accessed Aug. 15, 2022).

[39] J. T. Evans and A. G. Gibson, "Composite Angle Ply Laminates and Netting Analysis," *Proceedings: Mathematical, Physical and Engineering Sciences*, vol. 458, no. 2028, pp. 3079-3088, Dec. 2002, doi: 10.1098/rspa.2002.1066. Accessed: 2022/09/14/.

[40] B. Tew, "Preliminary design of tubular composite structures using netting theory and composite degradation factors," Nov. 1995, doi: 10.1115/1.2842141.

[41] S. Sapre, K. Pareek, and M. Vyas, "Investigation of structural stability of type IV compressed hydrogen storage tank during refueling of fuel cell vehicle," *Energy Storage*, vol. 2, no. 4, p. e150, Mar. 2020, doi: 10.1002/est2.150.

[42] V. V. Vasiliev, *Composite pressure vessels: Analysis, design, and manufacturing*. Bull Ridge Corporation, 2009. [Online]. Available: https://books.google.pt/books?id=oF-oWPmKU4UC&printsec=frontcover&hl=pt-PT&source=gbs_ge_summary_r&cad=0#v=onepage&q&f=false

[43] W. Mahdy, H. Kamel, and E. Soaly, "Design of Optimum Filament Wound Pressure Vessel with Integrated End Domes," *International Conference on Aerospace Sciences and Aviation Technology*, vol. 16, pp. 1-15, May 2015, doi: 10.21608/asat.2015.22929.

[44] A. Vafaeesefat, "Dome shape optimization of composite pressure vessels based on rational B-spline curve and genetic algorithm," *Applied Composite Materials*, vol. 16, no. 5, pp. 321-330, Jul. 2009, doi: 10.1007/s10443-009-9097-3.

[45] M. WM, H. Kamel, and E. El-Soaly, "Design of Optimum Filament Wound Pressure Vessel with Integrated End Domes."

[46] M. Sharma. "Trapezoidal Rule – C Program." https://www.bragitoff.com/2017/08/trapezoidal-rule-c-program/ (accessed Jun. 22, 2022).

[47] M. Legault. "The first commercial Type V composite pressure vessel." https://www.compositesworld.com/articles/next-generation-pressure-vessels (accessed Apr. 29, 2022).

[48] E. S. Agency. "FASTRAC." https://www.eoportal.org/satellite-missions/fastrac (accessed Sep. 16, 2022).

[49] I. Composite Technology Development. "CTD readies another batch of liner-less, lightweight tanks for use in UAVs." https://ctd-materials.com/ctd-delivers-another-batch-of-lightweight-uav-composite-pressure-vessels/ (accessed Apr. 25, 2022).

[50] I. Composite Technology Development. "CTD Supports Lockheed Martin Group 2 UAS World Record Flight." https://ctd-materials.com/ctd-supports-lockheed-martin-group-2-uas-world-record-flight/ (accessed Apr. 25, 2022).

[51] N. Liu *et al.*, "Progress in research on composite cryogenic propellant tank for large aerospace vehicles," *Composites Part A: Applied Science and Manufacturing*, vol. 143, p. 106297, Apr. 2021, doi: 10.1016/j.compositesa.2021.106297.

[52] D. Mosher. "The trickiest part of Elon Musk's Mars spaceship — a giant black orb — just passed a critical test." https://www.businessinsider.com/spacex-carbon-fiber-fuel-tank-ocean-ship-test-2016-11 (accessed Sep. 10, 2022).

[53] V. Kushwaha. "Why Elon Musk Chose Stainless Steel To Build SpaceX's Starship." https://www.educationaltechs.com/2019/02/spacex-stainless-steel-starship.html (accessed Sep. 15, 2022).

[54] G. Nehls. "Boeing all-composite cryogenic fuel tank proves technology readiness." https://www.compositesworld.com/news/the-gill-corp-is-awarded-boeing-contract-extension (accessed Sep. 10, 2022).

[55] E. J. Thompson, "Design of a multi-piece removable mandrel mold tool to fabricate and control inner mold surface contour of a composite wing spar," M.S. thesis, College of Engineering and Mineral Resources at West Virginia University, West Virginia, United States, 2010.

[56] A. Dey, A. Kumar, A. K. Sikder, and M. Gupta, "Chemically Collapsible Mandrel for Solid Rocket Motor Processing," *Journal of Aerospace Technology and Management*, vol. 7, no. 3, pp. 277-284, Sep. 2015, doi: 10.5028/jatm.v7i3.494.

[57] Method fabricating a collapsible mandrel structure to be used in manufacturing reinforced hollow tanks, by J. C. Brooks. (1987, Aug. 04). US4684423A [Online]. Available: https://patents.google.com/patent/US4684423A/en?oq=US4684423A

[58] M. Behl and A. Lendlein, "Shape-memory polymers," *Materials Today*, vol. 10, no. 4, pp. 20-28, Apr. 2007, doi: 10.1016/S1369-7021(07)70047-0.

[59] S. Tooling. "Capabilities." https://smarttooling.com/capabilities/ (accessed Apr. 28, 2022).

[60] S. Tooling. "UAV Inlet Duct Case Study." https://smarttooling.com/wp-content/uploads/2020/11/ST_UAV_InletDuct_CaseStudy_web.pdf (accessed May. 08, 2022).

[61] C. T. Development. "MUPET™ Composite Tooling." https://ctd-materials.com/engineered-materials/mupet/ (accessed Apr. 29, 2022).

[62] Low weight high performance composite vessel and method of making same, by B. Jones. (2004, Jan. 18). US20040026431A1 [Online]. Available: https://patents.google.com/patent/US20040026431A1/en?oq=US20040026431A1

[63] Simplify3D. "PVA." https://www.simplify3d.com/support/materials-guide/pva/ (accessed Apr. 29, 2022).

[64] V. Goodship and D. Jacobs, *Polyvinyl Alcohol: Materials, Processing and Applications*. Smithers Rapra Technology, 2009. [Online]. Available: https://books.google.pt/books?id=rryTPgAACAAJ

[65] G. Pearce, "Design of a Linerless Carbon Fibre Composite Pressure Vessel for Cryogenic Fuel Tank Applications," in *Hydrogen Liquefaction and Storage Symposium*, University of Western Australia, Perth, 2019. [Online]. Available: http://handle.unsw.edu.au/1959.4/unsworks_61641

[66] "Chapter 14 - Sodium silicate bonded sand," in *Foseco Ferrous Foundryman's Handbook (Eleventh Edition)*, J. R. Brown, Ed. Oxford: Butterworth-Heinemann, 2000, pp. 204-215, doi: 10.1016/B978-075064284-2/50015-6.

[67] K. Iqbal, "Development of a liner-less composite CNG cylinder and improved mechanical properties of cylinder materials," M.S. thesis, HKUST, Hong Kong, China, 2008. [Online]. Available: https://hdl.handle.net/1783.1/5175

[68] ExOne, "Catalog of Innovative 3D Printed Tooling Solutions," ed, 2022.

[69] R. Lucas. "3D Printing Delivers New, Easy-to-Use Washout Tooling for Composites." https://www.sme.org/technologies/articles/2019/september/3d-printing-delivers-new-easy-to-use-washout-tooling-for-composites/ (accessed Mar. 21, 2022).

[70] Water soluble tooling materials for composite structures, by J. L. L. Gregory J. Artz, K. Ranji Vaidyanathan, Joseph Walish. (2004, Dec. 07). US6828373B2

[71] A. C. Manufacturing. "Our Products." https://acmtucson.com/products/ (accessed Mar. 16, 2022).

[72] M. Richardson. "Simply wash and go!" https://www.composites.media/simply-wash-and-go (accessed Mar. 16, 2022).

[73] K. Ryan *et al.*, "Prediction of pressure cycle induced microcrack damage in linerless composite tanks," in *47th AIAA/ASME/ASCE/AHS/ASC Structures, Structural Dynamics, and Materials Conference 14th AIAA/ASME/AHS Adaptive Structures Conference 7th*, 2006, p. 2201.

[74] Damage and leakage barrier in all-composite pressure vessels and storage tanks, by J. Cronin, K. Mallick, M. Lake, M. Warner, and N. Munshi. (2011, Dec. 13). US8074826B2 [Online]. Available: https://patents.google.com/patent/US8074826B2/en?oq=US8074826B2

[75] Method for producing a leak-tight vessel, and a leak-tight vessel, by T. Vanswijgenhoven, D. Vanswijgenhoven, and A. Seifert. (2022, Apr. 12). US11299312B2 [Online]. Available: https://patents.google.com/patent/US11299312B2/en?oq=US11299312B2

[76] B. W. Grimsley, R. J. Cano, N. J. Johnston, A. C. Loos, and W. M. McMahon, "Hybrid composites for LH2 fuel tank structure," Jan. 2002. [Online]. Available: https://citeseerx.ist.psu.edu/viewdoc/download?doi=10.1.1.6.5445&rep=rep1&type=pdf

[77] C. Maes, W. Luyten, G. Herremans, R. Peeters, R. Carleer, and M. Buntinx, "Recent Updates on the Barrier Properties of Ethylene Vinyl Alcohol Copolymer (EVOH): A Review," *Polymer Reviews*, vol. 58, no. 2, pp. 209-246, Apr. 2018, doi: 10.1080/15583724.2017.1394323.

[78] H. M. Kim and H. S. Lee, "Water and oxygen permeation through transparent ethylene vinyl alcohol/(graphene oxide) membranes," *Carbon letters*, vol. 15, no. 1, pp. 50-56, Jan. 2014, doi: 10.5714/CL.2014.15.1.050.

[79] Y. Cui, S. I. Kundalwal, and S. Kumar, "Gas barrier performance of graphene/polymer nanocomposites," *Carbon*, vol. 98, pp. 313-333, Mar. 2016, doi: 10.1016/j.carbon.2015.11.018.

[80] W. Jiao *et al.*, "Improving the gas barrier properties of Fe3O4/graphite nanoplatelet reinforced nanocomposites by a low magnetic field induced alignment," *Composites Science and Technology*, vol. 99, pp. 124-130, Jul. 2014, doi: 10.1016/j.compscitech.2014.05.022.

[81] C. Habel *et al.*, "Lightweight ultra-high-barrier liners for helium and hydrogen," *ACS nano*, vol. 14, no. 6, pp. 7018-7024, May 2020, doi: 10.1021/acsnano.0c01633.

[82] F. Hübner, A. Brückner, T. Dickhut, V. Altstädt, A. R. de Anda, and H. Ruckdäschel, "Low temperature fatigue crack propagation in toughened epoxy resins aimed for filament winding of type V composite pressure vessels," *Polymer Testing*, vol. 102, p. 107323, Oct. 2021, doi: 10.1016/j.polymertesting.2021.107323.

[83] D. Murima, "Novel barrier coatings based on nanoclay-polymer composites," M.S. thesis, Faculty of Science at Stellenbosch University, Stellenbosch , South Africa, 2015. [Online]. Available: http://hdl.handle.net/10019.1/96994

[84] K. Yonemoto, Y. Yamamoto, K. Okuyama, and T. Ebina, "Application of CFRP with high hydrogen gas barrier characteristics to fuel tanks of space transportation system," vol. 7, no. ists26, pp. Pc_13-Pc_18, Apr. 2009, doi: 10.2322/tstj.7.Pc_13.

[85] O. C. Compton, S. Kim, C. Pierre, J. M. Torkelson, and S. T. Nguyen, "Crumpled graphene nanosheets as highly effective barrier property enhancers," *Advanced materials*, vol. 22, no. 42, pp. 4759-4763, Sep. 2010, doi: 10.1002/adma.201000960.

[86] A. G. Materials. "What is Graphene?" https://www.appliedgraphenematerials.com/who-are-agm/what-is-graphene/ (accessed Jun. 20, 2022).

[87] M. J. Allen, V. C. Tung, and R. B. Kaner, "Honeycomb carbon: a review of graphene," *Chemical reviews*, vol. 110, no. 1, pp. 132-145, Jul. 2009, doi: 10.1021/cr900070d.

[88] C. Lee, X. Wei, J. W. Kysar, and J. Hone, "Measurement of the elastic properties and intrinsic strength of monolayer graphene," *science*, vol. 321, no. 5887, pp. 385-388, Jul. 2008, doi: 10.1126/science.1157996.

[89] A. R. b. M. Yusoff, L. Dai, H.-M. Cheng, and J. Liu, "Graphene based energy devices," *Nanoscale*, vol. 7, no. 16, pp. 6881-6882, Mar. 2015, doi: 10.1039/C5NR90062J.

[90] L. Diamante, "Graphene 101: All about graphene and its many forms," ed. Graphene Flagship, 2021.

[91] S. A. Graphenest. "Patented Technology Process." https://graphenest.com/about/ (accessed Aug. 24, 2022).

[92] S. A. Graphenest. "Graphene Nanoplatelets Size Distribution." https://graphenest.com/graphene/ (accessed Jun. 15, 2022).

[93] A. G. Materials. "The New Anti-Corrosion Toolbox." https://www.appliedgraphenematerials.com/wp-content/uploads/2021/07/AGM_Coatings_Corrosion_2021-compressed.pdf (accessed Aug. 26, 2022).

[94] S. Francis. "Graphene technology enables composite cryogenic pressure vessels." https://www.compositesworld.com/news/graphene-technology-enables-composite-cyogenic-pressure-vessels (accessed Sep. 10, 2022).

[95] C.-C. T. Systems. "Composite pressure vessel CTS with anti-break valve, 6.8l." https://www.gamat-shop.com/composite-pressure-vessel-cts-with-anti-break-valve-6-8l (accessed Aug. 15, 2022).

[96] O. Corporation, Olin LITESTONE™ Filament Winding System - LITESTONE 2130E Epoxy Resin and LITESTONE 2142H Hardener

[97] J. B. Donnet and R. C. Bansal, *Carbon Fibers*. Crc Press, 1998. [Online]. Available: https://books.google.pt/books?id=YkN8xIwL0dsC&pg=PA231&dq=Carbon+fibers+donnet&hl=pt-PT&sa=X&ved=2ahUKEwiTka3Zp7D6AhUSgf0HHTZACJMQ6AF6BAgLEAI#v=onepage&q=Carbon%20fibers%20donnet&f=false

[98] D. Mounier, C. Poilâne, C. Bûcher, and P. Picart, "Evaluation of transverse elastic properties of fibers used in composite materials by laser resonant ultrasound spectroscopy," in *Acoustics 2012*, 2012.

[99] T. LIMITED, Tenax™-E HTS45 E23 12K 800tex, Out. 2021.

[100] M. Madhavi, K. Rao, and K. N. Rao, "Design and Analysis of Filament Wound Composite Pressure Vessel with Integrated-end Domes," *Defence science journal*, vol. 59, no. 1, Jan. 2009, doi: 10.14429/dsj.59.1488.

[101] A. A. S. M. Inc. "AISI Type 304 Stainless Steel." https://asm.matweb.com/search/SpecificMaterial.asp?bassnum=mq304a (accessed Jul. 15, 2022).

[102] I. Composites. "IC Products & Services." https://www.infinitecomposites.com/infinite-composite-pressure-vessels (accessed Apr. 25, 2022).

[103] S. M. S. v. T. L. Şti. "SPVR Series Dissolver Machine Discs." https://sozer.com/en/auxiliary-equipments/Products/spvr-series-dissolver-machine-discs (accessed Sep. 05, 2022).

[104] L. Carolo. "3D Printer Material Cost: An Overview." https://all3dp.com/2/3d-printer-material-cost-the-real-cost-of-3d-printing-materials/ (accessed Apr. 29, 2022).

[105] A. C. AG, "Mandrel Production Presentation 20101109," ed, 2010.

[106] C. S.p.A. "Cylinder Moulds." https://www.controls-group.com/eng/concrete-specimen-molds/cylinder-moulds.php (accessed May 25, 2022).

[107] MIKROSAM. "MAW 20 FB5/1." https://archive.mikrosam.com/new/article/en/maw-20-fb51/index.html (accessed Jul. 23, 2022).

[108] I. Composites. "Tank Specifications." https://www.infinitecomposites.com/downloads (accessed Sep. 10, 2022).

[109] R. Shufen and U. S. Dixit, "A Review of Theoretical and Experimental Research on Various Autofrettage Processes," *Journal of Pressure Vessel Technology*, vol. 140, no. 5, Aug. 2018, doi: 10.1115/1.4039206. Accessed: 9/22/2022.

[110] M. Vaz, E. R. Hulse, and M. Tomiyama, "A note on parameter identification of the AISI 304 stainless steel using micromechanical-based phenomenological approaches," *Materials Research*, vol. 22, Apr. 2019, doi: 10.1590/1980-5373-MR-2019-0222.

[111] L. MatWeb. "Aluminum 7075-T6; 7075-T651." https://www.matweb.com/search/DataSheet.aspx?MatGUID=4f19a42be94546b686bbf43f79c51b7d&ckck=1 (accessed Sep. 10, 2022).

[112] X. Li, K. Pandya, N. Karathanasopoulos, C. C. Roth, and D. Mohr, "Plasticity and fracture of aluminium 7075 at high strain rates and elevated temperatures," *EPJ Web Conf.*, vol. 250, p. 05007, Sep. 2021, doi: 10.1051/epjconf/202125005007.

[113] *Gas cylinders — Refillable composite gas cylinders and tubes*, ISO 11119-3:2013(E), I. O. f. Standardization, 2013. [Online]. Available: https://www.iso.org/standard/50523.html